

Fracture Angles in Numerical Simulations of Sea Ice with Viscous-Plastic Rheologies

A thesis presented for the degree of

**doctor rerum naturalium
(Dr. rer. nat.)**

by

Damien Ringeisen

Thesis Reviewers:

Prof. Dr. Thomas Jung

Prof. Dr. Christian Haas



Submission: June 15, 2020
Doctoral Colloquium: September 4, 2020

Department 1
Physics and Electrical Engineering
University of Bremen
Germany

*To my aunt, France Faure-Perrel,
Who always showed a lot
Of interest in my work,
And left us too early.*

We are part of nature, a product of a long evolutionary journey. To some degree, we carry the ancient oceans in our blood. . . . Our brains and nervous systems did not suddenly spring into existence without long antecedents in natural history. That which we most prize as integral to our humanity - our extraordinary capacity to think on complex conceptual levels - can be traced back to the nerve network of primitive invertebrates, the ganglia of a mollusk, the spinal cord of a fish, the brain of an amphibian, and the cerebral cortex of a primate.

Defending the Earth: A Dialogue Between
Murray Bookchin and Dave Foreman
MURRAY BOOKCHIN

Évoquer l'écologie, c'est comme parler du suffrage universel et du repos du dimanche : dans un premier temps, tous les bourgeois et tous les partisans de l'ordre vous disent que vous voulez leur ruine, le triomphe de l'anarchie et de l'obscurantisme. Puis, dans un deuxième temps, quand la force des choses et la pression populaire deviennent irrésistibles, on vous accorde ce qu'on vous refusait hier et, fondamentalement, rien ne change.

Leur écologie et la nôtre
ANDRÉ GORZ

Abstract

Sea ice is an essential component of the climate system because it modulates the exchange of energy between the ocean and the atmosphere. Under stress from wind and ocean currents, sea ice deforms constantly. Sea ice deformation takes the shape of narrow lines, the Linear Kinematic Features (LKFs). LKFs influence the heat transfer, mass balance, and sea ice dynamics, so LKFs should be accurately represented in high-resolution climate models. Sea ice is commonly modeled using viscous-plastic (VP) rheologies defined by a yield curve and a flow rule. Recent work showed that VP sea ice models explicitly create LKFs but overestimate their intersection angles.

This thesis aims to investigate the link between the angles of fracture in sea ice models and the parametrization of the sea ice internal stresses using idealized compression experiments. Three questions are addressed: Which parameters of the VP rheologies influence the fracture angle? Which theoretical framework explains this influence? Which rheologies should be used to simulate intersection angles at the observed range?

With the commonly used standard VP rheology with an elliptical yield curve and a normal flow rule, the fracture angles are linked to the yield curve's elliptical shape. Because of this shape, this rheology cannot create sea ice fracture angles more acute than 30° in uniaxial compression, even by changing the aspect of the ellipse. The classical coulombic theory predicts the angle of fracture accurately when adapted to the context of sea ice modeling.

A new rheology with an elliptical yield curve and a non-normal flow rule shows that fracture angles are also sensitive to the orientation of the flow rule. Using this new rheology allows creating fracture angles as low as 22° in uniaxial compression. A theory based on the angle of dilatancy and observations of granular materials predicts precisely the simulated angles.

Alternative rheologies can create fracture angles lower than 30° . With Mohr–Coulomb yield curves, fracture angles are well predicted by joining the concepts of coulombic friction and angle of dilatancy. Teardrop and Parabolic lens yield curves create small angles of fracture in uni-axial compression when used with small tensile strength.

Using a more realistic sea ice cover with heterogeneity, failure under deformation takes the form of a network of fracture lines. The choice of rheology strongly influences the angle of fracture in this network. Two rheologies are suitable candidates to decrease the fracture angles in sea ice VP models.

In conclusion, fracture angles in sea ice models are determined by the properties of the VP rheology and can be accurately predicted using fracture orientation theory. Changing the rheology can reduce the fracture angles in sea ice simulations. With the results presented in this thesis, new rheologies could be inferred from observations to represent sea ice fracture more realistically.

Résumé

La glace de mer (ou banquise) est une composante essentielle du système climatique car elle module l'échange d'énergie entre l'océan et l'atmosphère. Sous l'effet du vent et des courants océaniques, la glace de mer se déforme constamment. La déformation de la glace de mer prend la forme de lignes étroites, les *Linear Kinematic Features* (LKFs). Les LKFs influencent le transfert de chaleur, le bilan de masse et la dynamique de la glace de mer, elles doivent donc être représentées avec précision dans les modèles climatiques à haute résolution. La glace de mer est généralement modélisée à l'aide de rhéologies visco-plastiques (VP) définies par un critère de cassure et une règle d'écoulement. Des travaux récents ont montré que les modèles VP créent explicitement des LKFs mais surestiment leurs angles d'intersection.

Cette thèse vise à étudier le lien entre les angles de fracture dans les modèles VP de glace de mer et la paramétrisation des contraintes internes de la glace de mer en utilisant des expériences de compression idéales. Trois questions sont abordées : Quels sont les paramètres des rhéologies VP qui influencent l'angle de fracture ? Quel cadre théorique explique ces influences ? Quelles rhéologies doivent être utilisées pour simuler les angles d'intersection dans la gamme observée ?

Avec la rhéologie VP avec un critère de cassure elliptique et une règle d'écoulement normale, les angles de fracture sont liés à la forme elliptique du critère de cassure. En raison de cette forme, cette rhéologie ne peut pas créer des angles de fracture de la glace de mer plus aigus que 30° en compression uniaxiale, même en modifiant l'aspect de l'ellipse. La théorie coulombienne classique permet de prédire avec précision l'angle de fracture.

Une nouvelle rhéologie VP avec un critère de cassure elliptique et une règle d'écoulement non-normale montre que les angles de fracture sont également sensibles à l'orientation de la règle d'écoulement. L'utilisation de cette nouvelle rhéologie permet de créer des angles de fracture aussi petit que 22° en compression uni-axiale. Une théorie basée sur l'angle de dilatation et l'observation des matériaux granulaires permet de prédire avec précision les angles simulés.

D'autres rhéologies VP permettent de créer des angles de fracture inférieurs à 30° . Avec les critères de cassure Mohr–Coulomb, les angles de rupture sont bien prédits en associant les concepts de frottement coulombique et d'angle de dilatation. Les critères de cassure *Teardrop* et *Parabolic Lens* créent des angles de fracture aigus en compression uni-axiale lorsqu'elles sont utilisées avec une faible résistance à la traction.

En utilisant une couverture de glace de mer plus réaliste et hétérogène, la rupture sous déformation prend la forme d'un réseau de lignes de fracture. La rhéologie influence fortement l'angle de fracture dans ce réseau. Deux rhéologies présentés dans cette thèse sont des candidates appropriés pour diminuer les angles de fracture dans les modèles VP de glace de mer.

En conclusion, les angles de fracture dans les modèles de la glace de mer sont déterminés par les propriétés de la rhéologie VP et peuvent être prédits avec précision en utilisant les théorie de l'orientation de la fracture. La modification de la rhéologie peut réduire les angles de fracture dans les simulations de glace de mer. Avec les résultats présentés dans cette thèse, de nouvelles rhéologies pourraient être déduites des observations pour représenter la fracture de la glace de mer d'une manière plus réaliste.

Contents

Abstract	3
Résumé	5
Contents	7
1 Introduction	11
1.1 Climate change and the Arctic	11
1.1.1 A global climate change	11
1.1.2 Climate change in the Arctic	12
1.2 Modeling Sea Ice	13
1.2.1 Observations of sea ice properties	13
1.2.2 Sea ice models	16
1.3 Research Questions	17
2 Sea ice viscous-plastic rheologies	19
2.1 Sea ice dynamics	19
2.1.1 Sea ice momentum equation and rheology	19
2.1.2 Viscous-Plastic framework	20
2.1.3 Stress tensors definition	21
2.1.4 Strain rates definition	22
2.1.5 Defining the VP constitutive equations	23
2.2 VP Rheologies: Yield curves and flow rules	26
2.2.1 Elliptical yield curve with normal flow rule	26
2.2.2 Elliptical yield curve with non-normal flow rule	30
2.2.3 Mohr–Coulomb yield curve with shear flow rule	31
2.2.4 Mohr–Coulomb yield curve with elliptical plastic potential	33
2.2.5 Truncated ellipse - Coulombic yield curve	34
2.2.6 Teardrop yield curve with normal flow rule	35
2.2.7 Parabolic Lens yield curve with normal flow rule	38
2.2.8 Other VP rheologies	39
2.3 Summary	39
3 Theory of fracture angles	41
3.1 The orientation of shear bands in granular materials	41
3.2 Mohr–Coulomb theory of the internal angle of friction	43
3.3 Linking fracture angle and sea ice VP rheology	44
3.3.1 Linking fracture angle to the yield curve	44
3.3.2 Linking the fracture angle to the flow rule	46

3.4	Fracture angles for uniaxial compression	47
3.4.1	Uniaxial compression	47
3.4.2	Elliptical yield curve with a normal flow rule	48
3.4.3	Elliptical yield curve with non-normal flow rule	50
3.4.4	Mohr-Coulomb yield curve with shear only	51
3.4.5	Mohr-Coulomb yield curve with elliptical plastic potential	52
3.4.6	Coulombic yield curve (or Truncate ellipse)	52
3.4.7	Teardrop yield curve with normal flow rule	54
3.4.8	Parabolic lens yield curve with normal flow rule	56
3.5	Summary	56
4	Simulating intersection angles between conjugate faults in sea ice with different VP rheologies	57
4.1	Introduction	58
4.2	Experimental setup	61
4.2.1	Viscous-plastic model	61
4.2.2	Yield curve	62
4.2.3	Idealized experiment	64
4.3	Results	66
4.3.1	Uni-axial compressive test – default parameters	66
4.3.2	Sensitivity experiments	66
4.3.3	Effects of the yield curve on the fracture angle	72
4.4	Discussion	75
4.5	Conclusions	77
5	Non-normal flow rules affect fracture angles in sea ice viscous-plastic rheologies	81
5.1	Introduction	82
5.2	Sea ice Model and rheology	85
5.2.1	Building the sea ice VP constitutive equations	85
5.2.2	Elliptical yield curve with non-normal flow rule	87
5.2.3	Linking fracture and flow rule	87
5.3	Experimental setup and numerical scheme	91
5.4	Results	92
5.5	Discussion	94
5.6	Conclusions	98
6	Fracture angles with alternative VP rheologies	99
6.1	Experimental setup	99
6.2	Alternative rheologies	99
6.2.1	Mohr-Coulomb yield curve with shear flow rule	99
6.2.2	Mohr-Coulomb yield curve with elliptical plastic potential (MCE rheology)	104
6.2.3	Teardrop and Parabolic Lens rheologies	105
6.3	Discussion	107
6.3.1	Mohr-Coulomb yield curves	107
6.3.2	Teardrop and Parabolic yield curve	109
6.4	Summary	109

7	Fracture angles with heterogeneous sea ice cover	111
7.1	Initial heterogeneous ice cover	112
7.2	Results	112
7.2.1	Elliptical yield curve with normal flow rule (ENFR)	112
7.2.2	Elliptical yield curve with non-normal flow rule (ENNFR)	113
7.2.3	Mohr–Coulomb yield curve with an elliptical plastic potential (MCE)	115
7.2.4	Teardrop and Parabolic Lens rheologies	116
7.2.5	Fracture Angles	117
7.3	Discussion	117
7.4	Summary	119
8	Conclusions and outlook	121
8.1	Conclusions	121
8.2	Outlook	122
	List of Figures	127
	List of Tables	128
	List of Abbreviation	129
	Bibliography	131

Chapter 1

Introduction

Dans la bataille de l'homme et du monde, ce n'est pas le monde qui commence.

— Gaston BACHELARD

1.1 Climate change and the Arctic

1.1.1 A global climate change

The reality of an anthropogenic climate change is not a novelty; scientific literature mentions the influence of greenhouse gases (GHG, mainly CO_2 and CH_4) on the earth climate since the 1960s-1970s. In 1967, Manabe and Wetherald showed that an increase of CO_2 in the atmosphere would increase the global surface temperature. Shortly after, Keeling et al. state in 1976 that *“The air at Mauna Loa Observatory may be slightly influenced by local processes which cannot be expunged from the record, but the observed long term trend of rising CO_2 , appears clearly to be in response to increasing amounts of industrial CO_2 , in the air on a global scale.”*. These two papers are seminal studies in climate science and mark the beginning of our understanding of the current climate change. The CO_2 time series from Mauna Loa Observatory is still updated today and reached 417 ppm in June 2020, against an annual average of 327 ppm in 1971. Since these studies, climate science grew as a scientific field, and climate simulations have improved to give accurate predictions (Hausfather et al., 2020). As explained in the *Summary for Policymakers* from the latest Assessment Report (AR5) from the International Panel on Climate Change (IPCC, 2013): *“Continued emissions of greenhouse gases will cause further warming and changes in all components of the climate system. Limiting climate change will require substantial and sustained reductions of greenhouse gas emissions.”*. The report also states that *“Cumulative emissions of CO_2 largely determine global mean surface warming by the late 21st century and beyond [...]. Most aspects of climate change will persist for many centuries even if emissions of CO_2 are stopped. This represents a substantial multi-century climate change commitment created by past, present and future emissions of CO_2 .”*, that is, the effects of past and current GHG emissions will persist in the future, and their consequences need to be predicted and acknowledged.

The earth climate system is complex. It is the sum of its components (soil, ocean, atmosphere, cryosphere, and biosphere) and the sum of the exchanges between them (Donner and Large, 2008). To make valuable and precise predictions, the interactions between the climate components need to be understood. Climate modeling is touching every subject, from biology to glaciology. As an example of

interaction, massive deforestation in the Amazonian forest was shown to influence the climate pathways (Shukla et al., 1990). Over the years, the scientific community added more components, and the number of climate models grew. The Coupled Model Inter-comparison Project (CMIP) aims at comparing them using standardized input and output. The multi-model approach allows us to take account of all novelty and make average predictions. Besides, to improve the different components of the earth system models, projects like the Sea Ice Models Inter-comparison Project (SIMIP, Kreyscher et al., 1997; Notz et al., 2016) have been designed to compare components of different climate models, here the sea ice models.

If local destructive human activities (e.g., toxic waste pollution or deforestation) create local extinction events, the rapid climate change observed and predicted will have dramatic effects on the whole of earth's biosphere. The ecosystems transform faster than ever before and already show the extinction of many species at a global scale (Trisos et al., 2020; Urban, 2015). This global modification of the climate earth system is being addressed now in large conferences like the *2015 United Nations Climate Change Conference* (COP21). This conference led to the *Paris Agreement*. This agreement states that global warming should be limited to 1.5°C above pre-industrial levels. The United Nations then asked the IPCC to release a scientific report on the impact of a 1.5°C warming and the pathways to reach this objective (IPCC, 2018). This report explores the expected impacts on several ecosystems and shows that the Arctic regions are the most impacted biome after warm coral reefs.

1.1.2 Climate change in the Arctic

The polar regions, Arctic and Antarctic, are the areas of the world most sensitive to climate change. If the *Paris Agreement* is stating a limit of 1.5°C, this average temperature is a global average, but the temperature increase is predicted to be much higher in the Arctic. The Arctic have already the highest warming on the planet, as shown on Figure 1.1; it warms twice as fast as the Northern Hemisphere (Serreze et al., 2009). This phenomenon is called *Arctic Amplification* (Manabe and Stouffer, 1980). This drastic change in temperature has strong effects on the Arctic environment. Arctic Amplification was shown to be linked to the albedo feedback (Screen and Simmonds, 2010), but also to temperature feedback (Pithan and Mauritsen, 2014) and may be linked to extreme weather in mid-latitudes (Francis and Vavrus, 2012).

The reduction of area and volume of Arctic sea ice is one of the most visible and most dramatic effects of the ongoing climate change. Figure 1.2 shows the reduction of September sea ice extent and volume between the year 1979 and the year 2018. Besides the reduction of the sea ice-covered area, the older and thicker sea ice is disappearing: the sea ice volume decreased by 2/3. Recent studies showed that the Arctic ocean could be free of ice at the end of summer by the year 2050. In this case, all the old sea ice would have melted, and the sea ice cover would be only composed of young ice (SIMIP Community, 2020; Notz and Stroeve, 2018).

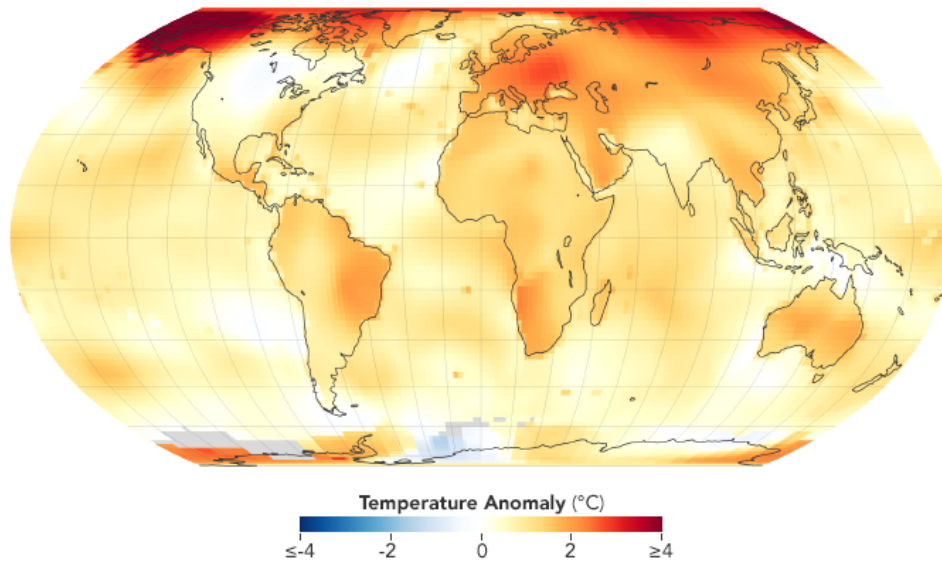


Figure 1.1: Global temperature anomalies in 2019 compared to the period 1951-1980. The Arctic is warming faster than any other region of the planet. Picture from NASA/Joshua Steven, public domain.

1.2 Modeling Sea Ice

1.2.1 Observations of sea ice properties

What is sea ice? This question is central to modelling sea ice. An appropriate set of assumptions is necessary to determine which parametrizations are suitable for sea ice modeling. General properties of sea ice can be inferred from observations, as illustrated by an example aerial photograph (Figure 1.3):

Sea ice is an interface medium Sea ice is frozen seawater which floats on the ocean surface until it has melted away, in the Arctic or in the subarctic regions. Sea ice is a film over the ocean that alters the interface between ocean and atmosphere (Vihma, 2014). It insulates the relatively warm ocean from the cold polar atmosphere and blocks shortwave radiations from penetrating the ocean (Curry et al., 1995). The salt rejection as water freezes, the brine rejection, or the release of freshwater as the ice melts, influence thermohaline circulation (Itkin et al., 2015; Nguyen et al., 2012).

Sea ice is a granular medium Sea ice is composed of discrete pieces of solid ice, called ice floes. Floes have different sizes; they grind, raft, pile, break or freeze together (Rothrock and Thorndike, 1984). Sea ice is a granular medium that shows continuity at large scale (Overland et al., 1998). Narrow lines of deformations called Linear Kinematic Features (LKFs) are common in Arctic sea ice. These very localized deformation zones are characteristic of granular materials like sands (Hutter and Rajagopal, 1994) and have been investigated for over two centuries (Coulomb, 1773). In sea ice, LKFs occur at all scales larger than the floe size, and their distribution follows a well-known power scaling law (Weiss and Dansereau, 2017; Bouchat and Tremblay, 2017; Hutter et al., 2019).

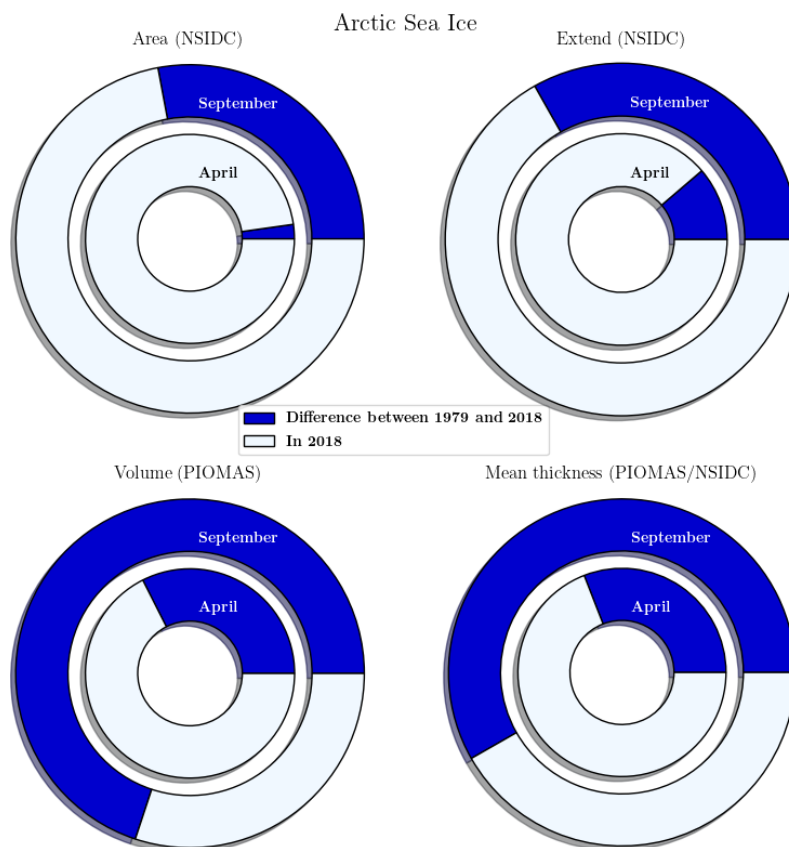


Figure 1.2: Comparison of the area, extend, volume, and mean thickness of the Arctic sea ice between 1979 and 2018. A complete pie chart represents the amount of ice 1979; the ice remaining in 2018 is shown in white, blue color shows the melted ice. The outside pie chart is for the September minimum, while the inside pie chart corresponds to the April maximum. Datasets from PIOMAS (Zhang and Rothrock, 2003; Schweiger et al., 2011, data available at <http://psc.apl.uw.edu/research/projects/arctic-sea-ice-volume-anomaly/>) and the NSIDC sea ice index (Fetterer, F. et al., 2017, data available at https://nsidc.org/data/seaice_index/).

Sea ice is a brittle material The ice is a granular material; however, the properties of its grains, the ice floes, change quickly. In contrast with other granular materials (e.g., sand or clay) where the grains are slowly eroded, the changes in granular structure of sea ice are fast (Dempsey et al., 2012). Wind breaks sea ice on scales from tens to hundreds of kilometers as stress propagates (Hunkins, 1960), leads freeze rapidly during the cold winter months (Petrich et al., 2007), and waves break the ice in the Marginal Ice Zone (Herman, 2017). Sea ice fracture can lead to a weakening (lead opening) or strengthening (refrozen ridges) of the sea ice cover; in addition, floes size can grow again when the floes aggregate and freeze together (Horvat and Tziperman, 2015; Horvat and Tziperman, 2017).

Sea ice dynamics occur on a 2D plane, but penetrate the 3rd dimension In contrast to other granular materials, sea ice is bounded to the 2D ocean-atmosphere interface by gravity and buoyancy, although ice can escape above and below the ocean surface. Usual stress investigation of material make use

of a circular symmetry, or use plane stress but strictly limited to a 2D plane (e.g., Roscoe et al., 1958). In the case of sea ice, ice floes can raft or break and pile, creating ice ridges (Hopkins, 1994). This property of sea ice to dissipate energy by *escaping in the 3rd dimension* is unique. The quick changes in the ice structure influence the ice properties directly, like thickness or internal structure.

All the processes described above happen on a small scale compared to the sea ice extent. The vastness of the Arctic ocean and the harsh polar meteorological conditions make the in-situ observation of sea ice properties difficult. Most of the recent observation of sea ice are made with remote sensing methods like satellite instruments (see a review in Kwok (2010)), shipborne (Lund et al., 2018) or ground-based sea ice radars (Oikkonen et al., 2016), or airborne electromagnetic sensor (Haas et al., 2009).



Figure 1.3: Aerial picture of a sea ice lead at a small scale. The ocean appears as black, while the ice is almost white. The ice floes appear in the lead or in between fractures, with different sizes and various thicknesses. The fracture was recently created; corresponding shapes of ice floes can be observed on each side of the lead. Picture from Lukas Piotrowski (<https://lukaspiotrowski.de/>), personal communication.

The performance of climate simulations in the Arctic is usually measured through large-scale sea ice indicators like sea ice extent, sea ice volume, or exported sea ice volume (SIMIP Community, 2020). Open waters and thin ice in LKFs are responsible for a large part of the heat exchanged between the atmosphere and the ocean despite their small total area (Maykut, 1978; Untersteiner, 1961). It is necessary for climates models to reproduce the observed density and patterns of LKFs to make accurate predictions. The angle of fracture controls the deformation

field that influences the changes in ice thickness via ridging and thermodynamical growth. The ice strength depends on ice thickness; therefore, thickness changes affect the local sea ice anisotropy. Local anisotropy will influence the transmission of stress; thus, the future fracture angles and deformations. For this work, I define the angle of fracture θ as half the intersection angle between two LKFs. The sea ice fracture angle is a suitable indicator to assess the performance of LKFs creation with different models. Observations report fracture angles of 14° (Marko and Thomson, 1977), $15 \pm 1.5^\circ$ (Erlingsson, 1988), 17° to 18° (Cunningham et al., 1994), 24° (Weiss and Schulson, 2009), and 20° to 30° (Hutter and Losch, 2020).

1.2.2 Sea ice models

The first sea ice models used low spatial resolution, by modern standards, with grid spacing of the order of 100 km. At such a coarse resolution, Coon et al. (1974) made three major assumptions: (1) Sea ice has no resistance in tension, (2) the multiple orientations of preexisting leads in a grid cell allow to consider sea ice as an isotropic material, so that (3) sea ice can be modeled with an isotropic yield curve. A system of equations, called a *rheology* (Bingham, 1933; Harrison, 1940), governs the sea ice internal stresses. Sea ice rheologies were designed in the 1970s, each using different material properties: a Elastic-Plastic (EP) model (Coon et al., 1974), an incompressible model (Rothrock, 1975c), and a Viscous-Plastic model (Hibler, 1977; Hibler, 1979). The latter, Hibler’s VP model, became *de facto* the standard sea ice model. Among the 33 CMIP5 (Climate Model Intercomparison Project 5) models compared in Stroeve et al. (2014), 30 use this rheology or variations thereof.

Several aspects of the standard sea ice rheology have been improved over the last 30 years. Here are some commonly used examples: a sub-grid scale Ice Thickness Distribution (ITD) was added to improve the representation of thickness within grid cells (Thorndike et al., 1975; Lipscomb et al., 2007; Ungermann et al., 2017); sea ice models feature more accurate solvers (Lemieux and Tremblay, 2009; Lemieux et al., 2008; Losch and Danilov, 2012; Losch et al., 2014; Hunke, 2001a); grounding schemes and tensile strength help to represent landfast ice (Lemieux et al., 2016; König Beatty and Holland, 2010). Despite these incremental improvements, the dynamical core of the VP model stayed the same. The compatibility of this model (and the associated classical assumptions) with modern high-resolution simulations with grid resolution of order $O(1 \text{ km})$ is questioned (Coon et al., 2007), especially for the representation of sharp edges in the sea ice cover, like fracture lines (Blockley et al., 2020).

The standard VP model is capable of producing LKFs (Hutchings et al., 2005), but generally overestimates the fracture angles (Hutter and Losch, 2020). To improve the representation of fractures, new sea ice rheologies were created. These new rheologies are divided in two categories: [1] rheologies with a different material property than VP, and [2] rheologies that change the strength and the post-fracture deformation properties of sea ice, called respectively yield curve flow rule, within the VP model:

1. Brittle rheologies represent sea ice fracture using a damage parameter in an Elastic model (Elasto-Brittle (Girard et al., 2011), and the Maxwell-Elasto-Brittle (Dansereau et al., 2016)), and show sharp fractures in pan-arctic simulations when implemented in a quasi-lagrangian model (Bouillon and Rampal,

2015). The Elastic-Anisotropic-Plastic (EAP) rheology include a parametrization to represent the observed anisotropic orientation of leads (Wilchinsky and Feltham, 2006a). A decohesive rheology was shown to be skillful to model sea ice leads (Schreyer et al., 2006), also combined with a material-point method (Sulsky et al., 2007). Discrete element models (DEM) represent sea ice as discrete pieces (floes) that include sharp ice-edges (Hopkins, 2002; Herman, 2016).

2. Modifying the parametrization of ice strength and post-fracture deformation changes the representation of LKFs in the standard VP sea ice rheology. Changing the ice strength allowed to reproduce observed ice bridges (Dumont et al., 2009), or reproduce sea ice LKF scaling laws at medium resolution (Bouchat and Tremblay, 2017). Lead permitting simulations with the standard sea ice model reproduce LKFs scaling laws (Hutter et al., 2018), despite previous contradictory studies (Girard et al., 2009). VP rheologies inspired by experiments on granular materials using different strength and post-fracture behavior were proposed (Ip et al., 1991; Tremblay and Mysak, 1997).

Despite new models, no rheology has been shown to reproduce the observed distribution of fracture angles.

Idealized experiments have proven useful in studying the creation of LKFs in sea ice models. For example, the EAP rheology creates sharper fracture than the VP model in idealized experiments (Heorton et al., 2018); the fracture angles with the MEB rheology are well predicted in uni-axial compression (Dansereau et al., 2019); DEMs show the creation of anisotropic floes and fracture patterns in idealized geometries (Wilchinsky et al., 2010). In VP models, rheologies have an effect on the orientation of LKFs (Hutchings et al., 2005); however, to the best of my knowledge, the relationship between the fracture angles and rheology have not yet been shown and explained using high-resolution models. This is the principal motivation for this work.

1.3 Research Questions

In this work, I investigate the link between fracture angles and sea ice VP rheologies using idealized experiments. In experiments designed to highlight the rheology's sole effect, I test various parameterizations for ice strength and post-fracture deformations and compare the modeled fracture angles to theoretical predictions. With the gained knowledge, I aim at finding suitable rheologies to reproduce the acute angles observed between LKFs in the Arctic sea ice.

The research questions guiding my work in this thesis are:

- RQ1** How do sea ice VP rheologies affect the angle of fracture? And what are the independent contributions of the parameterizations for ice strength (yield curve) and the post-fracture behavior (flow rule)?
- RQ2** Which theoretical framework can predict the angle of fracture in sea ice VP rheologies?
- RQ3** Which VP rheologies should be used to create smaller fracture angles and reproduce observed sea ice dynamics?

The thesis is structured as follows:

In Chapter 2, I present the different rheologies used in this thesis, their formulations and characteristic features: sea ice strength in compression, shear, and tension as well as post-fracture behavior (convergence, shearing, and divergence). In addition to existing rheology, I describe two new original VP rheologies.

In Chapter 3, I review theories that link rheologies to fracture angles and adapt them to the context of sea ice modeling to compare to the results of uni-axial compression experiments.

In Chapter 4, I explore various experimental designs to create an idealized experiment that isolates the effect of the rheology on the angle of fracture and explore the fracture angles created by the standard rheology. This chapter has been published in the journal *The Cryosphere* by Ringeisen et al. (2019) under the title “*Simulating intersection angles between conjugate faults in sea ice with different VP rheologies*”.

In Chapter 5, I study the dependence of the fracture angles on the post-fracture behavior using a new VP rheology. This chapter has been submitted to the journal *The Cryosphere* under the title “*Non-normal flow rules affect fracture angles in sea ice viscous-plastic rheologies*”.

In Chapter 6, I present the results of idealized experiments with the remaining sea ice VP rheologies. I then compare compare the resulting fracture angles with the various theories linking rheologies and the orientation of fracture lines.

In Chapter 7, I investigate the compression of sea ice with more realistic heterogeneous initial ice conditions, and study if the previous results with an homogeneous ice cover still apply.

In Chapter 8, I present the general conclusions of this thesis and give an outlook for future work.

Remark: Chapters 4 and 5 are unaltered journal papers compiled with my co-authors. This might create some repetitions and some inconsistencies regarding the utilization of the first person plural and style.

Chapter 2

Sea ice viscous-plastic rheologies

The question inevitably arises, “What is the possible use of Rheology?”

— *The New Science of Rheology* – Eugene C. Bingham (1933)

2.1 Sea ice dynamics

2.1.1 Sea ice momentum equation and rheology

Ice drift is computed from the sea ice momentum equations

$$\rho h \frac{\partial \vec{u}}{\partial t} = -\rho h f \vec{k} \times \vec{u} + \vec{\tau}_{air} + \vec{\tau}_{ocean} - \rho h \nabla \phi(0) + \boxed{\nabla \cdot \boldsymbol{\sigma}}, \quad (2.1)$$

where ρ is the ice density, h is the grid cell averaged sea ice thickness, \vec{u} is the velocity field, f is the Coriolis parameter, \vec{k} is the vertical unit vector, $\vec{\tau}_{air}$ is the surface air stress, $\vec{\tau}_{ocean}$ is the ocean drag, $\nabla \phi(0)$ is the acceleration from the tilt of sea surface height, and $\boldsymbol{\sigma}$ is the vertically integrated internal ice stress tensor.

The form of the $\boldsymbol{\sigma}$ tensor gives the rheology, the material properties of sea ice. Coon et al. (1974) showed that free drift does not explain the dynamics of sea ice, therefore sea ice internal stresses need to be included. The internal stresses of sea ice includes the interactions between the ice floes at a small scales, and defines the mechanics of the sea ice in the model. Note that I describe different viscous-plastic (VP) *rheologies* (plural), within a VP *framework* (singular):

Framework refers to the material properties given to the simulated medium. For the Viscous-Plastic (VP) framework it means: Plastic for high deformations and Viscous for small deformations. Other existing frameworks are: Elastic-Plastic (EP, Coon et al., 1974), Elasto-Brittle (EB, Girard et al., 2011), or Maxwell-Elasto-Brittle (MEB, Dansereau et al., 2016). By definition, an elastic deformations is reversible, viscous and plastic deformation are not reversible, and brittle behavior implies a physical fracture, represented by the change of physical properties like the maximal ice strength P or Elastic modulus E .

Rheology in the refers to the coupling between a *yield curve* and a *flow rule* in a given framework. **(1)** The *yield curve* is the limit in stress at which the material change from one regime to another, from one limited to small deformations to a behavior that will allow large deformation events and limits the building of additional stress. For example, the yield curve marks the transition from elastic to plastic, viscous to plastic, elastic to brittle or viscous-elastic to brittle. Yield curves can take several shapes in stress space and this shape sets for which configuration of stress the ice will deform, e.g. for which ratio of shear to normal stress. Different yield curves have been compared in multiple studies at both different scales and resolution, e.g.

in Ip et al. (1991) or in (Zhang and Rothrock, 2005). **(2)** The *flow rule* determines how the medium deforms when the yield curve is reached. From the point in stress space where the medium deforms, the medium can deform with different directions in shear or in divergence. The flow rule can be normal to the yield curve (This is called normal-flow rule or associated flow rule) or can be set independently. Several yield curves have been implemented in models (e.g., Tremblay and Mysak, 1997). Therefore, two models sharing the same framework but different yield curves are two different rheologies and two different framework sharing the same yield curve are also two different rheologies. The same applies to different flow rules. Note that this is different in a brittle rheology, like the EB or MEB sea ice rheologies.

In this work, I focus on the Viscous-Plastic framework, and discuss the different Viscous-Plastic rheologies used in the past, or currently in use for sea ice modeling.

2.1.2 Viscous-Plastic framework

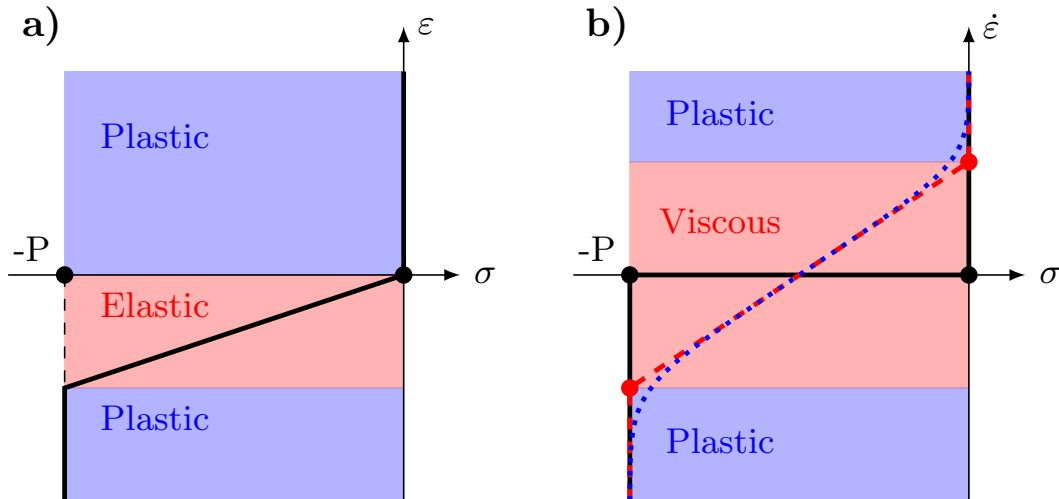


Figure 2.1: a) Relationship between stress σ and strain ϵ in an Elastic-Plastic 1D model. b) Relationship between stress σ and strain rate $\dot{\epsilon} = \frac{\partial \epsilon}{\partial t}$ in a 1D model. Black lines show the Plastic behavior, the red dashed line shows the Viscous-Plastic (VP) behavior, and the blue dashed line show VP behavior with a smooth regularization (Lemieux and Tremblay, 2009). Figure adapted from Hibler (1979).

The first dynamic sea ice models used the Elastic-Plastic framework (Coon et al., 1974). In order to include elasticity, it was necessary to keep a memory of the strain, as the elastic stress is function of the strain and not the strain rate (panel **a** on Figure 2.1). Having such a relation makes sea ice model harder to implement because it requires the use of a Lagrangian implementation (Hibler, 1979).

Hibler (1979) describes a set constitutive equations using the Viscous-Plastic (VP) framework. Using viscous instead of elastic properties allows to use strain rates $\dot{\epsilon}$ instead of strain ϵ , simplifying the numerical formulation of sea ice models. Figure 2.1b shows the behavior of stress relative to strain-rates $\dot{\epsilon}$. The VP rheologies use quantities defined the bulk and shear viscosities ζ and η . These two quantities define the viscosity during compression/tension deformation and shear deformations, respectively. Viscosities can be seen as the resistance of a fluid to deformations, or

its thickness. Slow deformations are modeled as a slow viscous creep with constant viscosities. Fast deformations are modeled as permanent plastic deformations which imply a constant stress, so viscosities vary to ensure that the stress is independent of strain rate: the viscosities become large when the deformations become small. Following the Reiner-Rivlin model for non-elastic solids (Astarita and Marrucci, 1974):

$$\boldsymbol{\sigma} = \alpha \mathbf{I} + \beta \dot{\boldsymbol{\epsilon}} + \gamma \dot{\boldsymbol{\epsilon}}^2 \quad (2.2)$$

where α , β , and γ are functions of the strain rates and the state variables, or functions of ζ and η and the state variables. The second order term is neglected, i.e. $\gamma = 0$. In this formulation, to transition from plastic deformation to viscous creep, ζ and η are set to have a maximum value. When this value is reached, the stress is only a linear function of the strain rates and tends to zero when they tend to zero.

Figure 2.1 shows a 1D example, therefore the yield conditions are points, shown as black dots at the stresses position $\sigma = -P$ and $\sigma = 0$. When sea ice is modeled as a 2D medium, the yield condition is replaced by a more complex condition defined as function of the stress invariants, defined in Section 2.1.3. This condition can be represented a 2D yield curve (Figure 2.2). As for the 1D case, stresses are constant for all strain rates during plastic deformation, show as a blue line, while viscous states are enclosed inside the yield curve, shown as red area.

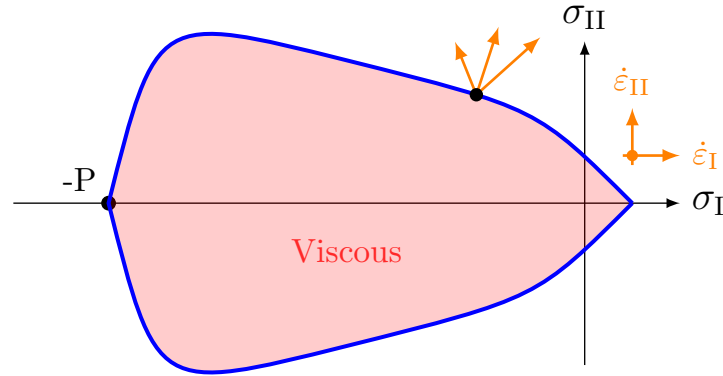


Figure 2.2: Arbitrary yield curve: The plastic yield condition is shown in blue with different flow direction and flow rates. The viscous states enclosed in the yield curve are shown in red.

2.1.3 Stress tensors definition

The stress tensor, or Cauchy stress tensor, $\boldsymbol{\sigma}$ is a tensor expressing the stress applied on a sea ice element of the model. In our 2D model, the stress tensor is a 2×2 matrix defined as

$$\begin{pmatrix} \sigma_{11} & \sigma_{12} \\ \sigma_{21} & \sigma_{22} \end{pmatrix} \quad (2.3)$$

The stress tensor is often transformed in terms of principal stresses σ_1 and σ_2 or stress invariants σ_I and σ_{II} . The principal stresses σ_1 and σ_2 are the principal

components or eigenvalues of the stress tensor on a sea ice element. The principal stresses σ_1 and σ_2 can be expressed as a function of σ_{ij} as :

$$\sigma_1 = \frac{1}{2} \left(\sigma_{11} + \sigma_{22} + \sqrt{(\sigma_{11} - \sigma_{22})^2 + 4\sigma_{12}^2} \right), \quad (2.4)$$

$$\sigma_2 = \frac{1}{2} \left(\sigma_{11} + \sigma_{22} - \sqrt{(\sigma_{11} - \sigma_{22})^2 + 4\sigma_{12}^2} \right), \quad (2.5)$$

This change of coordinates can then be represented as a rotation of the coordinates by angle ψ . This angle is (Tremblay and Mysak, 1997):

$$\tan(2\psi) = \frac{2\sigma_{12}}{\sigma_{11} - \sigma_{22}}. \quad (2.6)$$

See Figure 3.2 for an illustration of ψ . Any linear combination of the principal stresses are stress invariants. One common sets of stress invariants are the mean normal stress (σ_I) and the maximal shear stress (σ_{II}). They define the Mohr's circle (see Chapter 3) and can be written as

$$\sigma_I = \frac{1}{2}(\sigma_1 + \sigma_2) = \frac{1}{2}(\sigma_{11} + \sigma_{22}), \quad (2.7)$$

$$\sigma_{II} = \frac{1}{2}(\sigma_1 - \sigma_2) = \frac{1}{2}\sqrt{(\sigma_{11} - \sigma_{22})^2 + 4\sigma_{12}^2}. \quad (2.8)$$

2.1.4 Strain rates definition

The strain-rate tensor describes the deformation in a medium based on the velocity inside the medium. One important assumption in sea ice models is that the stress and strain rate axes are aligned. The strain rates tensor is also a 2x2 matrix is defined as

$$\dot{\epsilon}_{ij} = \frac{1}{2} \left(\frac{\partial u_i}{\partial x_j} + \frac{\partial u_j}{\partial x_i} \right), \quad (2.9)$$

where $u_1 = u$ and $u_2 = v$ are the ice velocity in x and y direction, respectively. The strain rate tensor can also be expressed as principal strain rates

$$\dot{\epsilon}_1 = \frac{1}{2} \left((\dot{\epsilon}_{11} + \dot{\epsilon}_{22}) + \sqrt{(\dot{\epsilon}_{11} - \dot{\epsilon}_{22})^2 + 4\dot{\epsilon}_{12}^2} \right), \quad (2.10)$$

$$\dot{\epsilon}_2 = \frac{1}{2} \left((\dot{\epsilon}_{11} + \dot{\epsilon}_{22}) - \sqrt{(\dot{\epsilon}_{11} - \dot{\epsilon}_{22})^2 + 4\dot{\epsilon}_{12}^2} \right), \quad (2.11)$$

and the invariant strain rates $\dot{\epsilon}_I$ the divergence and $\dot{\epsilon}_{II}$ the total shear deformation as

$$\dot{\epsilon}_I = \dot{\epsilon}_1 + \dot{\epsilon}_2 = \dot{\epsilon}_{11} + \dot{\epsilon}_{22}, \quad (2.12)$$

$$\dot{\epsilon}_{II} = \dot{\epsilon}_1 - \dot{\epsilon}_2 = \sqrt{(\dot{\epsilon}_{11} - \dot{\epsilon}_{22})^2 + 4\dot{\epsilon}_{12}^2}. \quad (2.13)$$

Shear deformation can be induced when $\dot{\epsilon}_{11}$ and $\dot{\epsilon}_{22}$ have different values; therefore, $\dot{\epsilon}_{II} \neq \dot{\epsilon}_{12}$.

2.1.5 Defining the VP constitutive equations

2.1.5.1 Constitutive Equations

The constitutive equations are a set of equations linking the stress tensor to the strain tensor in the form

$$\boldsymbol{\sigma} = f(\boldsymbol{\varepsilon}). \quad (2.14)$$

Therefore, each values of σ_{ij} is computed from the values of $\dot{\varepsilon}_{ij}$ and used in the sea ice momentum Equation (2.1). It is the set of equation that defines the rheology of sea ice, influence the fracture pattern, the fracture angle, and the opening or closing of the ice.

2.1.5.2 Yield Curve

In VP models, the yield curve, or yield condition, is the limit in the stress space where the ice will change from slow viscous creep to fast permanent plastic deformation. Because sea ice is modeled as a thin 2D material, the symmetrical stress tensor has three components, and the yield curve can expressed as a two dimensional curve in the stress invariants or the principal stresses. This yield curve encloses the viscous stress states, while states on the curve are deforming plastically. In the original paper (Hibler, 1977), for coarse resolution, the viscous states were used as a regularization for small strains that would otherwise induce high viscosities and slow down the numerical solver. Viscous states are created in between narrow zones of plastic deformation (Hutchings et al., 2005). These zones of plastic deformation are called Linear Kinematic Features (LKFs).

The yield curve is expressed as function of the stresses (σ_{ij}) and the state variables (χ) as

$$F(\sigma_{ij}, \chi) = 0. \quad (2.15)$$

This equation determines only if the deformation is plastic or viscous, but it does not determine how the deformation will take place and it does not allow to close the system of equations to build the constitutive equations. For this, a plastic potential is needed, and therefore, a flow rule.

2.1.5.3 Plastic potential and flow rule

The plastic potential determine in which direction the deformation will happen for each stress state on the yield curve (Kelly, 2020). It is a function that depends on stresses and state variables, as the yield curve,

$$G(\sigma_{ij}, \chi) = 0. \quad (2.16)$$

The direction of the deformation, or *flow rule*, is perpendicular to the plastic potential. This is expressed mathematically by

$$\dot{\varepsilon}_{ij} = \lambda \frac{\partial G}{\partial \sigma_{ij}}, \quad (2.17)$$

where $\lambda > 0$ is the *flow rate* to be determined.

Using this equation, it is possible to write a system of equation with 5 equations (4 from Eq. 2.17 and 1 from Eq. 2.15) for 5 unknowns ($\sigma_{11}, \sigma_{22}, \sigma_{12}, \sigma_{12}, \lambda$). Solving

this system of equations allows us to write the constitutive equations for the sea ice model.

If the plastic potential and the yield curve are the same function, $G = F$, the flow rule is perpendicular to the yield curve and this is then called an *associative* or *normal* flow rule. The most common VP sea ice model (Hibler, 1979) uses a normal flow rule, although some non-normal flow rules have also been used (Ip et al., 1991; Tremblay and Mysak, 1997; Hibler and Schulson, 2000).

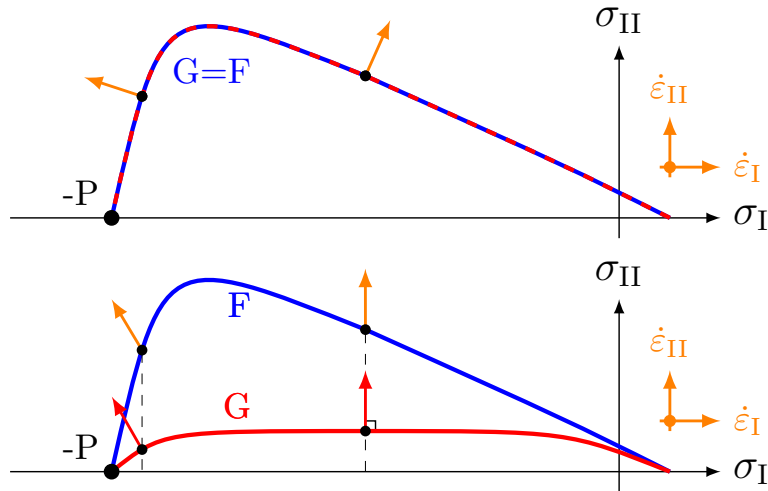


Figure 2.3: Example of arbitrary yield curve with normal (top) and non-normal flow rule (bottom). F (blue) is the yield curve and G (red) is the plastic potential. The orange arrows illustrate the flow rule defined by the plastic potential.

2.1.5.4 Ice strength in sea ice models

One state variable is common to every sea ice rheology described in Section 2.2, the maximal compressive strength P . P is defined to represent the strength of an agglomerate of ice floes in a coarse resolution Eulerian model. It takes into account the ice concentration of a grid cell and the mean thickness. This variable represents the maximal compressive stress that sea ice can bear in uniform compression, before ridging. P is defined by

$$P = P_0 h e^{-C^*(1-A)}, \quad (2.18)$$

where C^* is a free parameter (with a default value $C^* = 20$), h is the mean ice thickness, A is the concentration of ice in the grid cell, and P_0 is the ice strength of 1 m ice and 100% concentration. Some other parameters of the rheologies are function of P , e.g. the tensile strength T is usually defined as $T = k_t \cdot P$ with $k_t > 0$ the tensile factor (König Beatty and Holland, 2010).

The ice strength P can also be defined as function of the Ice Thickness Distribution (ITD). (Rothrock, 1975b) defined the ITD as a way to represent different ice thicknesses in the same grid cell. Each grid cell have ice thickness categories, a function compute the sea ice strength from the amount of ice in each categories. It is also possible to use a mean ice thickness from the distribution (Ungermann et al., 2017).

2.1.5.5 Energy considerations, symmetry and associated flow rule

In the momentum equation, the force per unit of area by the internal stress divergence in sea ice is given by

$$F_{\sigma,i} = \partial_j \sigma_{ij}. \quad (2.19)$$

Multiplying this force with the drift vector u_i yields the kinetic energy dissipation equation (in tensor notation):

$$W = u_j \partial_i \sigma_{ij}. \quad (2.20)$$

The factor rule of differentiation yields the expression

$$W = \partial_i (u_j \sigma_{ij}) - (\partial_i u_j) \sigma_{ij} \quad (2.21)$$

that can be rewritten by using the symmetry $\sigma_{ij} = \sigma_{ji}$ as

$$W = \partial_i (u_j \sigma_{ij}) - \dot{\epsilon}_{ij} \sigma_{ij}, \quad (2.22)$$

where the first member is the total energy dissipation (kinetic and internal stress), therefore the second term is the energy dissipation of the internal forces (Ukita and Moritz, 1995).

$$W_{int} = \dot{\epsilon}_{ij} \sigma_{ij} \quad (2.23)$$

For a stable plastic medium Drucker's postulate requires that dissipation of energy from internal stress be positive (Kelly, 2020), i.e. $d\dot{\epsilon}_{ij} d\sigma_{ij} \geq 0$. In an ideal plastic medium, an increment of stress $d\sigma_{ij}$ should create a stress also lying on the yield curve F , Equation (2.15), as

$$F(\sigma_{ij} + d\sigma_{ij}) = F(\sigma_{ij}) = 0, \quad (2.24)$$

because stress are constant at the yield condition. If $F(\sigma_{ij} + d\sigma_{ij})$, then

$$F(\sigma_{ij} + d\sigma_{ij}) = F(\sigma_{ij}) + \frac{\partial F}{\partial \sigma_{ij}} d\sigma_{ij} + O^2(d\sigma_{ij}), \quad (2.25)$$

which means that, neglecting second order terms,

$$\frac{\partial F}{\partial \sigma_{ij}} d\sigma_{ij} = 0. \quad (2.26)$$

If the stress state is on the yield curve, then the stress is constant $d\sigma = 0$ and therefore $d\dot{\epsilon}_{ij} d\sigma_{ij} = 0$, justifying the use of the normal flow rule to have a stable plastic material

$$\dot{\epsilon}_{ij} = \gamma \frac{\partial F}{\partial \sigma_{ij}}. \quad (2.27)$$

If a non-normal yield curve is used, the generality of the stability is lost, some deformations could lead to energy increase as $d\dot{\epsilon}_{ij} d\sigma_{ij} < 0$.

It is important to note that the symmetry of σ_{ij} cannot be used for deriving the constitutive law from the yield curve and the plastic potential. Using the symmetry before differentiating would be a change in the tensorial formulation. The constitutive equations need to be derived without the assumption of symmetry to get a general formulation, then symmetry can be used after the derivation.

2.2 VP Rheologies: Yield curves and flow rules

2.2.1 Elliptical yield curve with normal flow rule

2.2.1.1 Definition of the elliptical yield curve

The elliptical yield curve is the standard in VP sea ice models today. I describe here the complete derivation of the constitutive equations of the elliptical yield curve with the associative flow-rule and tensile strength.

First, I define the shape of the yield curve in the invariant space: The ellipse tips of the semi-major axis are at $-P$ ($P > 0$, the maximal compressive stress) and the T ($T > 0$, the maximal tensile stress), the center of the ellipse is at the point $\frac{-P+T}{2}$ on the σ_I axis. The maximal shear strength that is a factor the length of the ellipse in the compressive/tensile axis $S = \frac{1}{e} \cdot \frac{P+T}{2}$. Therefore, the elliptical yield curve equation is

$$\left(\frac{\sigma_I + \frac{P-T}{2}}{\frac{P+T}{2}} \right)^2 + \left(\frac{\sigma_{II}}{\frac{P+T}{2e}} \right)^2 = 1, \quad (2.28)$$

and with $T = k_t \cdot P$, where k_t is the tensile strength factor (König Beatty and Holland, 2010),

$$\left(\frac{\sigma_I + P \frac{1-k_t}{2}}{P \frac{1+k_t}{2}} \right)^2 + \left(\frac{\sigma_{II}}{P \frac{1+k_t}{2e}} \right)^2 = 1. \quad (2.29)$$

The equation above can be manipulated to express σ_{II} as function of σ_I

$$\sigma_{II} = \frac{1}{e} \sqrt{P^2 k_t - \sigma_I(\sigma_I + P - P k_t)}, \quad (2.30)$$

where $e = \frac{a}{b}$ is the ellipse aspect ratio with the semi-major half-axes a and b (shown in blue in Figure 2.4). The ellipse aspect ratio e defines the shear strength $S^* = \frac{P^*}{2e}$ of the material as a fraction of its compressive strength (Bouchat and Tremblay, 2017). From equation 2.29, the yield condition in the physical space σ_{ij} becomes

$$F_{ell} = \left(\frac{(\sigma_{11} + \sigma_{22}) + P \frac{1-k_t}{2}}{P \frac{1+k_t}{2}} \right)^2 + \left(\frac{\frac{1}{2} \sqrt{(\sigma_{11} - \sigma_{22})^2 + 4\sigma_{12}\sigma_{21}}}{P \frac{1+k_t}{2e}} \right)^2 - 1 = 0. \quad (2.31)$$

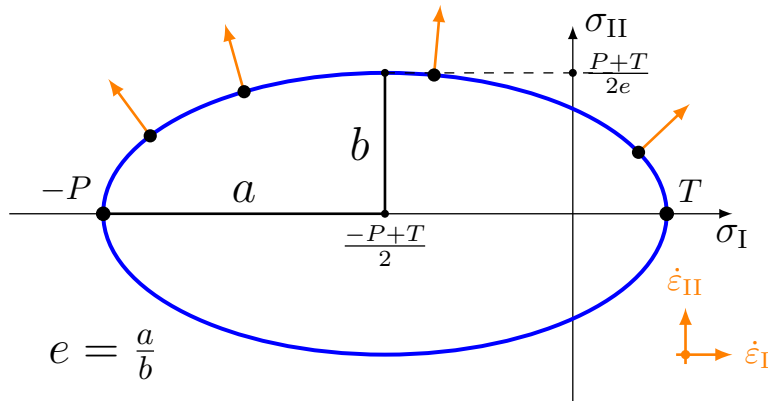


Figure 2.4: Elliptical yield curve in stress-invariant space with tensile strength and normal flow rule

2.2.1.2 Normal flow rule

I use the normal flow rule ($G = F_{ell}$) to link strain rates and stress

$$\dot{\epsilon}_{ij} = \lambda \frac{\partial F_{ell}}{\partial \sigma_{ij}}. \quad (2.32)$$

Applying this flow rule to expression (2.31) yields four equations:

$$\begin{aligned} \dot{\epsilon}_{11} &= \lambda \frac{\partial F_{ell}}{\partial \sigma_{11}} = \lambda \left\{ \frac{1}{P^2(1+k_t)^2} 2(\sigma_{11} + \sigma_{22} + P(1-k_t)) + \frac{e^2}{P^2(1+k_t)^2} 2(\sigma_{11} - \sigma_{22}) \right\} \\ &= \frac{2\lambda}{P^2(1+k_t)^2} (\sigma_{11} + \sigma_{22} + P(1-k_t)) + \frac{2\lambda e^2}{P^2(1+k_t)^2} (\sigma_{11} - \sigma_{22}) \end{aligned} \quad (2.33)$$

$$\begin{aligned} \dot{\epsilon}_{22} &= \lambda \frac{\partial F_{ell}}{\partial \sigma_{22}} = \lambda \left\{ \frac{1}{P^2(1+k_t)^2} 2(\sigma_{11} + \sigma_{22} + P(1-k_t)) - \frac{e^2}{P^2(1+k_t)^2} 2(\sigma_{11} - \sigma_{22}) \right\} \\ &= \frac{2\lambda}{P^2(1+k_t)^2} (\sigma_{11} + \sigma_{22} + P(1-k_t)) - \frac{2\lambda e^2}{P^2(1+k_t)^2} (\sigma_{11} - \sigma_{22}) \end{aligned} \quad (2.34)$$

$$\dot{\epsilon}_{12} = \lambda \frac{\partial F_{ell}}{\partial \sigma_{12}} = \lambda \frac{e^2}{P^2(1+k_t)^2} 4\sigma_{21} = \frac{4\lambda e^2}{P^2(1+k_t)^2} \sigma_{21} \quad (2.35)$$

$$\dot{\epsilon}_{21} = \lambda \frac{\partial F_{ell}}{\partial \sigma_{21}} = \lambda \frac{e^2}{P^2(1+k_t)^2} 4\sigma_{12} = \frac{4\lambda e^2}{P^2(1+k_t)^2} \sigma_{12} \quad (2.36)$$

Introducing the convenient abbreviations $\sigma_+ = \sigma_{11} + \sigma_{22}$ and $\sigma_- = \sigma_{11} - \sigma_{22}$ and similarly for the strain rate tensor components $\dot{\epsilon}_{ij}$ one can rewrite the first two equations:

$$\begin{aligned} \dot{\epsilon}_+ &= \frac{4\lambda}{P^2(1+k_t)^2} (\sigma_+ + P(1-k_t)) \\ \dot{\epsilon}_- &= \frac{4\lambda e^2}{P^2(1+k_t)^2} \sigma_- \end{aligned}$$

This gives the following expressions for the components of $\boldsymbol{\sigma}$:

$$\sigma_+ = \frac{P^2(1+k_t)^2 \dot{\epsilon}_+}{4\lambda} - P(1-k_t) \quad (2.37)$$

$$\sigma_- = \frac{P^2(1+k_t)^2 \dot{\epsilon}_-}{4\lambda e^2} \quad (2.38)$$

$$\sigma_{12} = \frac{P^2(1+k_t)^2 \dot{\epsilon}_{21}}{4\lambda e^2} \quad (2.39)$$

$$\sigma_{21} = \frac{P^2(1+k_t)^2 \dot{\epsilon}_{12}}{4\lambda e^2}. \quad (2.40)$$

2.2.1.3 Consistency condition $F = 0$

An expression for λ is found by inserting these expressions (2.37) to (2.40) into (2.31) with the consistency condition $F = 0$:

$$\begin{aligned}
1 &= \left(\frac{\sigma_+ + P(1 - k_t)}{P(1 + k_t)} \right)^2 + \frac{\sigma_-^2 + 4\sigma_{12}\sigma_{21}}{(P(1 + k_t)/e)^2} \\
&= \left(\frac{\frac{P^2(1+k_t)^2\dot{\epsilon}_+}{4\lambda} - P(1 - k_t) + P(1 - k_t)}{P(1 + k_t)} \right)^2 \\
&\quad + \frac{\left(\frac{P^2(1+k_t)^2\dot{\epsilon}_-}{4\lambda e^2} \right)^2 + 4 \left(\frac{P^2(1+k_t)^2}{4\lambda e^2} \right)^2 \dot{\epsilon}_{12}\dot{\epsilon}_{21}}{(P(1 + k_t)/e)^2} \\
&= \frac{P^2(1 + k_t)^2\dot{\epsilon}_+^2}{4^2\lambda^2} + \frac{P^2(1 + k_t)^2\dot{\epsilon}_-^2}{4^2\lambda^2 e^2} + 4 \frac{P^2(1 + k_t)^2\dot{\epsilon}_{12}\dot{\epsilon}_{21}}{4^2\lambda^2 e^2} \\
\Leftrightarrow \lambda &= \frac{P(1 + k_t)}{4} \sqrt{\dot{\epsilon}_+^2 + e^{-2}(\dot{\epsilon}_-^2 + 4\dot{\epsilon}_{12}\dot{\epsilon}_{21})} = \frac{P(1 + k_t)}{4} \Delta \tag{2.41}
\end{aligned}$$

with

$$\begin{aligned}
\Delta &= \sqrt{\dot{\epsilon}_+^2 + e^{-2}(\dot{\epsilon}_-^2 + 4\dot{\epsilon}_{12}\dot{\epsilon}_{21})} \\
&= \sqrt{(\dot{\epsilon}_{11} + \dot{\epsilon}_{22})^2 + e^{-2}[(\dot{\epsilon}_{11} - \dot{\epsilon}_{22})^2 + 4\dot{\epsilon}_{12}\dot{\epsilon}_{21}]}. \tag{2.42}
\end{aligned}$$

Inserting λ into (2.37) to (2.39) gives

$$\begin{aligned}
\sigma_+ &= \frac{P(1 + k_t)\dot{\epsilon}_+}{\Delta} - P(1 - k_t) = 2\zeta \dot{\epsilon}_+ - P(1 - k_t) \\
\sigma_- &= \frac{P(1 + k_t)\dot{\epsilon}_-}{\Delta e^2} = 2\eta \dot{\epsilon}_- \\
\sigma_{12} &= \frac{P(1 + k_t)\dot{\epsilon}_{21}}{\Delta e^2} = 2\eta \dot{\epsilon}_{21} \\
\sigma_{21} &= \frac{P(1 + k_t)\dot{\epsilon}_{12}}{\Delta e^2} = 2\eta \dot{\epsilon}_{12}
\end{aligned}$$

where the bulk and shear viscosities

$$\zeta = \frac{P(1 + k_t)}{2\Delta} \tag{2.43}$$

$$\eta = \frac{P(1 + k_t)}{2\Delta e^2} = \frac{\zeta}{e^2} \tag{2.44}$$

have been introduced. Finally,

$$\begin{aligned}
\sigma_{11} &= \frac{1}{2}(\sigma_+ + \sigma_-) = \zeta(\dot{\epsilon}_{11} + \dot{\epsilon}_{22}) + \eta(\dot{\epsilon}_{11} - \dot{\epsilon}_{22}) - \frac{P(1 - k_t)}{2} \\
&= 2\eta\dot{\epsilon}_{11} + (\zeta - \eta)(\dot{\epsilon}_{11} + \dot{\epsilon}_{22}) - \frac{P(1 - k_t)}{2} \\
\sigma_{22} &= \frac{1}{2}(\sigma_+ - \sigma_-) = \zeta(\dot{\epsilon}_{11} + \dot{\epsilon}_{22}) - \eta(\dot{\epsilon}_{11} - \dot{\epsilon}_{22}) - \frac{P(1 - k_t)}{2} \\
&= 2\eta\dot{\epsilon}_{22} + (\zeta - \eta)(\dot{\epsilon}_{11} + \dot{\epsilon}_{22}) - \frac{P(1 - k_t)}{2} \\
\sigma_{12} &= 2\eta\dot{\epsilon}_{21}, \quad \sigma_{21} = 2\eta\dot{\epsilon}_{12},
\end{aligned}$$

which can be summarized as

$$\sigma_{ij} = 2\eta \dot{\epsilon}_{ji} + \delta_{ij} \left([\zeta - \eta](\dot{\epsilon}_{11} + \dot{\epsilon}_{22}) - \frac{P(1 - k_t)}{2} \right), \quad (2.45)$$

or for symmetric stress and strain rate tensors ($\sigma_{ij} = \sigma_{ji}$ and $\dot{\epsilon}_{ij} = \dot{\epsilon}_{ji}$):

$$\sigma_{ij} = 2\eta \boxed{\dot{\epsilon}_{ij}} + \delta_{ij} \left([\zeta - \eta](\dot{\epsilon}_{11} + \dot{\epsilon}_{22}) - \frac{P(1 - k_t)}{2} \right). \quad (2.46)$$

The constitutive equation (2.46) can be written in terms of the principal stresses

$$\sigma_1 = (\zeta + \eta)\dot{\epsilon}_1 + (\zeta - \eta)\dot{\epsilon}_2 - \frac{P(1 - k_t)}{2}, \quad (2.47)$$

$$\sigma_2 = (\zeta - \eta)\dot{\epsilon}_1 + (\zeta + \eta)\dot{\epsilon}_2 - \frac{P(1 - k_t)}{2}, \quad (2.48)$$

or in terms of the stress invariants

$$\sigma_I = 2\zeta\dot{\epsilon}_I - \frac{P(1 - k_t)}{2}, \quad (2.49)$$

$$\sigma_{II} = 2\eta\dot{\epsilon}_{II}. \quad (2.50)$$

In this abbreviation, the strain rate invariants are the divergence $\dot{\epsilon}_I = \dot{\epsilon}_{11} + \dot{\epsilon}_{22}$, and the maximum shear strain rate $\dot{\epsilon}_{II} = \sqrt{(\dot{\epsilon}_{11} + \dot{\epsilon}_{22})^2 + 4\dot{\epsilon}_{12}^2}$.

2.2.1.4 Viscous deformation

As explained in Section 2.1.2, when sea ice deformation becomes small ($\dot{\epsilon}_{ij} \rightarrow 0$), Δ becomes very small. From there definition, the viscosities η and ζ becomes arbitrary large (Equation 2.43 and 2.44). Having viscosities tending to infinity is a numerical difficulty. To regularize this behavior and introduce viscous behavior, ζ is capped to a maximum values ζ_{\max} , and, by its definition, η is capped to $\eta_{\max} = \frac{\zeta_{\max}}{e^2}$ (Hibler, 1979).

Viscous deformation is very slow in comparison to the observed deformation rates in the Arctic (Stern et al., 1995). Viscous deformation take place for deformation rate $\leq 10^{-9} \text{ s}^{-1}$. In other words, viscous deformation have a timescale of 27 years, this is very large in comparison to the observed deformation rate in the Arctic.

2.2.1.5 Replacement pressure

With the formulation above, if no deformation is applied, sea ice is in a viscous state (i.e., $\zeta = \zeta_{\max}$). Then, the stress states are at the coordinates ($\sigma_I = \frac{P}{2}$, $\sigma_{II} = 0$). For nonzero stress ($\sigma_I = P/2$), viscous flow to adjacent cells follows from the momentum equations. Ip et al. (1991) and Hibler and Ip (1995) introduced the replacement pressure to remove this behavior. The equation of ζ (2.43) is inverted to express the replacement pressure P_{repl} as

$$P_{repl} = \frac{2\Delta\zeta}{1 + k_t}. \quad (2.51)$$

So that, if $\dot{\epsilon}_{ij} \rightarrow 0$, then $\zeta = \zeta_{\max}$ and $\Delta \rightarrow 0$ then $P_{repl} \rightarrow 0$. P_{repl} replaces the P in Equation (2.46) so that without external forcing, resting ice remains at rest.

2.2.2 Elliptical yield curve with non-normal flow rule

The elliptical yield curve with an associative flow rule is the most commonly used VP rheology in sea ice models, because its definition is simple and makes the momentum equations relatively simple to solve at coarse resolution. However, this yield curve leads to fracture patterns that do not compare to observations (Ringeyen et al., 2019, Chapter 4). The elliptical yield curve has only been used with the normal flow rule such that it is not possible to separate the effect of the yield curve shape and the effect of the flow rule during fracture events. To study the different effects of both parts, I derive the constitutive equations for an elliptical yield curve with non-normal flow rule.

To compute constitutive equations with a non-normal flow rule, I use a plastic potential different from the yield curve. The elliptical yield condition F as function of P and e_F is defined by

$$F_{ell} = \left(\frac{\sigma_{11} + \sigma_{22} + P(1 - k_t)}{P(1 + k_t)} \right)^2 + \frac{(\sigma_{11} - \sigma_{22})^2 + 4\sigma_{21}\sigma_{12}}{\left(\frac{P(1+k_t)}{e_F} \right)^2} - 1 = 0, \quad (2.52)$$

when I define the elliptical plastic potential G_{ell} as function of P and e_G by

$$G_{ell} = \left(\frac{\sigma_{11} + \sigma_{22} + P(1 - k_t)}{P(1 + k_t)} \right)^2 + \frac{(\sigma_{11} - \sigma_{22})^2 + 4\sigma_{21}\sigma_{12}}{\left(\frac{P(1+k_t)}{e_G} \right)^2} - 1 = 0. \quad (2.53)$$

I use another ellipse as a plastic potential because it makes the computation and resulting constitutive equations similar to the normal flow rule case, and it requires fewer modifications to the sea ice model. The numbers e_F and e_G are elliptical ratios for the yield condition F and plastic potential G .

Using the same method as in Section 2.2.1, I derive the viscosities

$$\zeta = \frac{P(1 + k_t)}{2\Delta} \quad \text{and} \quad \eta = \frac{\zeta}{e_G^2} = \frac{P(1 + k_t)}{2e_G^2\Delta} \quad (2.54)$$

where

$$\Delta = \sqrt{(\dot{\epsilon}_{11} - \dot{\epsilon}_{22})^2 + \frac{e_F^2}{e_G^4}((\dot{\epsilon}_{11} - \dot{\epsilon}_{22})^2 + 4\dot{\epsilon}_{12}^2)} \quad (2.55)$$

with the same definition of stress tensor σ_{ij}

$$\sigma_{ij} = 2\eta\dot{\epsilon}_{ij} + (\zeta - \eta)\dot{\epsilon}_{kk}\delta_{ij} - \frac{P(1 - k_t)}{2}\delta_{ij}. \quad (2.56)$$

These new constitutive equations describe a rheology with an elliptical yield curve and flow rule that changes with the value of e_G . If $e_F = e_G$, Δ reduces to Equation (2.42) and the rheology is again the elliptical yield curve with normal flow rule. Changing the value of e_G to a value larger than e_F decreases the divergent and convergent motion and increases the shear deformation (Figure 2.5), and vice-versa for $e_G < e_F$. Using a high value for e_G , i.e. for $e_G = 5$, would favor almost pure shear deformations and restrict high divergent or convergent motion to the tips of the elliptical yield curve ($\sigma_I \simeq -1$ or $\sigma_I \simeq T$).

However, changing e_G does not change the sign of the divergence, convergent motion stay convergent and divergence motion stay divergence, only the ratio of shear and divergence or shear and convergence changes. In order to change the convergent or divergent motion, a different plastic potential function G is needed.

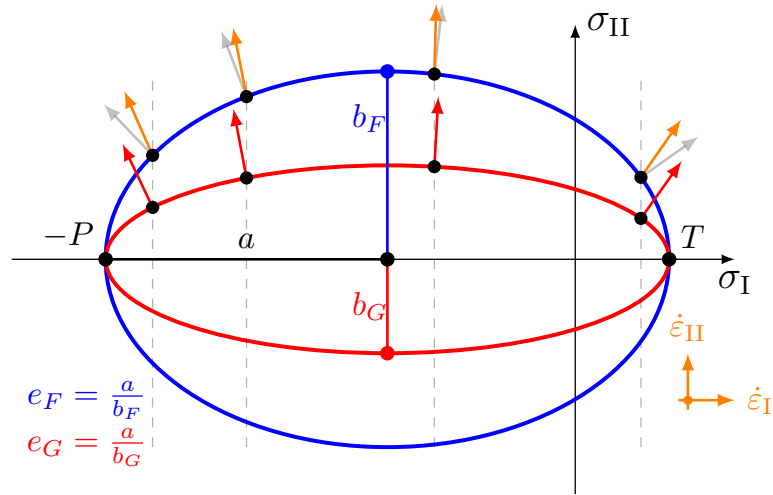


Figure 2.5: Yield curve with non-normal flow rule. The blue curve is the yield curve while the red curve is the plastic potential that defines the flow rule, shown with the orange arrows. The grey arrows illustrate the normal flow rule for this yield curve.

2.2.3 Mohr–Coulomb yield curve with shear flow rule

2.2.3.1 Derivation of the viscosities

The Mohr–Coulomb criterion has been used for many year for modeling the dynamics of granular material such as sand or clay (Verruijt, 2018). This yield curve is linked to the idea of the Mohr’s circle. The physics of the Mohr’s circle and Mohr’s criterion are described in Chapter 3, Section 3.2. Note that this yield curve is not build by using the yield curve and the plastic potential, but by setting a different η and ζ to have a Mohr–Coulomb shaped yield curve. I use the formulation of the elliptical yield curve and modify them to define the viscosities with the Mohr–Coulomb limbs.

I describe below the complete derivation of Mohr–Coulomb yield curve, inspired by the a formulation already used in sea ice modeling (Ip et al., 1991). I start from the elliptical yield curve constitutive equations

$$\sigma_{ij} = 2\eta\dot{\epsilon}_{ij} + \delta_{ij}(\zeta - \eta)\dot{\epsilon}_{kk} - \delta_{ij}\frac{P(1 - k_t)}{2}, \quad (2.57)$$

with

$$\dot{\epsilon}_{kk} = \dot{\epsilon}_{11} + \dot{\epsilon}_{22}. \quad (2.58)$$

The definition of the bulk viscosity ζ is now defined by

$$\zeta = \min \left\{ \zeta_{max}, \frac{P(1 + k_t)}{2|\dot{\epsilon}_{kk}|} \right\} \quad (2.59)$$

with the maximum value for viscous deformation

$$\zeta_{max} = \frac{P(1 + k_t)}{2\dot{\epsilon}_{kk,min}} \quad (2.60)$$

The Mohr–Coulomb condition linking the shear stress σ_{II} and the compressive stress σ_I

$$\sigma_{II} = -\sigma_I\mu + Pk_t\mu \quad (2.61)$$

where μ is the slope of the yield curve in invariant space (σ_I, σ_{II}) and k_t the tensile factor. I replace σ_{II} by its definition as function of σ_{ij} , and insert the constitutive equations in stress invariant space (Equation 2.50)

$$\sigma_{II} = \frac{1}{2}\sqrt{(\sigma_{11} - \sigma_{22})^2 + 4\sigma_{12}^2} = 2\eta\frac{1}{2}\sqrt{(\dot{\epsilon}_{11} - \dot{\epsilon}_{22})^2 + 4\dot{\epsilon}_{12}^2} \quad (2.62)$$

so

$$\sigma_{II} = 2\eta\dot{\epsilon}_{II} = -\sigma_I\mu + Pk_t\mu \quad (2.63)$$

From which I can write

$$\eta = \frac{-\sigma_I\mu + Pk_t\mu}{2\dot{\epsilon}_{II}} \quad (2.64)$$

where σ_I is given by Equation 2.49 as

$$\sigma_I = \zeta\dot{\epsilon}_{kk} - \frac{P(1 - k_t)}{2}. \quad (2.65)$$

Finally, I add a the viscous regularization $\dot{\epsilon}_{II, min}$

$$\eta = \frac{\mu \left[\frac{P(1-k_t)}{2} - \zeta\dot{\epsilon}_{kk} + Pk_t \right]}{2 \max\{\dot{\epsilon}_{II}, \dot{\epsilon}_{II, min}\}} \quad (2.66)$$

To have a replacement pressure, as explained in Section 2.2.1.5, I define

$$P_{repl} = \frac{2|\dot{\epsilon}_{kk}|\zeta}{(1 + k_t)} \quad (2.67)$$

2.2.3.2 Viscous-Plastic behavior

The transition between plastic and viscous deformations with this yield curve is not trivial because it is composed of 4 different behaviours. the 4 different behaviours are described below (for the case with replacement pressure) and shown with their respective number on Figure 2.6:

1. For large strain rates in both divergence or convergence and shear, that is, in plastic states, all the stress states accumulate at the points $(\sigma_I = -P, \sigma_{II} = \mu(P + k_t))$ and $(\sigma_I = k_t P = T, \sigma_{II} = 0)$, for positive $\dot{\epsilon}_I$ and negative $\dot{\epsilon}_{II}$ respectively. For these two stress state, there is a multitude of flow rule direction.
2. For strain rates that are small in divergence and large in shear, only ζ reaches a maximum value. Then the stress moves toward the tip of the yield curve, on the linear limb of slope μ , toward the point $(\sigma_I = Pk_t/2, \sigma_{II} = 0)$. In this state, ice deforms plastically in shear, and viscously in divergence. The flow rule is non-normal and oriented only in shear.
3. For strain rates that are large in divergence and small in shear, only η reaches a maximum value. Then the stress moves toward the σ_I axis, toward the point $(\sigma_I = -P, \sigma_{II} = 0)$. In this state, ice deforms plastically in divergence, and viscously in shear. The flow rule is normal and oriented only in convergence.
4. For strain rates that are small in divergence and shear, both η and ζ reach a maximum value. The stress states move in both direction inside the yield curve. For small strain rates, the stress tend to get close to $(\sigma_I = 0, \sigma_{II} = 0)$. The deformation is viscous, the flow rule is set only for deformation field

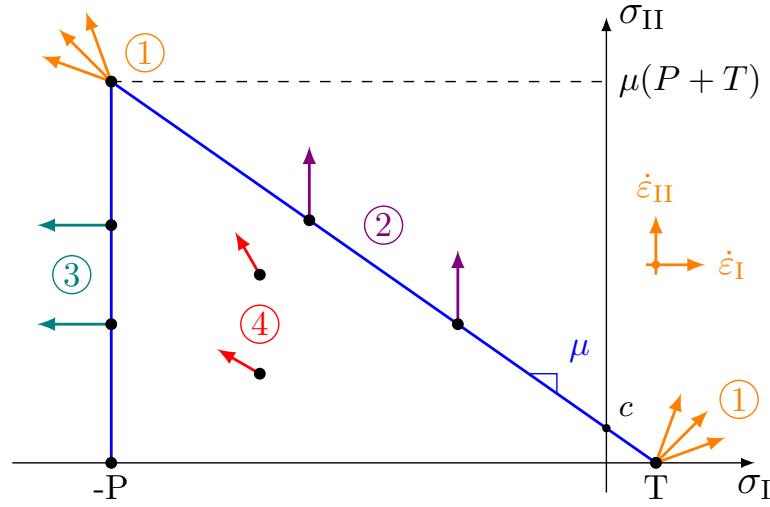


Figure 2.6: Mohr-Coulomb yield curve inspired by Ip (1993) with the illustration of 4 yield curve behaviors: 1 is purely plastic behavior, 2 is plastic in shear and viscous in divergence, 3 is plastic in divergence and viscous in shear, and 4 is purely viscous.

2.2.4 Mohr–Coulomb yield curve with elliptical plastic potential

The Mohr–Coulomb rheology presented in Section 2.2.3 has the disadvantage that only pure shear deformation is possible along the linear Mohr–Coulomb limbs. In order to have a yield curve with a defined flow rule all along the Mohr–Coulomb limbs, I use the flow rule of the elliptical yield curve and apply it to the limbs. Note that this yield curve is not build by using the yield curve and the plastic potential, but by setting a different η to have a Mohr–Coulomb shaped yield curve and ζ the same as with the elliptical yield curve with normal flow rule.

To get this yield curve, I use ζ from the elliptical yield curve formulation, Equation 2.43

$$\zeta_{\text{MCE}} = \frac{P(1 + k_t)}{2\Delta},$$

with Δ as in Equation 2.42

$$\Delta = \sqrt{(\dot{\epsilon}_{11} + \dot{\epsilon}_{22})^2 + e^{-2} [(\dot{\epsilon}_{11} + \dot{\epsilon}_{22})^2 + 4\dot{\epsilon}_{12}^2]}.$$

For η , I use the Mohr–Coulomb formulation, Equation 2.66

$$\eta_{\text{MCE}} = \frac{\mu \left[\frac{P(1-k_t)}{2} - \zeta\Delta + Pk_t \right]}{2\dot{\epsilon}_{\text{II}}}$$

Note that η is now uncoupled from ζ when it comes to viscous-plastic transition. For small deformation, if ζ reached its maximum ζ_{max} , η does not reach a maximum. To ensure that the state is viscous I define $\eta_{\text{max,MCE}}$ as a function of ζ_{max} , η , and ζ

$$\eta_{\text{max,MCE}} = \min \left\{ \eta \cdot \frac{\zeta_{\text{max}}}{\zeta}, \eta_{\text{max}} \right\} \quad (2.68)$$

And then I take the minima

$$\eta = \min\{\eta_{\text{MCE}}, \eta_{\text{max,MCE}}\} \quad (2.69)$$

$$\zeta = \min\{\zeta_{\text{MCE}}, \zeta_{\text{max}}\}. \quad (2.70)$$

In this way, I have plastic deformation along the Mohr–Coulomb slopes, viscous deformation inside the yield curve and half-plastic deformations for high compressive stress, as shown on Figure 2.7. This rheology has a non-normal flow rule for linear limbs, except on one point, where the flow rule is perpendicular to the yield curve.

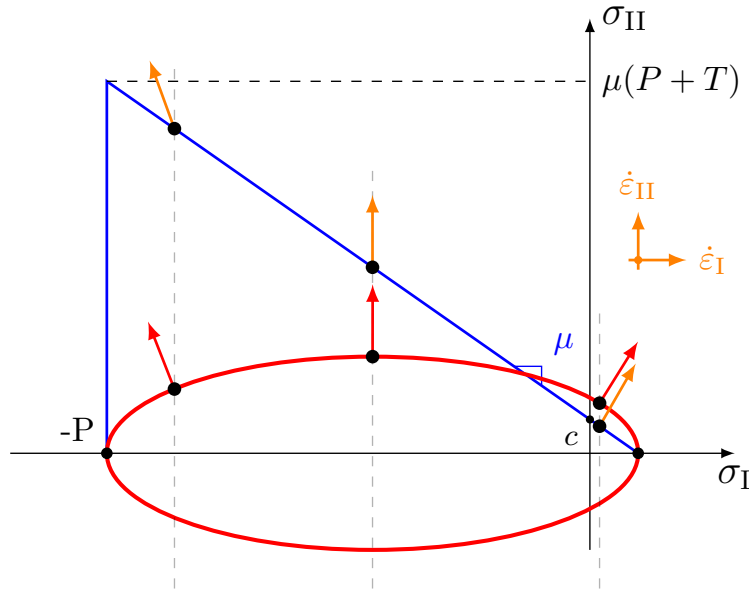


Figure 2.7: Mohr–Coulomb yield curve with elliptical plastic potential. This yield curve is similar to the modified Coulombic yield curve, but extended to be a full Mohr–Coulomb shape. The flow rule is non-normal almost everywhere along the linear limbs, except on one point. The red arrows are the normal to the plastic potential and define the flow rule, shown in orange.

2.2.5 Truncated ellipse - Coulombic yield curve

Hibler and Schulson (2000) proposed a Coulombic yield curve which is a modification of the elliptical yield curve. It includes Mohr–Coulomb linear limbs for small compressive stress. The elliptical yield curve is truncated by Mohr–Coulomb limbs with a slope μ

$$\eta = \min \left\{ \eta_{\text{ell}}, \frac{1}{2\dot{\epsilon}_{\text{II}}} \left[\mu \left(\frac{P(1 - k_t)}{2} - \zeta \dot{\epsilon}_{kk} \right) + c \right] \right\}, \quad (2.71)$$

where μ is the slope of the Mohr–Coulomb limbs (Figure 1), and c is the cohesion, that is, the value of shear strength σ_{II} for $\sigma_{\text{I}} = 0$, defined relative to the tensile strength by $c = \mu T = \mu k_t P$. On the Mohr–Coulomb limbs, the flow rule is not normal anymore, but has the direction of the corresponding point of the ellipse with the same value of σ_{I} . The yield curve and the different flow rule behaviors are shown on Fig. 2.8.

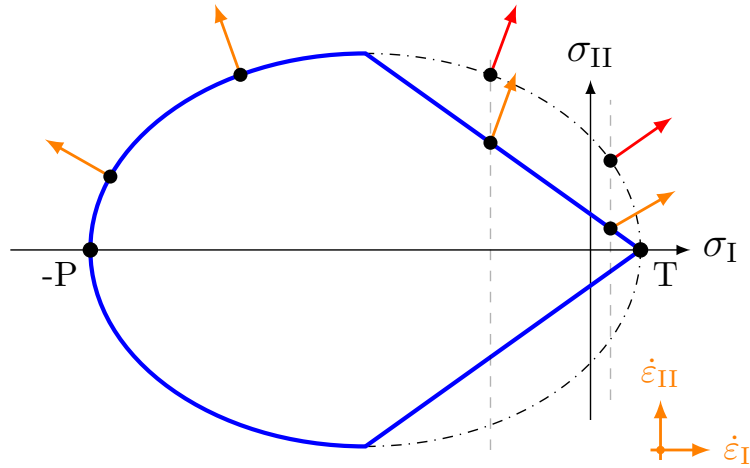


Figure 2.8: Coulombic yield curve. The orange arrows denote the flow rule and show that it is non-normal along the straight Mohr–Coulomb limbs.

Note that this yield curve is similar to the Mohr–Coulomb yield curve with elliptical plastic potential (Section 2.2.4), except for the capping with an elliptical yield curve with normal flow rule for the high-compressive stress.

2.2.6 Teardrop yield curve with normal flow rule

2.2.6.1 Formulation from Zhang and Rothrock (2005)

Zhang and Rothrock (2005) developed the constitutive equations of the teardrop yield curve with an *associated* flow rule. I repeat below the computation of the viscous coefficients. For the sake of uniformity with the other rheologies, I use k_t as the tensile factor (König Beatty and Holland, 2010) instead of a used in Zhang and Rothrock (2005). The equation of the yield curve can be written as

$$\frac{\sigma_{\text{II}}}{P} = - \left(\frac{\sigma_{\text{I}}}{P} - k_t \right) \left(\frac{\sigma_{\text{I}}}{P} + 1 \right)^{\frac{1}{2}}. \quad (2.72)$$

This equation can be simplified using

$$x = \frac{\sigma_{\text{I}}}{P}, \quad u = x - k_t, \quad y = \frac{\sigma_{\text{II}}}{P}, \quad (2.73)$$

and written as

$$F = y^2 - (1 + k_t)u^2 - u^3 = 0. \quad (2.74)$$

Then, using the associated flow rule conditions

$$\dot{\epsilon}_{\text{I}} = \lambda \frac{\partial F}{\partial u}, \quad \dot{\epsilon}_{\text{II}} = \lambda \frac{\partial F}{\partial y}, \quad (2.75)$$

The system defined by Equations (2.74) can be solved and gives

$$u = \frac{-[6(1 + k_t) - 2h^2] + 2h\sqrt{h^2 + 3(1 + k_t)}}{9} \quad (2.76)$$

for $h = \frac{\dot{\epsilon}_I}{\dot{\epsilon}_{II}} \leq 1$. To avoid confusion with the tensile strength, I replace k used in Zhang and Rothrock (2005) by h . For $h > 1$, $x = k_t$. Using $x = u + k_t$ and equations (2.49) and (2.50), the viscosities ζ and η are:

$$\zeta = \frac{\sigma_I + P/2}{2\dot{\epsilon}_I} = \frac{x + 1/2}{2\dot{\epsilon}_I} P \quad (2.77)$$

$$\eta = \frac{\sigma_{II}}{2\dot{\epsilon}_{II}} = \frac{y}{2\dot{\epsilon}_{II}} = \frac{-(x - k_t)(1 + x)^{\frac{1}{2}}}{2\dot{\epsilon}_{II}} P. \quad (2.78)$$

The equations describe the teardrop yield curve with a normal flow rule, as shown on Figure 2.9. In the case of small deformation, the viscous coefficients η and ζ become large. To avoid this, ζ is capped with a maximum, ζ_{max} . In contrast to the elliptical yield curve, η is not a function of ζ , so η is capped as well by a maximum value η_{max} (J. Zhang, personal communication).

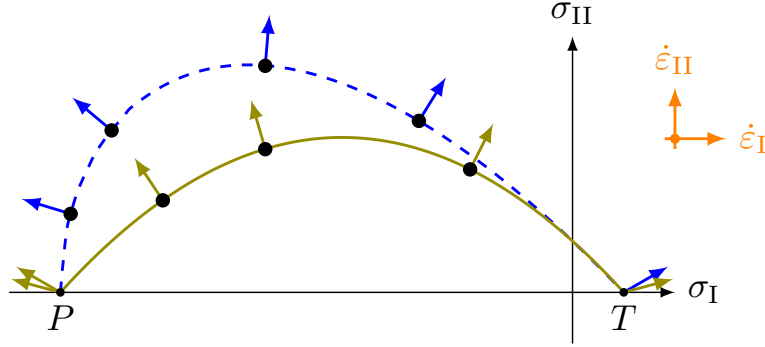


Figure 2.9: Teardrop (blue dashed line) and Parabolic Lens (green plain line) yield curve with normal flow rule in the corresponding color.

Note that the derivation of these constitutive equations is also not similar to the method described in Section 2.1.5 that was used to derive the constitutive equations of the elliptical yield curve in Section 2.2.1. Instead of computing the value of the flow rate γ by inserting the derivative of the plastic potential in the equation of the yield curve, the quotient $h = \frac{\dot{\epsilon}_I}{\dot{\epsilon}_{II}}$ is defined to compute the value of σ_I . This method is used because solving the equation with the usual method for this yield curve is, if not impossible, non-trivial and would give complicated constitutive equations.

This formulation of the constitutive equations leads to three problems, which I describe and solve in following sections.

2.2.6.2 Transition between Viscous and Plastic deformations

The viscosities ζ and η are capped independently, in contrast with the elliptical yield curve where capping ζ to the maximum value put a maximum value to η as well. However, ζ is capped and η is not capped, then the constitutive equations are in a state where divergence and convergence take place in the viscous regime and the shear deformation in the plastic regime. This behavior is not consistent, because stress states inside the yield curve are then not entirely viscous anymore.

I propose the following modification. The value of η_{max} is computed from the value of ζ before capping following

$$\eta_{max} = \eta \frac{\zeta_{max}}{\zeta}, \quad (2.79)$$

with this I ensure that all stress states inside the yield curve are viscous states, and all stress on the yield curve are plastic states.

2.2.6.3 The condition $h \leq 1$

The condition $h \leq 1$ is used to ensure that $x < a$. But the condition does not depend on the value of a , and therefore excludes a part of the yield curve when $a > 0$. In order to ensure that the yield curve is continuous between $\sigma_I/P = a$ and $\sigma_I/P = -1$, I propose to use the following condition for the value of x :

$$\text{reset } x = k_t \text{ for } x > a. \quad (2.80)$$

2.2.6.4 Negative zeta

With the formulation of Equation (2.77) above, the value of ζ can be negative if

- The denominator $2\dot{\epsilon}_I$ changes sign with h , at $h = \frac{\dot{\epsilon}_I}{\dot{\epsilon}_{II}} = 0$
- For $k = 0$, the numerator $x + 1/2$ is different from 0 (excepted for one value $k_t = 1/2$)

$$\text{For } h = 0, \quad x + 1/2 = \frac{1}{2} - \frac{2 - k_t}{3} \neq 0, \quad (2.81)$$

so the value of ζ tends to infinity and changes sign.

This problem might come from the method used to derive the constitutive equation, because the tensile parameter is not taken into account correctly when using the mathematical expression for ζ between Equation (2.76) and (2.77)

In the original work, the negative ζ are dealt with by using a minimum value of $\zeta_{min} = 0$ (J. Zhang, personal communication), but this also leads to a discontinuity in the yield curve. In order to change this, I modify the expression of ζ (Equation 2.77) and the expression of the pressure. ζ becomes

$$\zeta = \frac{x + \frac{2-k_t}{3}}{2\dot{\epsilon}_I} P, \quad (2.82)$$

and pressure

$$P_m = 2 \cdot \frac{2 - k_t}{3} \cdot P. \quad (2.83)$$

The change in the pressure formulation avoids the need to change the constitutive equations. Similarly, I define the replacement pressure to avoid stress when there is no deformation (see Section 2.2.1.5):

$$P_m = \frac{2\dot{\epsilon}_I\zeta}{x + \frac{2-k_t}{3}} \cdot 2 \cdot \frac{2 - k_t}{3} \quad (2.84)$$

2.2.6.5 Summary of the modifications

I summarize below the modified viscosities for the teardrop yield curve

$$h = \frac{\dot{\epsilon}_I}{\dot{\epsilon}_{II}}, \quad (2.85)$$

$$x = \frac{-[6(1+k_t) - 2h^2] + 2h\sqrt{h^2 + 3(1+k_t)}}{9} + a, \quad (2.86)$$

$$\text{with } x = a \text{ if } x > a, \quad (2.87)$$

$$\zeta = \frac{x + \frac{2-k_t}{3}P}{2\dot{\epsilon}_I}P, \quad (2.88)$$

$$\eta = \frac{-(x-k_t)(1+x)^{\frac{1}{2}}}{2\dot{\epsilon}_{II}}P, \quad \eta_{max} = \eta \frac{\zeta_{max}}{\zeta}, \quad (2.89)$$

$$P = 2 \cdot \frac{2-k_t}{3} \cdot P, \text{ without replacement pressure} \quad (2.90)$$

$$P = \frac{2\dot{\epsilon}_I\zeta}{x + \frac{2-k_t}{3}} \cdot 2 \cdot \frac{2-k_t}{3} \text{ with replacement pressure.} \quad (2.91)$$

The equations for σ_{ij} stay the same as for elliptical yield curve (Equation (2.46))

2.2.7 Parabolic Lens yield curve with normal flow rule

2.2.7.1 Formulation from Zhang and Rothrock (2005)

Zhang and Rothrock (2005) also derived the constitutive equations for the *parabolic lens* yield curve with a normal flow rule. It is a smooth yield curve (Figure 2.9) designed to be similar to the diamond yield curve of Coon et al. (1974). As for the teardrop yield curve, I replace a and k , used in (Zhang and Rothrock, 2005) by k_t and h . I repeat below the computation of the viscous coefficients. The equation of the yield curve can be written as

$$\frac{\sigma_{II}}{P} = - \left(\frac{\sigma_I}{P} - k_t \right) \left(\frac{\sigma_I}{P} + 1 \right). \quad (2.92)$$

I use the same method as for the teardrop yield curve and find

$$u = \frac{1}{2}(k - 1 - k_t) \quad (2.93)$$

for $k = \frac{\dot{\epsilon}_I}{\dot{\epsilon}_{II}} \leq 1$. For $k > 1$, $x = k_t$. Using $x = u + k_t$ and equations (2.49) and (2.50), the viscosities ζ and η are:

$$\zeta = \frac{\sigma_I + P/2}{2\dot{\epsilon}_I} = \frac{x + 1/2}{2\dot{\epsilon}_I}P \quad (2.94)$$

$$\eta = \frac{\sigma_{II}}{2\dot{\epsilon}_{II}} = \frac{y}{2\dot{\epsilon}_{II}} = \frac{-(x-k_t)(1+x)}{2\dot{\epsilon}_{II}}P. \quad (2.95)$$

The equations above describe the parabolic yield curve with normal flow rule. In the case of small deformation, the viscous coefficients become large. To avoid this, I cap ζ with a maximum, ζ_{max} .

2.2.7.2 Summary of the modifications

From this formulation of the parabolic lens yield curve, the same problems as for the teardrop yield curve appear, but can be solved in the same way. I summarize below the modified viscosities for the teardrop yield curve

$$h = \frac{\dot{\epsilon}_I}{\dot{\epsilon}_{II}}, \quad (2.96)$$

$$x = \frac{1}{2}(h - 1 + k_t), \quad (2.97)$$

$$\text{with } x = k_t \text{ if } x > k_t, \quad (2.98)$$

$$\text{and } x = -1 \text{ if } x < -1, \quad (2.99)$$

$$\zeta = \frac{x + (1 - k_t)}{2\dot{\epsilon}_I} P, \quad (2.100)$$

$$\eta = \frac{-(x - k_t)(1 + x)}{2\dot{\epsilon}_{II}} P, \quad (2.101)$$

$$P = (1 - k_t)P, \text{ without replacement pressure} \quad (2.102)$$

$$P = \frac{2\dot{\epsilon}_I \zeta}{x + (1 - k_t)} \cdot (1 - k_t) \text{ with replacement pressure.} \quad (2.103)$$

The equations for σ_{ij} stay the same as for elliptical yield curve (Equation (2.46))

2.2.8 Other VP rheologies

Some other VP rheologies have to be mentioned for completeness:

- **The curved diamond yield curve (Wang, 2007):** This rheology is built by observing LKFs angles and using observations and the relationship between yield curve and fracture angles (Pritchard, 2001). The yield curve is close to the diamond yield curve of Coon et al. (1974) but features a slightly bent curve to include small fracture angles. Wang and Wang (2009) used this yield curve to model LKFs in the Arctic pack ice, but the deformation fields they present appear to be dominated by features aligned with the numerical grid (their Figure 6).
- **The Mohr–Coulomb yield curve including dilatancy (Tremblay and Mysak, 1997):** This Mohr–Coulomb yield curve differs from the one described in Section 2.2.3 by allowing to change the direction of the flow rule and avoid the shear-only flow rule.
- **The EVP rheology (Hunke, 2001a):** This is not a different VP rheology, but a method to solve the VP momentum equation by introducing an elastic term. This method is faster but is known to produce smoother field of deformation without LKFs. This issue can be fixed by using adaptive methods (Kimmritz et al., 2016; Koldunov et al., 2019)

2.3 Summary

In this Chapter, I have reviewed the equations that govern the rheology in VP sea ice models. I defined the main components and characteristics of sea ice rheologies, the

yield curve, and flow rule and detailed the construction of the constitutive equations linking stress and strain rates. After this, I have reviewed most of the VP rheologies used for sea ice modeling, from the most common one to new VP rheologies. The elliptical yield curve with normal flow rule has been used now for 4 decades. Other rheologies have been used only marginally in climate simulations, however, the need sea ice rheology suitable for high resolutions appears again because of the recent increases in computer power.

Because the resolution of Arctic simulations have increased, questions arise about of the ability of VP rheologies to simulate correctly the creation of LKFs. Comparisons between simulations and observation show that there is large differences in the distribution of angles between LKFs (Hutter et al., 2019). In the following chapter, I develop a theory linking the intersection angle of Linear Kinematic Features (LKFs) in sea ice to the VP rheology, taking into account both the yield curve and the flow rule.

Chapter 3

Orientation of fracture in VP sea ice models

There is an irresistible fascination about the regions of northernmost Grant Land that is impossible for me to describe. Having no poetry in my soul, and being somewhat hardened by years of experience in that inhospitable country, words proper to give you an idea of its unique beauty do not come to mind. Imagine gorgeous bleakness, beautiful blankness.

— *A Negro explorer at the North Pole* – Matthew A. HENSON

Note: Of the next sections,

- Section 3.2 has been published as the Appendix A in *Simulating intersection angles between conjugate faults in sea ice with different VP rheologies* by Ringeisen et al. (2019) in the journal *The Cryosphere*.
- Section 3.3 is a modified version of the Appendix B1 published from Ringeisen et al. (2019), with a new section to take into account results of Chapter 5.
- Section 3.4 includes the appendix B2 and a modified version of B3 from Ringeisen et al. (2019) and expands the fracture theory to all the yield curves presented in Section 2.2.

3.1 The orientation of shear bands in granular materials

Satellite observations show that sea ice deforms along thin lines, called Linear Kinematic Features (LKFs) (Overland et al., 1998; Kwok, 2001). Hutchings et al. (2005) showed that the standard VP model (Hibler, 1979) and the Modified Coulombic yield curve (Hibler and Schulson, 2000) allows the creation of these shear bands. These LKFs, or shear bands, are present in high-resolution sea ice models (Losch et al., 2014; Hutter and Losch, 2020).

Shear banding is a common feature of a granular medium, like sand or clay. Charles-Augustin de Coulomb was the first to study it (Coulomb, 1773). In his seminal work, he argued that the angle θ between the shear band and the major

compressive stress axis is given by

$$\theta_C = \frac{\pi}{4} - \frac{\phi}{2} \quad (3.1)$$

where ϕ is called the internal angle of friction (see Figure 3.1a). This hypothesis created what is now called the Mohr-Coulomb criterion (Mohr, 1882). This theory has since been challenged by some experimental results. Some show that the angle of dilatancy δ (see Figure 3.1b) of the material plays a major role in setting the orientation of the shear bands (Roscoe, 1970). The angle θ then becomes

$$\theta_R = \frac{\pi}{4} - \frac{\delta}{2} \quad (3.2)$$

with δ defined as shown on Figure 3.1. Other experiments showed that both internal angle of friction and dilatancy angle play an equal role (Arthur et al., 1977; Vardoulakis, 1980). They defined θ as

$$\theta_A = \frac{1}{2} (\theta_C + \theta_R) = \frac{\pi}{4} - \frac{1}{4} (\delta + \phi) \quad (3.3)$$

More recent experiments showed that both mechanisms are valid, and their role varies with the grain size of the granular material (Vermeer, 1990). If the dilatancy angle and the internal angle of friction are equal, then the flow rule is an associative flow rule or a normal flow rule, as described in Chapter 2.

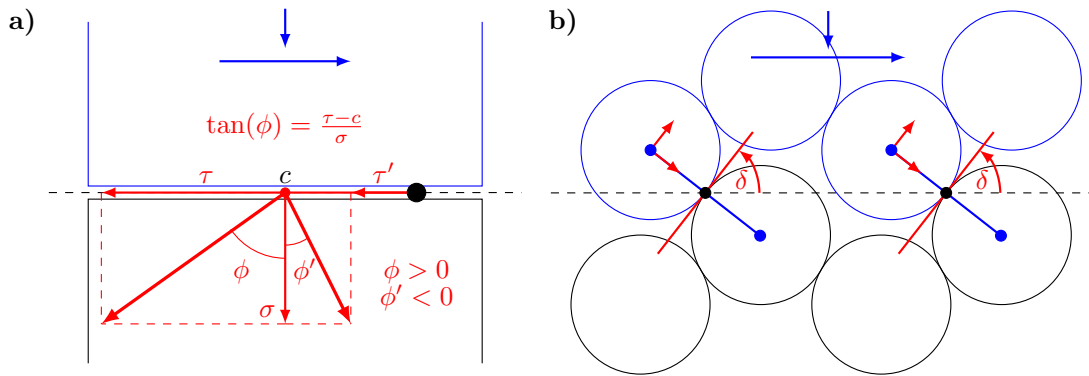


Figure 3.1: Illustration of the internal angle of friction and the angle of dilatancy. In both panels, the blue part (top) is moving (blue arrows) respect to the black part (bottom). The friction is considered at the black dot. **a)** The angle of friction is define by the relative amounts of the shear minus to the cohesion strength ($\tau - c$) and normal (σ) stress at the fracture line. The angle of friction is negative if the shear stress is smaller than the cohesion strength (τ', ϕ'), and vice versa (τ, ϕ). **b)** The dilatancy angle δ is given by the contact points between grains in a granular material. The fracture line is shown here by the black dashed line. The blue arrows show the forces on the macroscopic place, while red arrows show the forces on the microscopic plane defined by the grain contacts. Note that δ can also be negative when the granular medium is closing. Modified from Figure 6 of Tremblay and Mysak (1997)

The remaining parts of this chapter aims at defining the link between the fracture angles and the sea ice VP rheologies. I first derive the classical Mohr's circle and

internal angle of friction theory from Coulomb (1773) — Equation (3.1). I then apply this relation to sea ice VP rheologies with normal flow rule, before considering the case of a non-normal flow rule using the arguments of Roscoe (1970). Finally, I compute the theoretical fracture angle for each rheology in Chapter 2 for the case of an uni-axial compression experiment.

3.2 Mohr–Coulomb theory of the internal angle of friction

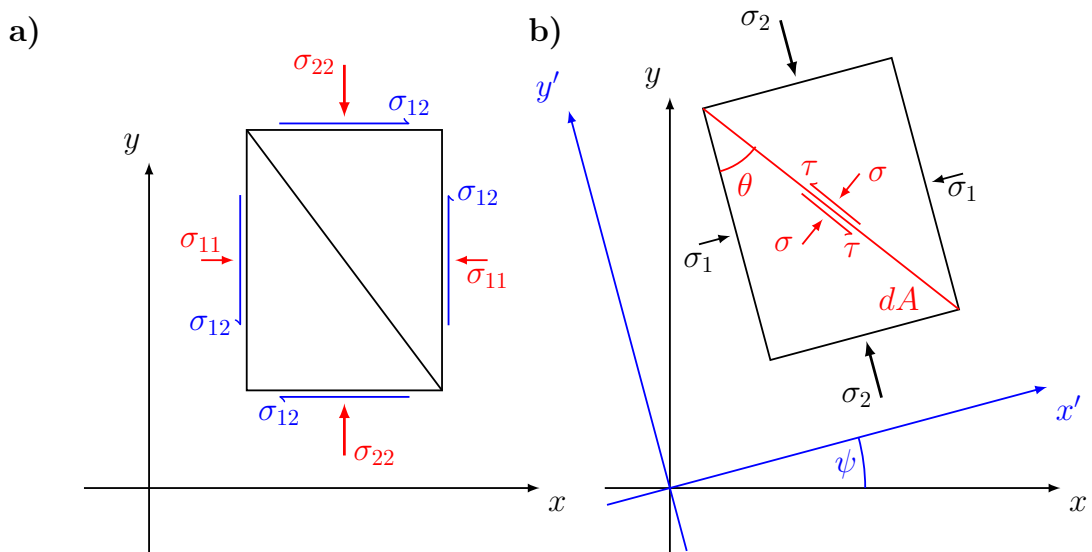


Figure 3.2: Stress state in physical stress space (a) and in an arbitrary coordinate system oriented at an angle θ with the principal stress axes (b) on an arbitrary unit of element. The principal stresses are the eigenvalues of the stress tensor in an arbitrary coordinate system, and the angle ψ is derived from the rotation matrix composed of the two eigenvectors. Note that in uni-axial compression, there is no shear stress ($\sigma_{12} = 0$) so principal axes and physical axes are aligned ($\psi = 0$).

Below, I derive a relationship between the fracture angle and the internal angle of friction for a Mohr–Coulomb yield criterion (Coulomb, 1773; Mohr, 1882; Mohr, 1900). I consider an arbitrary piece of a 2D medium (Figure 3.2a) that is subject to stress in physical stress space σ_{ij} ($i = 1, 2$). I can consider the principal stress (σ_1, σ_2) applied on the medium (Figure 3.2b) as described in Section 2.1.3. From the force balance, the normal stress σ and the shear stress τ on a plane at an angle θ from the principal stress axis can be written as (see Figure 3.2b and Popov, 1976)

$$\sigma dA = \sigma_2 \sin(\theta) \sin(\theta) dA + \sigma_1 \cos(\theta) \cos(\theta) dA, \quad (3.4)$$

$$\tau dA = -\sigma_2 \cos(\theta) \sin(\theta) dA + \sigma_1 \cos(\theta) \sin(\theta) dA, \quad (3.5)$$

where dA is the area of the friction plane on which the stress are applied (in 2D it is just a line). The second trigonometric term comes from the fact that this surface is tilted compared to the direction of stress σ_1 and σ_2 . Using the angle sum and difference identities of trigonometry, the stress σ and τ in terms of the principal

stress σ_1 and σ_2 as are written as

$$\sigma = \frac{1}{2}(\sigma_1 + \sigma_2) + \frac{1}{2}(\sigma_1 - \sigma_2) \cos(2\theta), \quad (3.6)$$

$$\tau = \frac{1}{2}(\sigma_1 - \sigma_2) \sin(2\theta). \quad (3.7)$$

In terms of the stress invariants σ_I and σ_{II} , this gives

$$\sigma = \sigma_I + \sigma_{II} \cos(2\theta), \quad (3.8)$$

$$\tau = \sigma_{II} \sin(2\theta). \quad (3.9)$$

The Mohr–Coulomb failure criterion can be written in the fracture plane stress space (σ, τ) (see Figure 3.3) as

$$\tau = -\tan(\phi) \sigma + c, \quad (3.10)$$

where ϕ is the internal angle of friction, and c the cohesion when no stresses are applied (Verruijt, 2018). Substituting (3.8) and (3.9) in (3.10), I get

$$\sigma_{II} \sin(2\theta) = -\tan(\phi) \sigma_I - \tan(\phi) \sigma_{II} \cos(2\theta) + c, \quad (3.11)$$

and after multiplying both sides by $\cos(\phi)$

$$\sigma_{II} [\sin(2\theta) \cos(\phi) + \cos(2\theta) \sin(\phi)] = -\sigma_I \sin(\phi) + c \cos(\phi). \quad (3.12)$$

By geometrical construction (see Figure 3.3), the MC criterion is satisfied when (see also Verruijt, 2018, Section 20.4)

$$\sin(\phi) = \frac{\sigma_{II}}{\sigma_I + \frac{c}{\tan(\phi)}}, \quad (3.13)$$

which can be simplified as

$$\sigma_{II} = -\sigma_I \sin(\phi) + c \cos(\phi), \quad (3.14)$$

so that Equation. (3.12) becomes

$$\sin(2\theta) \cos(\phi) + \cos(2\theta) \sin(\phi) = \sin(2\theta + \phi) = 1, \quad (3.15)$$

from which the classical result of material deformation physics emerges:

$$2\theta + \phi = \frac{\pi}{2} \Rightarrow \theta = \frac{\pi}{4} - \frac{\phi}{2} \quad (3.16)$$

3.3 Linking fracture angle and sea ice VP rheology

3.3.1 Linking fracture angle to the yield curve

In the following, I use the Mohr's circle and Coulomb's internal angle of friction to link sea ice rheology with a normal flow rule to the fracture angle θ . In the context of sea ice modeling, a yield curve is defined in the local stress (σ_{ij}) , principal stress

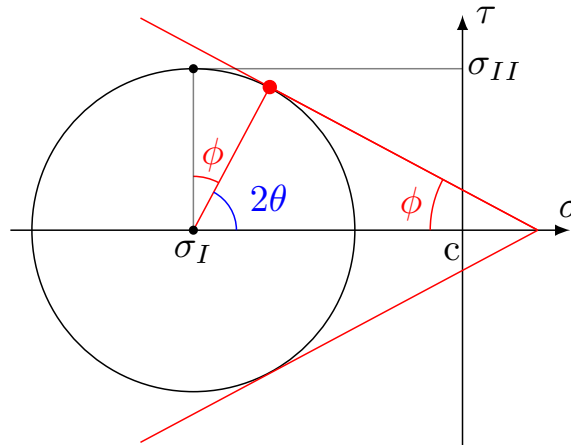


Figure 3.3: Mohr's circle of stress (Mohr, 1900) (black) with the Mohr–Coulomb yield criterion (red) (Mohr, 1882) of the angle of internal friction ϕ (red) and cohesion c in (σ, τ) space. From Equation (3.16), the deformation is created with an angle θ that can be represented in Mohr's circle (blue).

$(\sigma_{1,2})$, or stress invariant $(\sigma_{I,II})$ spaces. The yield curve in stress invariant space $(\sigma_{I,II})$ gives, for each stress state on it, the center and radius of the Mohr's circle of stress for which the ice will break. Mohr's circle of stress defines all the equivalent stress states (σ, τ) for any angle $\theta \in [0, \pi]$ in the reference coordinate system of the element (see Figure 3.2). The question is to determine for which angles θ the fracture will be created. By drawing all the Mohr's circle of the yield curve, it is possible to observe that a new yield curve envelope emerges. In this sense, I can define the yield curve in the fracture plane (σ, τ) space as the envelope of all Mohr's circles of the yield curve defined in stress invariant coordinates (see Figure 3.7 for an illustration with the elliptical yield curve). In the following, I refer to this envelope of all Mohr's circles as the reconstructed yield curve. With this principle and with the geometrical construction shown in Figure 3.4, I can express the internal angle of friction ϕ as a function of the tangent to the yield curve with the expression

$$\sin(\phi) = \tan(\gamma) = -\frac{\partial \sigma_{II,F}}{\partial \sigma_I}, \quad (3.17)$$

where $\sigma_{II,F}$ is the yield curve F expressed as σ_{II} as a function of σ_I . The fracture angle for stress states on the yield curve envelope can be expressed by inserting Equation (3.17) in Equation (3.16):

$$\theta_n(\sigma_I) = \frac{\pi}{4} - \frac{1}{2} \arcsin \left(-\frac{\partial \sigma_{II,F}}{\partial \sigma_I}(\sigma_I) \right) = \frac{1}{2} \arccos \left(-\frac{\partial \sigma_{II,F}}{\partial \sigma_I}(\sigma_I) \right). \quad (3.18)$$

This is the same relation presented in Pritchard (1988) and used previously in Wang et al. (2006), but is obtained within the (σ, τ) stress space.

The theoretical fracture angle defined here agrees with the Coulomb angle, Equation (3.1), the Roscoe angle, equation (3.2), and the Arthur angle, Equation (3.3) because the flow rule is normal to the yield curve, i.e., the internal angle of friction and the angle of dilatancy are the equal.

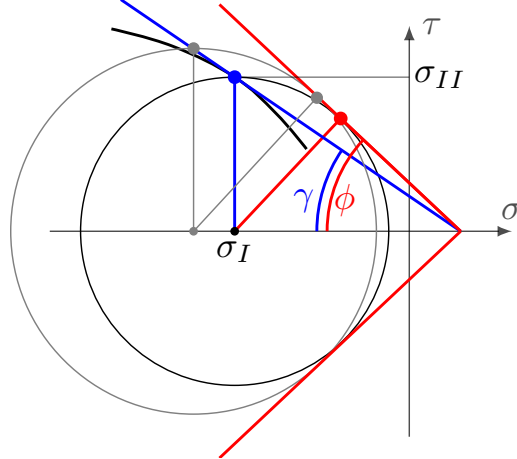


Figure 3.4: Mohr's circle of stress with an arbitrary yield curve (black line) in the fracture plane reference. The blue line is the tangent to the yield curve. The red line is the tangent to the Mohr's circle through the same intersection point $\tan(\gamma) = \mu$ is the tangent to the yield curve, and ϕ is the internal angle of friction as described in Section 3.2. Note that $\sin(\phi) = \tan(\gamma) = \mu$ (for $|\mu| \leq 1$). For a different Mohr's circle (grey), the blue and red tangents meet in the same point on the σ axis.

3.3.2 Linking the fracture angle to the flow rule

The theory in the previous Section 3.3.1 links the fracture angle to the yield curve. It accurately predicts the fracture angles obtained with the standard elliptical yield curve with normal flow rule as will be shown in Chapter 4, Figure 4.10. Although the theory gives accurate results in prediction the fracture angles, the influence of using a non-normal flow rule is still unclear in VP sea ice models.

Following Roscoe (1970), who based their theory on observations of granular media like sand, I now consider the plastic potential to be the main parameter in the rheology for determining the fracture angle. To compute the fracture angle for a given point on the yield curve, I consider the slope of the plastic potential function (G in Figure 3.5), and not the slope of the yield curve (function F in Figure 3.5).

Figure 3.5 shows the case of an arbitrary yield curve with an arbitrary plastic potential. Using the same geometrical construction as in the previous Section 3.3.1, the angle δ is defined as

$$\sin(\delta) = \tan(\gamma_G) = -\frac{\partial \sigma_{II,G}}{\partial \sigma_I}(\sigma_I^p), \quad (3.19)$$

where $\sigma_{II,G}(\sigma_I)$ is the plastic potential G expressed as σ_{II} as a function of σ_I . This relationship agrees with the definition of Roscoe (1970) $\sin(\delta) = \frac{\dot{\epsilon}_I}{\dot{\epsilon}_{II}}$, because the ratio of $\dot{\epsilon}_I$ to $\dot{\epsilon}_{II}$ is equal to the slope of the plastic potential $-\frac{\partial \sigma_{II,G}}{\partial \sigma_I}$, as the flow rule is perpendicular to the plastic potential.

Using this definition, I rewrite Equation 3.18 with the definition of the Roscoe angle (Equation 3.2), the theoretical fracture angle becomes

$$\theta_{nn}(\sigma_I) = \frac{\pi}{4} - \frac{1}{2} \arcsin \left(-\frac{\partial \sigma_{II,G}}{\partial \sigma_I}(\sigma_I^p) \right) = \frac{1}{2} \arccos \left(-\frac{\partial \sigma_{II,G}}{\partial \sigma_I}(\sigma_I^p) \right). \quad (3.20)$$

Note that using a non-normal flow rule contradicts the Drucker's postulate for plasticity (Kelly, 2020). As described in Section 2.1.5.5 using a non-normal flow

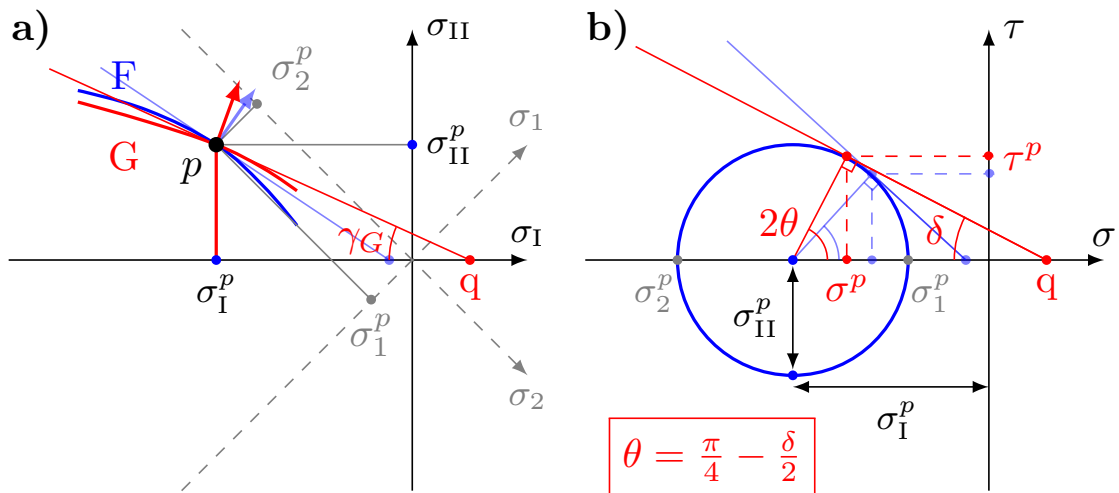


Figure 3.5: Link between fracture angle and yield curve: **a)** Arbitrary yield curve F (blue) and plastic potential G (red) in stress invariants space. The plastic potential and yield curve intersect at a stress state p for illustration purposes only. The red arrow is perpendicular to G , but non-normal to the yield curve F . The tangent to the plastic potential G at point p has a slope $\mu_G = \tan(\gamma_G)$ and intersects the σ_I -axis at point q (thin red line). For reference, the normal and tangent to the yield curve F are shown as a thin blue arrow and line. Gray dashed lines show the principal stress axes. **b)** Mohr's circle for the fracture state p in **a)** in the fracture plane of reference (σ, τ) of center σ_I^p and radius σ_{II}^p . The thin red line is the tangent to the Mohr's circle that passes through the point q on the σ axis. By this geometrical construction, $\sin(\delta) = \tan(\gamma_G) = \mu_G$ (for $|\mu_G| \leq 1$). δ is called the dilatancy angle. Again for comparison, the transparent blue lines show the corresponding construction for a normal flow rule from panel **a)**.

rule may lead to negative dissipation of energy for some deformation events. I can express this instability by the fact that Mohr's circle is valid locally but not globally: A fracture point on the Mohr's circle (red dot in Figure 3.5b) for a stress point σ_I^p could be inside the Mohr's circle of stress of another stress state σ_I . Because of this, reconstructing a yield curve as on Figure 3.7 for the elliptical yield curve with a normal-flow rule. Rheologies with a non-normal flow rule are expected to be more challenging to solve than their counterparts with a normal flow rule because the ratio of shear stress to normal stress is different than the ratio of shear to divergence.

3.4 Fracture angles for uniaxial compression

In this section, I first define uniaxial compression in terms of different stress spaces: physical, principal and invariant. In a second time, I calculate the fracture angle for uniaxial compression for each rheology for the Coulomb angle and Roscoe angle.

3.4.1 Uniaxial compression

To study the creation of fracture with VP sea ice rheologies in the next chapters, I use an idealized experiment with uni-axial compression. I compute the fracture angles for the elliptical yield curve with non-normal flow rule in uniaxial compression

from the y axis. This can be visualized on Figure 3.2. With $\sigma_{11} = \sigma_{12} = 0$, $\sigma_{22} < 0$, the principal stresses and stress invariants can be written as:

$$\sigma_1 = \frac{1}{2} \left(\sigma_{11} + \sigma_{22} + \sqrt{(\sigma_{11} - \sigma_{22})^2 + 4\sigma_{12}^2} \right) = 0 \quad (3.21)$$

$$\sigma_2 = \frac{1}{2} \left(\sigma_{11} + \sigma_{22} - \sqrt{(\sigma_{11} - \sigma_{22})^2 + 4\sigma_{12}^2} \right) = \sigma_{22}. \quad (3.22)$$

$$\sigma_I = \frac{\sigma_1 + \sigma_2}{2} = \frac{\sigma_{22}}{2} \quad (3.23)$$

$$\sigma_{II} = \frac{\sigma_1 - \sigma_2}{2} = -\frac{\sigma_{22}}{2} = -\sigma_I. \quad (3.24)$$

From Equ. 3.24, the maximum shear stress $\sigma_{II,F}^p$ on the fracture plane in uniaxial compression can be expressed as:

$$\sigma_{II,F}(\sigma_I^p) = -\sigma_I. \quad (3.25)$$

Figure 3.6 illustrates the uni-axial behavior of the stress in a uni-axial compression for a normal flow rule and a non-normal flow rule. Figure 3.6a shows the case of a elliptical yield curve with normal flow rule: Changing the shape of the yield curve changes the fracture state and the flow rule. If sea ice is confined on the side and cannot expand, then $\sigma_{11} \neq 0$, which leads to $\sigma_I \neq 0$, and therefore, the stress increases from higher compressive stress, as shown with the blue dashed line. Figure 3.6b shows case of the elliptical yield curve with a non-normal flow rule. The direction of the flow rule changes with the plastic potential for the same stress state p or p' .

Note that for rheologies with a narrow tip in low compressive stress (e.g., Mohr-Coulomb yield curves, Teardrop and Parabolic Lens yield curves), adding tensile strength is necessary for the uniaxial compression experiments. If the tensile strength $T = 0$, stress states reach the yield curve for a stress $\sigma_I = \sigma_{II} = 0$. The experiment is not stable because uniaxial deformation take place with zero stress. The elliptical yield curves have the advantages to have large shear strength for very small compressive stresses, so the ice does not deform plastically. For the other rheologies, adding tensile strength increases stability. In addition, observation showed that sea ice models should include tensile strength (Coon et al., 2007; Weiss and Schulson, 2009).

3.4.2 Elliptical yield curve with a normal flow rule

From the relationship between yield curve and fracture angle in Section 3.3.1, I compute the theoretical fracture angles for the elliptical yield curve with normal flow rule in uni-axial compression. As shown in Figure 3.6, in a uni-directional compressive setup the slope of a tangent to the yield curve changes with the ellipse ratio. The convexity of the ellipse implies that the ratio $\frac{\tau}{\sigma} = \tan(\phi)$ of shear strength τ to compressive strength σ becomes smaller with smaller e . If I compute the slope of the tangent to the elliptical yield curve at the intersection point between the yield curve and the σ_2 axis, I get

$$\left. \frac{\partial \sigma_{II}}{\partial \sigma_I} \right|_{\sigma_{II} = -\sigma_I} = -\frac{1}{2} \left(1 - \frac{1}{e^2} \right). \quad (3.26)$$

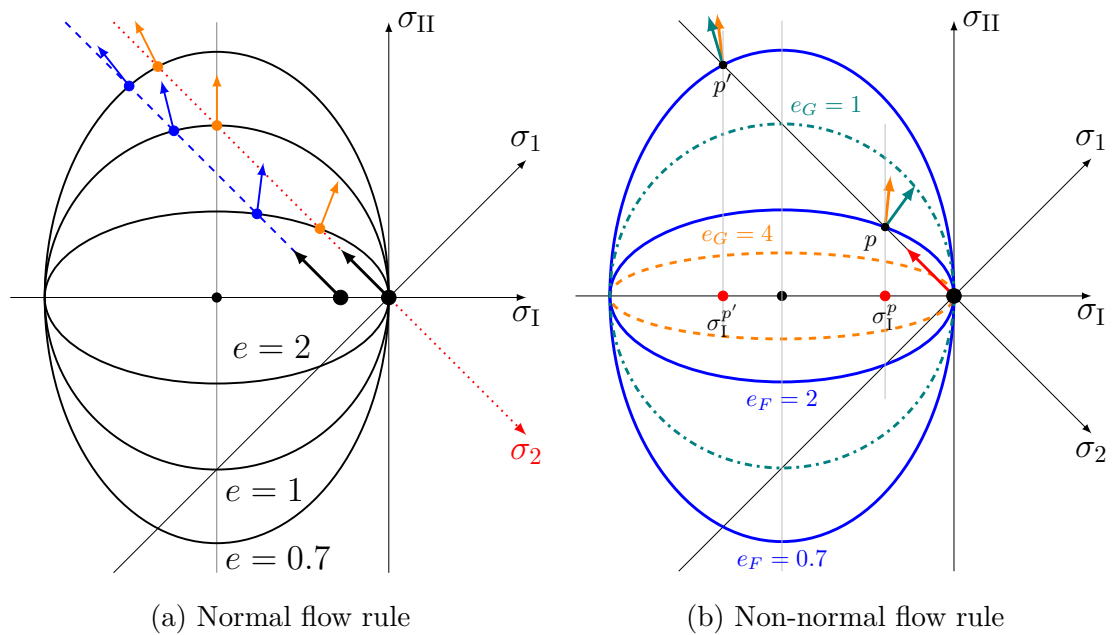


Figure 3.6: Schematics of stress states and failure in stress invariant space. Panel (a): Black arrows show how stress move from zero at the beginning of loading towards the yield curve until failure. The failure stress state (orange points) and the direction of deformation (orange arrows) changes with the ellipse ratio from divergences ($e = 2$) to pure shear ($e = 1$) and convergence ($e = 0.7$). The blue points and arrows show the case when the ice floe is confined and the loading will lead to extra stress in the direction of σ_I . Panel (b): Trajectory of maximum normal stress (red arrow) in a uniaxial compression experiment in a material with an elliptical yield curve (blue) and two plastic potentials (dashed orange and dash-dotted teal). The arrows show the flow rule which is normal to each plastic potential for the same stress state in uniaxial compression. The yield curves in blue have ellipse ratios $e_F = 2$ and $e_F = 0.7$, the two plastic potentials have an ellipse ratio $e_G = 1$ (dashed orange), and $e_G = 4$ (dot-dashed teal). Both create a different flow rule shown a by the arrow in the corresponding color. Having $e_G < e_F$ favors divergence to shear, while having $e_G > e_F$ does the inverse. A similar figure in principal stress space is presented on Figure 4.4

Inserting this relationship into Equation (3.18) gives the angle of fracture for the uni-axial compressive experiment with an ellipse ratio e :

$$\theta_{e,n}(e) = \frac{1}{2} \arccos \left[\frac{1}{2} \left(1 - \frac{1}{e^2} \right) \right]. \quad (3.27)$$

A yield curve in (σ_I, σ_{II}) space with a tangent slope above unity does not have a Mohr's circle that can be tangent to the yield curve in (σ, τ) space (orange circle on in Figure 3.7). It implies that it is not possible to derive an angle of fracture for these stresses states, which is exactly the case for the elliptical yield curve for low and high compressive stress. It is still unclear what happens in the VP model for stress states on the yield curve that have a tangent with a slope higher than unity (see also Pritchard, 1988). Note also that for some (σ_I, σ_{II}) states, the ice will fail in tension, as the reconstructed yield curve with a few points in the first and fourth quadrant.

The shear and bulk viscosities are symmetrical about the center of the ellipse. It implies that they are equal for divergence and convergence. This behavior is not physical since, for shear deformations where ice floes continue to interact with one another (termed the quasi-static flow regime, Babić et al. (1990)), divergent flow counterintuitively should have more ice–ice interactions and higher viscosities than convergent flow — because the divergent flow is the result of a higher number of contact normals opposing the shear. When the divergence is significant, and floes no longer interact, the shear and bulk viscosities are still symmetrical about the center of the ellipse. While this is nonphysical, it does lead to a better numerical stability because the extra viscosity or dissipation of energy regularizes the problem.

Note that a yield curve with a tangent that has a slope smaller than 1 (in absolute value) in the first and fourth quadrant (positive first principal stress) is unphysical because it would lead to a diamond-shaped pair of ice fracture even in a uni-axial tensile test, which is inconsistent with laboratory experiments that show fracture lines perpendicular to the axis of stress (Cox and Richter-Menge, 1985; Menge and Jones, 1993). I conclude that adding tensile strength to the elliptical yield curve may not be physical.

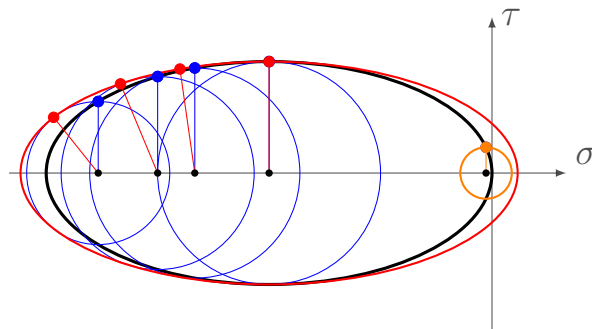


Figure 3.7: Illustration of the Mohr's circle applied to the elliptical yield curve (black ellipse) in σ, τ space, some examples of Mohr's circles (blue), and the reconstructed yield curve (red) in the fracture plane space. The orange Mohr's circle illustrates the case in which no fracture lines exists, for $|\mu| > 1$.

3.4.3 Elliptical yield curve with non-normal flow rule

If I only consider the theory of the internal angle of friction (Coulomb, 1773), then the angle of fracture would not change with a different orientation of the flow rule, the angle is not influence by the flow rule, only the slope of the yield curve. The fracture angles would stay the same as for the elliptical yield curve with normal flow rule. In the remainder of this section, I consider the case where the flow rule direction, or dilatancy angle, is the main factor for determining the fracture angle (Roscoe, 1970).

I use the Equation (3.20) instead of the Equation 3.18 to take into account the effect of the non-normal flow rule. I use the same method as in Section 3.4.2 to determine the fracture angle in pure compression. First, I compute the point where the σ_2 axis intercepts the yield curve F , i.e. where $\sigma_{II} = -\sigma_I$. I use the normalized

stress invariants $\sigma'_I = \frac{\sigma_I}{P}$ and $\sigma'_{II} = \frac{\sigma_{II}}{P}$ and solve

$$\sigma'_{II,F} = -\sigma'_I = -\frac{1}{e_F} \sqrt{k_t - \sigma'_I(\sigma'_I + 1 - k_t)} \quad (3.28)$$

to get

$$\sigma_I^p = \frac{(k_t - 1) - \sqrt{(1 - k_t)^2 + 4k_t(1 + e_F^2)}}{2(1 + e_F^2)}, \quad (3.29)$$

where the superscript p denote the fracture point. Now I compute slope the derivative of the plastic potential G

$$\frac{\partial \sigma'_{II,G}}{\partial \sigma'_I} = \frac{1}{e_G} \frac{-2\sigma'_I - 1 + k_t}{2\sqrt{k_t - \sigma'_I(\sigma'_I + 1 - k_t)}} \quad (3.30)$$

I replace σ'_I above by Equation 3.29 in the derivative to get the slope of the tangent at this precise point and get

$$\left. \frac{\partial \sigma'_{II,G}}{\partial \sigma'_I} \right|_{\sigma_I^p} = \frac{1}{e_G e_F} \left(1 - \frac{(1 + e_F^2)}{1 + \sqrt{1 + 4\frac{k_t}{(1-k_t)^2}(1 + e_F^2)}} \right) \quad (3.31)$$

For the elliptical yield curve without tensile strength ($k_t = 0$),

$$\left. \frac{\partial \sigma'_{II,G}}{\partial \sigma'_I} \right|_{\sigma_I^p, k_t=0} = \frac{1}{e_G} \frac{(1 - e_F^2)}{2e_F} \quad (3.32)$$

Therefore, the fracture angle is

$$\theta_{e,nn}(e_F, e_G) = \frac{1}{2} \arccos \left(\frac{1}{e_G} \frac{(1 - e_F^2)}{2e_F} \right) \quad (3.33)$$

I test this prediction in Chapter 5. Note that when $e_F = e_G$, Equation 3.33 reduces to Equation 3.27.

3.4.4 Mohr-Coulomb yield curve with shear only

As shown in Section 2.2.3, the behavior of this Mohr–Coulomb yield curve is complicated, because the plastic potential does not define the flow rule as for the elliptical yield curve. Because the flow rule is non-normal, I consider here the two cases where the fracture angle is set by (1) the internal angle of friction, Equation (3.1), and (2) by the dilatancy angle, Equation (3.2).

If determined by the internal angle of friction, the theoretical fracture angle is the same along the linear limbs and is given by the slope μ , as

$$\theta_{MCS,n}(\mu) = \frac{1}{2} \arccos(\mu). \quad (3.34)$$

If determined by the angle of dilatancy, computing the angle of fracture of this Mohr–Coulomb yield curve is not straightforward. The flow rule is the result of states that are viscous in divergence and plastic in shear, see Section 2.2.3.2. For this reason, I cannot define the fracture angle as for the other yield curves, but assume that the fracture angle is close to 45° for all slope parameters μ : the flow rule is plastic in shear and viscous in divergence or convergence. This means that I consider the slope of tangent to the plastic potential $\tan(\gamma_G) = \mu_G = 0$, so $\delta = \arcsin(\mu_G) = 0$, leading to

$$\theta_{MCS,nn} = \frac{\pi}{4}. \quad (3.35)$$

3.4.5 Mohr-Coulomb yield curve with elliptical plastic potential

If I consider the coulombic theory of the internal angle of friction, then the fracture angle would be the same as in the previous section for every plastic potential

$$\theta_{\text{MCE},n}(\mu) = \frac{1}{2} \arccos(\mu). \quad (3.36)$$

If the angle of dilatancy from the Roscoe angle determines the angle of fracture, the orientation of the flow rule at the fracture state sets the fracture angle. I use the normalized stress invariant $\sigma'_I = \frac{\sigma}{P}$ and $\sigma'_{II} = \frac{\sigma_{II}}{P}$. For uniaxial compression, as described in Section 3.4.1, the stress state at fracture σ_I^{lp} satisfies

$$\sigma'_{II}{}^{lp} = -\sigma_I^{lp} = -\mu\sigma_I^{lp} + k_t\mu, \quad (3.37)$$

which gives

$$\sigma_I^{lp} = \frac{k_t\mu}{\mu - 1}. \quad (3.38)$$

I insert this result into Equation (3.30) and get

$$\left. \frac{\partial \sigma'_{II,G}}{\partial \sigma_I} \right|_{\sigma_I^{lp}} = \frac{1}{e} \frac{-2 \frac{k_t}{\mu-1} - 1 + k_t}{2\sqrt{k_t - \frac{k_t\mu}{\mu-1} \left(\frac{k_t\mu}{\mu-1} + 1 - k_t \right)}}, \quad (3.39)$$

from which I obtain an equation for the theoretical fracture angle

$$\theta_{\text{MCE},nn} = \frac{1}{2} \arccos \left(\frac{1}{e} \frac{-2 \frac{k_t\mu}{\mu-1} - 1 + k_t}{2\sqrt{k_t - \frac{k_t\mu}{\mu-1} \left(\frac{k_t\mu}{\mu-1} + 1 - k_t \right)}} \right). \quad (3.40)$$

Figure 3.8 shows the evolution of the theoretical fracture angle for varying parameters μ , e , and k_t . Observed fracture angles in pack ice are measure between 15° and 25° (Cunningham et al., 1994; Hutter and Losch, 2020). Observations report an internal angle of friction ϕ in the range $[0.6, 0.8]$ (Schulson, 2004; Weiss et al., 2007). From these theoretical prediction, I expect that e should be below 2 and k_t below 0.1 to reproduce the observed fracture angles.

3.4.6 Coulombic yield curve (or Truncate ellipse)

Applying the theory of Mohr's circle and the internal angle of friction to the Coulombic yield curve explains why the non-differentiable corners in the yield curve lead to instabilities. The tangent does not vary smoothly, and the reconstructed yield curve in the failure plane (σ, τ) is discontinuous (Figure 3.9, red line). When the stress states fall on only one of the two parts (ellipse or limb), the conjugate faults form as expected (Figure 4.12b). Using Equation (3.27), with μ as the slope of the Mohr-Coulomb limbs of the Coulombic yield curve, the fracture angle is given by

$$\theta_{c,n}(\mu) = \frac{1}{2} \arccos(\mu), \quad (3.41)$$

which is identical to Equation (3.16).

The Coulombic yield curve with an internal angle of friction of 90° ($\mu = 1$) and no cohesion ($c = 0$) (also called the Truncated Ellipse Method (TEM) in Hibler and

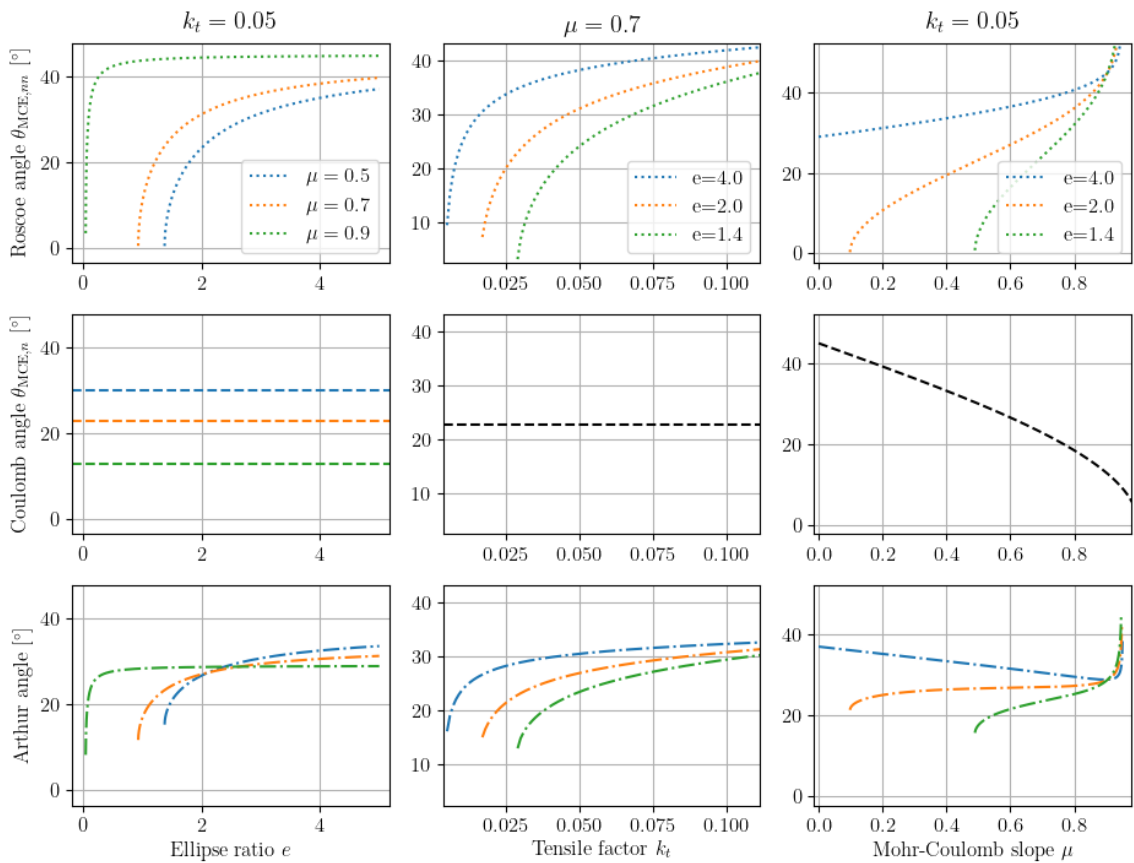


Figure 3.8: Theoretical fracture angles for the Mohr–Coulomb yield curve with elliptical plastic potential. Each row shows the theoretical prediction for a different theory: the Roscoe angle (Equation 3.40), the Coulomb angle (Equation 3.36) and the Arthur angles (the average of both). Each column shows the evolution of the fracture angle for different set of parameters e , k_t , and μ . The colors denote the same parameters per column. The black color denote the case when the parameters have no incidence of the theoretical prediction.

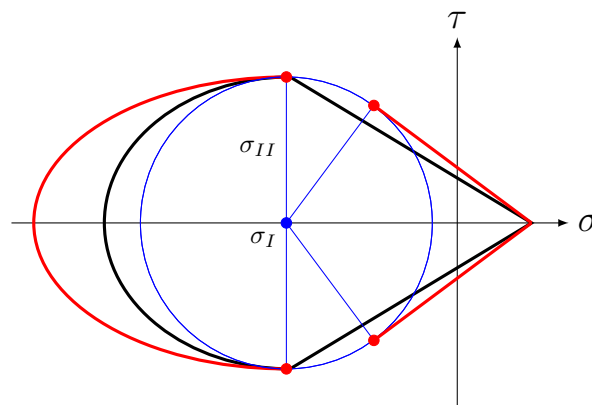


Figure 3.9: Mohr’s circle applied to the Coulombic yield curve (in black) in σ, τ space, the Mohr’s circle for the cusps between the elliptical cap and the Mohr–Coulomb linear limbs (blue circle), and the yield curve in (σ, τ) space (red). By combining the two regimes, for the same Mohr’s circle, two different angles coexist (red circles) and are apart from each other.

Schulson, 1997, Appendix) only has one possible solution with an angle of fracture equal to 0 degrees (i.e., conjugate pair of fracture are not possible). Zero cohesion implies that the ice will deform, even for nearly no stress, which is unphysical.

I now consider the dilatancy angle relationship for this yield curve. The plastic potential is smooth for the whole yield curve but is non-normal along Mohr–Coulomb limbs, excepted in one single point. Therefore, the fracture angle would be the same as for the elliptical yield curve with normal flow rule on the elliptical cap, and it is the same fracture angle as defined in Section 3.4.5 on the Mohr–Coulomb limbs.

$$\theta_{c,nn}(\mu) = \frac{1}{2} \arccos \left(\frac{1 - \frac{-2k_t(\mu+1)}{\mu-1} - 1}{e 2\sqrt{k_t - \frac{k_t\mu}{\mu-1} \left(\frac{k_t\mu}{\mu-1} + 1 - k_t \right)}} \right) \quad (3.42)$$

Note that for the initial Coulombic yield curve (Hibler and Schulson, 2000), the transition between viscous and plastic behavior on the Mohr–Coulomb limbs is not well defined. As ζ reaches the maximum ζ_{max} , η has no maximum value (Equation 2.68 in Section 2.2.4).

3.4.7 Teardrop yield curve with normal flow rule

This teardrop yield curve has a normal flow rule so both theory from Roscoe and Coulomb are valid and equal, therefore I use the fracture angle prediction of Section 3.3.1. The derivation of the fracture angle for the teardrop yield curve is complex because the equation of the yield curve is cubic. I use the normalized stress invariants $\sigma'_I = \frac{\sigma_I}{P}$ and $\sigma'_{II} = \frac{\sigma_{II}}{P}$. I use here the standard notation for tensile strength factor k_t (König Beatty and Holland, 2010), instead of the notation a in Zhang and Rothrock (2005).

$$-\sigma'_{I,s} = -(\sigma'_{I,s} - k_t)\sqrt{1 + \sigma'_{I,s}}. \quad (3.43)$$

Which can be written in the cubic form $x^3 + a_2x^2 + a_1x + a_0$

$$\sigma'^3_{I,s} - 2k_t\sigma'^2_{I,s} + (k_t^2 - 2k_t)\sigma'_{I,s} - k_t^2 = 0. \quad (3.44)$$

This equation can be solved by using Vieta's substitution (Bronshtein et al., 2015): I define Q and R

$$Q = \frac{3a_1 - a_2^2}{9} = \frac{-6a - a^2}{9} \quad (3.45)$$

$$R = \frac{9a_1a_2 - 27a_0 - 2a_2^3}{54} = \frac{18a^3 - 36a^2 - 27a^2 - 16a^3}{54} \quad (3.46)$$

from which I compute the determinant

$$D = Q^3 + R^2 \quad (3.47)$$

If $D < 0$, then three distinct real solutions exist. Note that, because I compute the intersection of two curves (the axis $\sigma_{II} = -\sigma_I$, and the yield curve), the solutions

are real and not complex. The three real solutions are defined by

$$x_1 = 2\sqrt{-Q} \cos\left(\frac{\theta}{3}\right) - \frac{1}{3}a_2 \quad (3.48)$$

$$x_2 = 2\sqrt{-Q} \cos\left(\frac{\theta + 2\pi}{3}\right) - \frac{1}{3}a_2 \quad (3.49)$$

$$x_3 = 2\sqrt{-Q} \cos\left(\frac{\theta + 4\pi}{3}\right) - \frac{1}{3}a_2 \quad (3.50)$$

where

$$\theta = \cos^{-1}\left(\frac{R}{\sqrt{-Q^3}}\right) \quad (3.51)$$

Among these three solutions, x_1 and x_3 are positive and x_2 is negative (not shown). I search for a negative solution because I only consider a compressive state (i.e., $\sigma_I < 0$), so x_2 is the correct intersection solution.

For details, the first solution x_1 is the intersection of the yield curve and the axis defined by $\sigma_{II} = -\sigma_I$ for $\sigma_I > k_t$, while the third solution is the intersection point of the yield curve symmetrical compared to the axis σ_I and comes from the square power used between Equations (3.43) and (3.44), $x_3 \in [0, k_t]$.

The theoretical fracture angle is given by

$$\theta_{TD,n} = \frac{1}{2} \arccos\left(-\frac{\partial\sigma'_{II}}{\partial\sigma'_I}(k_t, x_2)\right) \quad (3.52)$$

with the slope of the yield curve teardrop yield curve

$$\frac{\partial\sigma'_{II}}{\partial\sigma'_I}(k_t, x_2) = -\frac{2 - k_t + 3x_2}{2\sqrt{1 + x_2}}. \quad (3.53)$$

Figure 3.10 shows the theoretical fracture angle as a function of the tensile strength k_t .

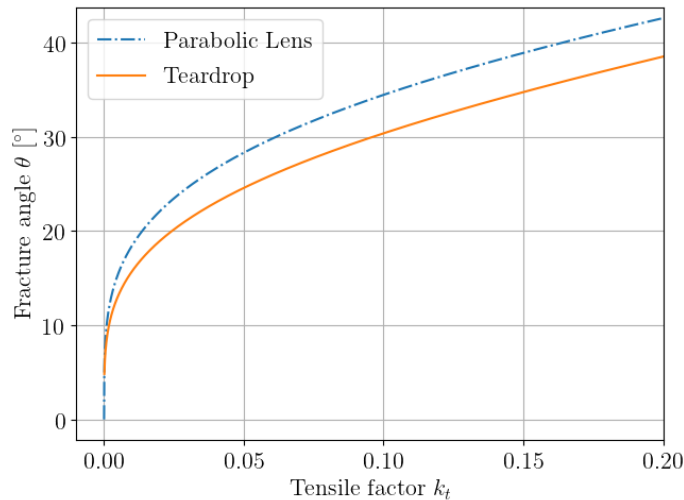


Figure 3.10: Theoretical fracture angle for the teardrop (TD) yield curve and the Parabolic Lens (PL) yield curve with normal flow rules as function of the tensile factor k_t .

3.4.8 Parabolic lens yield curve with normal flow rule

As for the teardrop yield curve, the flow rule is normal; therefore, I use only Section 3.3.1. The derivation of the fracture angle for the parabolic lens yield curve is simpler than for the teardrop because the equation is only quadratic. First, I determine where the axis σ_2 intercept the yield curve. I use $\sigma'_I = \frac{\sigma_I}{P}$ and $\sigma'_{II} = \frac{\sigma_{II}}{P}$ and $k_t = a$.

$$-\sigma_I^{lp} = -(\sigma_I^{lp} - k_t)(\sigma_I^{lp} + 1), \quad (3.54)$$

and its solution

$$\sigma_I^{lp} = \frac{k_t - \sqrt{k_t^2 + 4k_t}}{2}. \quad (3.55)$$

I exclude the positive solution, as the intersection point is negative. I then compute the slope of this yield curve

$$\frac{\partial \sigma'_{II}}{\partial \sigma'_I}(\sigma'_I) = 1 - k_t + 2\sigma'_I, \quad (3.56)$$

and insert the intersection point

$$\frac{\partial \sigma'_{II}}{\partial \sigma'_I}(\sigma_I^{lp}) = 1 - \sqrt{k_t^2 + 4a}, \quad (3.57)$$

so that the fracture angle as a function of k_t is given by

$$\theta_{PL,n}(k_t) = \frac{1}{2} \arccos(1 - \sqrt{k_t^2 + 4k_t}). \quad (3.58)$$

Figure 3.10 shows the evolution of $\theta_{PL,n}$ as function of the tensile factor k_t .

3.5 Summary

In this chapter, I first described two theories of the orientation of shear bands, both based on observations of deformations in granular materials. The first one by Coulomb (1773) uses the internal angle of friction, the second one by Roscoe (1970) takes into account the granular interaction at the fracture line. I apply both theories to the sea ice modeling framework to derive theoretical fracture angles. With these two theories, I took into account both normal flow rule and non-normal flow rule rheologies. Finally, I compute predictions for fracture angle in uni-axial compression for each rheology in Chapter 2.

In the following chapters, I investigate the modeled fracture angles in the uni-axial compression setup and compare them to the theoretical fracture angles. Chapter 4 presents the effects of the experimental setup of the idealized setup and shows the results of the fracture angle for the standard rheology (the elliptical yield curve with normal yield curve) as well as the fracture angles with the Coulombic yield curve. In Chapter 5, I investigate the effect of using the non-normal flow rule with an elliptical yield curve. Chapter 6 presents the modeled angles with the alternative rheologies: The Mohr–Coulomb yield curves with the shear flow rule, the Mohr–Coulomb yield curves with with elliptical plastic potential, and the teardrop and parabolic lens yield curves with normal flow rule.

Chapter 4

Simulating intersection angles between conjugate faults in sea ice with different VP rheologies

Note: The present chapter is identical to Ringeisen et al. (2019), peer-reviewed paper published in the journal *The Cryosphere* the 9th April 2019, at the exception of the appendix that has been moved into the Chapter 3

Authors Contributions: I designed the experiments, ran the simulations, and interpreted the results with the help of ML and LBT. NH contributed to the discussion on LKFs in simulations and observations. I prepared the paper with contributions from all co-authors.

Abstract

Recent high-resolution pan-Arctic sea ice simulations show fracture patterns (linear kinematic features or LKFs) that are typical of granular materials but with wider fracture angles than those observed in high-resolution satellite images. Motivated by this, ice fracture is investigated in a simple uni-axial loading test using two different viscous-plastic (VP) rheologies: one with an elliptical yield curve and a normal flow rule and one with a Coulombic yield curve and a normal flow rule that applies only to the elliptical cap. With the standard VP rheology, it is not possible to simulate fracture angles smaller than 30° . Further, the standard VP model is not consistent with the behavior of granular material such as sea ice because (1) the fracture angle increases with ice shear strength; (2) the divergence along the fracture lines (or LKFs) is uniquely defined by the shear strength of the material with divergence for high shear strength and convergent with low shear strength; (3) the angle of fracture depends on the confining pressure with more convergence as the confining pressure increases. This behavior of the VP model is connected to the convexity of the yield curve together with use of a normal flow rule. In the Coulombic model, the angle of fracture is smaller ($\theta = 23^\circ$) and grossly consistent with observations. The solution, however, is unstable when the compressive stress is too large because of non-differentiable corners between the straight limbs of the Coulombic yield curve and the elliptical cap. The results suggest that, although at first sight the large-scale patterns of LKFs

simulated with a VP sea ice model appear to be realistic, the elliptical yield curve with a normal flow rule is not consistent with the notion of sea ice as a pressure-sensitive and dilatant granular material.

4.1 Introduction

Sea ice is a granular material, that is, a material that is composed of ice floes of different sizes and shapes (Rothrock and Thorndike, 1984; Overland et al., 1998). In most large-scale models, sea ice is treated as a viscous–plastic continuum. It deforms plastically when the internal stress becomes critical in compression, shear, or tension; it deforms as a very viscous (creep) flow when the internal stress is relatively small (e.g., Hibler, 1979; Zhang and Hibler, 1997; Hunke and Dukowicz, 1997). The corresponding highly nonlinear sea ice momentum equations can be solved with modern numerical solvers to reproduce, in a qualitative way, observed linear patterns of sea ice deformation within reasonable computing time (Hutchings et al., 2004; Lemieux et al., 2010; Losch et al., 2010; Hutter et al., 2018). These linear kinematic features (LKFs) are places of large shear and divergence (Kwok, 2001). Leads that open along LKFs are responsible for an emergent anisotropy of such models, affecting the subsequent dynamics, mass balance, and the heat and matter exchanges between the ocean, ice, and atmosphere. It is therefore important to investigate whether sea ice fracture is represented accurately in continuum sea ice models.

The sea ice dynamics are complicated because of sharp spatial changes in material properties associated with discontinuities (e.g., along sea ice leads or ridges) and heterogeneity (spatially varying ice thickness and concentration). The sea ice momentum equations are difficult to solve numerically because of the nonlinear sea ice rheology. Since the first sea ice dynamics model, the elastic–plastic sea ice model based on data collected during the Arctic Ice Dynamics Joint Experiment (AIDJEX; Coon et al., 1974), several approaches to modeling sea ice have been developed. Sea ice has been modeled as an incompressible fluid (Rothrock, 1975c), a viscous–plastic (VP) material (Hibler, 1979), an elastic–viscous–plastic (EVP) material (Hunke, 2001b), a granular material (Tremblay and Mysak, 1997), an elastic anisotropic plastic (EAP) medium (Wilchinsky and Feltham, 2006a), an elastic–decohesive medium (Schreyer et al., 2006), an elasto–brittle (EB) material (Rampal et al., 2016), and a Maxwell(viscous)–elastic–brittle (MEB) material (Dansereau et al., 2016). The actual number of approaches to sea ice modeling in the community, however, is much smaller. For example, 30 out of 33 global climate models in CMIP5 use some form of the standard VP rheology (Stroeve et al., 2014).

In spite of its success, the standard VP rheology is not undisputed. Coon et al. (2007) critically reviewed the assumptions behind current modeling practice since the original model of Coon et al. (1974), namely the zero tensile strength (ice is a highly fractured material) and isotropy assumptions of the sea ice cover and the rheological model. Originally, Coon et al. (1974) assumed sea ice to have cracks in all directions, justifying isotropic ice properties and isotropic rheologies. The use of continuum models such as the standard VP model for high-resolution simulations (grid spacings of 1–10 km) is also debated since the grid size approaches a typical floe size and clearly violates the continuum assumption. For instance, recent high-resolution simulations using the VP model used spatial resolution of approximately

500 m for a regional domain (Wang et al., 2006) and 1 km for a pan-Arctic domain (Hutter et al., 2018). It can be argued that if the mode of deformation of a single floe is similar to that of an aggregate of floes, a given rheology developed for a continuum can still be applicable at spatial resolutions of the order of the floe size (Overland et al., 1998; Feltham, 2008, Appendix C), but the validity of a given flow rule across scales is not clear. At any scale, the assumption of viscous creep for small deformations is not physical, and an elastic model would be appropriate for low stress states. The long viscous timescale, compared to the synoptic timescale of LKFs, of order 30 years (Hibler, 1979), however, allows viscous deformation to be viewed as a small numerical regularization with few implications for the dissipation of mechanical energy from the wind or ocean current (Bouchat and Tremblay, 2014), and the ice model can be considered an ideal plastic material. Tsamados et al. (2013) included anisotropy explicitly in a VP model and show that it improved the representation of ice thickness and ice drift compared to an EVP model. Alternative VP rheologies were never widely used in the community. These include a Coulombic yield curve with a normal flow rule (Hibler and Schulson, 2000), a parabolic lens and a tear drop (Pritchard, 1975), a diamond-shaped yield curve with normal flow rules (Zhang and Rothrock, 2005), a Mohr–Coulomb yield curve with a double-sliding deformation law (Tremblay and Mysak, 1997), or a curved diamond (Wang, 2007).

Previously, fracture lines (LKFs) in the pack ice were explained by brittle fracture (Marko and Thomson, 1977). Similar fracture patterns were also observed, from the centimeter scale in the lab to hundreds of kilometers in satellite observations (Schulson, 2004; Weiss et al., 2007). The scale invariance of the fracture processes at the floe scale has not been shown. This may come from a lack of observations at both high spatial and temporal resolution. Based on satellite observations (e.g., RADARSAT Geophysical Processor System, RPGS, or Advanced Very-High-Resolution Radiometer, AVHRR) and in situ internal ice stress measurements (e.g., from the Surface Heat Budget of the Arctic Ocean, SHEBA, experiment), Weiss et al. (2007) proposed to model winter sea ice as a material that undergoes brittle failure with subsequent inelastic deformation by sliding along LKFs. This idea was formalized with an additional parameterization to simulate damage associated with brittle fracture in an elasto–brittle (EB) and Maxwell–elasto–brittle (MEB) model (Girard et al., 2011; Rampal et al., 2016; Dansereau et al., 2016). We note that subsequent deformation in this model is considered to be elastic deformation (EB) or visco–elastic deformation (MEB) instead of plastic. That is, in the EB and MEB approaches, the material does not weaken when fracture occurs, but rather the Young’s modulus is reduced, leading to larger elastic deformation for the same stress. From the scaling behavior of simulated sea ice deformation fields of EVP models (with 12 km grid spacing), it was found that the heterogeneity and the intermittency of deformation in the VP model are not consistent with Radarsat Geophysical Processor System (RGPS) data (Girard et al., 2009). In contrast, VP models were shown to be indeed capable of simulating the probability density functions (PDFs) of sea ice deformations and some of the scaling characteristics over the whole Arctic in agreement with the same observations, either with sufficient resolution (Spren et al., 2017; Hutter et al., 2018) or with tuned shear and compressive strength parameters (Bouchat and Tremblay, 2017).

High-resolution sea ice models simulate LKF patterns in pack ice, where they appear as lines of high deformation (Hutchings et al., 2005; Hutter et al., 2018). Previously fractured ice will be weaker and will affect future sea ice deformation

fields. The weakening associated with shear deformation results from divergence and a reduction in ice concentration along the LKFs. This mechanism introduces an anisotropy in high-resolution simulations that is similar to observations with comparable spatial resolution. Lead characteristics, including intersection angles between LKFs, were studied a number of times (Lindsay and Rothrock, 1995; Hutchings et al., 2005; Wilchinsky et al., 2010; Bröhan and Kaleschke, 2014; Wang et al., 2016; Hutter et al., 2019). These studies show that VP models produce LKFs with various confinements, scales, resolutions, and forcings. From observations with different instruments (Landsat, Seasat/SAR, areal photographs, AVHRR), typical fracture angles between intersecting LKFs of $(15 \pm 15)^\circ$ emerge at scales from 1 to 100 km (Erlingsson, 1988; Walter and Overland, 1993). Hutter et al. (2019) present an LKF tracking algorithm and show that fracture angles (half of the intersection angles) between LKFs in RGPS data follow a broad distribution that peaks around 20° , in line with previous assessments (e.g., Walter and Overland, 1993). Hutter et al. (2019) also show that the distribution of fracture angles in a VP simulation with 2 km grid spacing is biased, with a high modal value of 45° and with too few small intersection angles between 15 and 25° . The observed bias motivates the present investigation of the dependence of fracture angles in different VP rheologies and model settings, that is, scale, resolution, boundary conditions, model geometry, and variability in initial ice thickness field.

The simulation of fractures in sea ice models has been studied in idealized model geometries before. Hibler and Schulson (2000) investigated the effect of embedded flaws – that favor certain angles of fractures – in idealized experiments using a Coulombic yield curve. Hutchings et al. (2005) showed that LKFs can be simulated with an isotropic VP model using an idealized model geometry. The shape of the elliptical yield curve (ratio of shear to compressive strength) in the standard VP model determines if ice arches can form in an idealized channel experiment (Hibler et al., 2006; Dumont et al., 2009). Pritchard (1988) investigated the yield curve’s mathematical characteristics and derived angles between the principal stress directions and characteristics directions that depend on the tangent to the yield curve. These results show that stress states exist in plastic materials where no LKFs form and were later used to build a yield curve (Wang, 2007). To build an anisotropic rheology, Wilchinsky et al. (2010) used a discrete element model (DEM) in an idealized model domain and showed clear diamond-shaped fracture patterns. Idealized experiments are also used to investigate new rheologies, for example, the Maxwell–elastic–brittle (MEB) rheology (Dansereau et al., 2016) or the material-point method (MPM) (Sulsky et al., 2007), or to study the theoretical framework explaining the fracture angles (e.g., Dansereau et al., 2019, with a Mohr–Coulomb yield criterion in an MEB model). Recently, Heorton et al. (2018) compared simulated fractures by the EVP and EAP models using an idealized model geometry and wind forcing and showed that the anisotropic model creates sharper deformation features. To the best of our knowledge, the dependency of the fracture angles in sea ice on the shape of the yield curve using high-resolution models has not yet been investigated. This is another motivation of this study.

In this paper, we simulate the creation of a pair of conjugate faults in an ice floe with two different VP rheologies in an idealized experiment at a spatial resolution of 25 m. We explore the influence of various parameters of the rheologies and the model geometry (scale, resolution, confinement, boundary conditions, and heterogeneous initial conditions). The remainder of this paper is structured as follows.

Section 4.2 presents the experimental setup: the VP framework (Sect. 4.2.1), the definition of the yield curve (Sect. 4.2.2), and the description of the idealized experiment (Sect. 4.2.3). Section 4.3 presents the results: first the control simulation is presented (Sect. 4.3.1), then we explore the sensitivity of the setup in Sect. 4.3.2 to scale, resolution and longer run time (Sect. 4.3.2.1), modified boundary conditions and lateral confinement (Sect. 4.3.2.2), and to heterogeneity in initial conditions (Sect. 4.3.2.3). Finally, we consider the effects of two different yield curves with different flow rules in Sect. 4.3.3: the elliptical (Sect. 4.3.3.1) and the Coulombic yield curve (Sect. 4.3.3.2). Discussion and conclusions follow in Sects. 4.4 and 4.5.

4.2 Experimental setup

4.2.1 Viscous–plastic model

We use the Massachusetts Institute of Technology general circulation model (MIT-gcm; Marshall et al., 1997) with its sea ice package that allows for the use of different rheologies (Losch et al., 2010). All thermodynamic processes have been turned off for our experiments. The initial sea ice conditions, mean (grid cell averaged) thickness h and fractional sea ice cover A , are advected by ice drift velocities with a third-order flux limiter advection scheme (Huntdorfer et al., 1995). Ice drift is computed from the sea ice momentum equations

$$\rho h \frac{\partial \vec{u}}{\partial t} = -\rho h f \vec{k} \times \vec{u} + \vec{\tau}_{\text{air}} + \vec{\tau}_{\text{ocean}} - \rho h \nabla \phi(0) + \nabla \cdot \boldsymbol{\sigma}, \quad (4.1)$$

where ρ is the ice density, h is the grid cell averaged sea ice thickness, \vec{u} is the velocity field, f is the Coriolis parameter, \vec{k} is the vertical unit vector, $\vec{\tau}_{\text{air}}$ is the surface air stress, $\vec{\tau}_{\text{ocean}}$ is the ocean drag, $\nabla \phi(0)$ is the gradient of sea surface height, and $\boldsymbol{\sigma}$ is the vertically integrated internal ice stress tensor. The form of $\boldsymbol{\sigma}$ defines the rheology. In the case of the standard VP model described in Hibler (1979), the components of $\boldsymbol{\sigma}$ are defined as

$$\sigma_{ij} = 2\eta \dot{\epsilon}_{ij} + (\zeta - \eta) \dot{\epsilon}_{kk} \delta_{ij} - \frac{P}{2} \delta_{ij}, \quad (4.2)$$

where δ_{ij} is the Kronecker delta, and summation over equal indices is implied. η and ζ are the shear and bulk viscosities, $\dot{\epsilon}_{ij}$ is the strain rate tensor defined as

$$\dot{\epsilon}_{ij} = \frac{1}{2} \left(\frac{\partial u_i}{\partial x_j} + \frac{\partial u_j}{\partial x_i} \right), \quad (4.3)$$

and P is the maximum compressive stress defined as a function of the ice strength parameter P^* , mean sea ice thickness h , and the sea ice concentration A :

$$P = P^* h e^{-C^*(1-A)}, \quad (4.4)$$

where C^* is a free parameter.

The stress tensor $\boldsymbol{\sigma}$ is often expressed in terms of principal stresses σ_1 and σ_2 or stress invariants σ_I and σ_{II} . The principal stresses σ_1 and σ_2 are the principal components or eigenvalues of the stress tensor on a sea ice element. Eigenvalues

always exist because the stress tensor is by definition symmetric. The principal stresses σ_1 and σ_2 can be expressed as a function of σ_{ij} as

$$\sigma_1 = \frac{1}{2} \left(\sigma_{11} + \sigma_{22} + \sqrt{(\sigma_{11} - \sigma_{22})^2 + 4\sigma_{12}^2} \right), \quad (4.5)$$

$$\sigma_2 = \frac{1}{2} \left(\sigma_{11} + \sigma_{22} - \sqrt{(\sigma_{11} - \sigma_{22})^2 + 4\sigma_{12}^2} \right). \quad (4.6)$$

This change of coordinates can then be represented as a rotation of the coordinates by ψ (Fig. 3.2). This angle is (Tremblay and Mysak, 1997)

$$\tan(2\psi) = \frac{2\sigma_{12}}{\sigma_{11} - \sigma_{22}}. \quad (4.7)$$

Any linear combination of the principal stresses consists of stress invariants. One common set of stress invariants is the mean normal stress (σ_I) and the maximal shear stress (σ_{II}). They can be written as

$$\sigma_I = \frac{1}{2}(\sigma_1 + \sigma_2) = \frac{1}{2}(\sigma_{11} + \sigma_{22}), \quad (4.8)$$

$$\sigma_{II} = \frac{1}{2}(\sigma_1 - \sigma_2) = \frac{1}{2}\sqrt{(\sigma_{11} - \sigma_{22})^2 + 4\sigma_{12}^2}. \quad (4.9)$$

4.2.2 Yield curve

The VP rheology was originally developed to simulate ice motion on a basin scale (e.g., Arctic Ocean, Southern Ocean) (Hibler, 1979). In this model, stochastic elastic deformation is parameterized as highly viscous (creep) flow (Hibler, 1977). Ice is set in motion by surface air and basal ocean stresses moderated by internal ice stress. When the internal sea ice stress reaches a critical value in compression, tension, or shear, sea ice fails and relatively large plastic deformation takes place. Internal ice stress below these thresholds leads to highly viscous (creep) flow that parameterizes the bulk effect of many small reversible elastic deformation events. The timescale of viscous deformation is so high ($\simeq 30$ years) that viscous deformation can be seen as regularization for better numerical convergence in the case of small deformation. Plastic deformations are relatively large and irreversible. Viscous deformations are negligibly small; in contrast to elastic deformation, they are also irreversible. The yield criterion is expressed as a 2-D envelope either in principal stress space or stress invariant space with a normal flow rule. The constitutive equations (Eq. 4.2) are derived assuming that the principal axes of stress coincide with the principal axes of strain. The stress state on the yield curve together with the normal flow rule therefore determines the relative importance of divergence (positive or negative) and shear strain rate at a point. The magnitude of the deformation is such that the stress state remains on the yield curve during plastic deformation.

In this study, we use two different yield curves: an elliptical yield curve (Hibler, 1979) and a Coulombic yield curve (Hibler and Schulson, 2000). The elliptical yield curve is used in conjunction with a normal flow rule, while the Coulombic yield curve uses a normal flow rule on the elliptical cap and a flow rule normal to the truncated ellipse for the same first principal stress (Hibler and Schulson, 2000, Appendix A).

For the elliptical yield curve (Fig. 4.1, black line), η and ζ are given by

$$\zeta = \frac{P}{2\Delta}, \quad (4.10)$$

$$\eta = \frac{\zeta}{e^2}, \quad (4.11)$$

with the abbreviation

$$\Delta = \sqrt{\dot{\epsilon}_I^2 + \frac{1}{e^2}\dot{\epsilon}_{II}^2}. \quad (4.12)$$

In this abbreviation, the strain rate invariants are the divergence $\dot{\epsilon}_I = \dot{\epsilon}_{11} + \dot{\epsilon}_{22}$, and the maximum shear strain rate $\dot{\epsilon}_{II} = \sqrt{(\dot{\epsilon}_{22} - \dot{\epsilon}_{11})^2 + 4\dot{\epsilon}_{12}^2}$. $e = a/b$ is the ellipse aspect ratio with the semi-major half-axes a and b (shown in blue in Fig. 4.1). The ellipse aspect ratio e defines the shear strength $S^* = P^*/2e$ of the material as a fraction of its compressive strength (Bouchat and Tremblay, 2017). For the Coulombic yield curve (Fig. 4.1, red curve), the shear viscosity η is capped on the two straight limbs:

$$\eta_{MC} = \min \left\{ \eta, \frac{1}{\dot{\epsilon}_{II}} \left[\mu \left(\frac{P}{2} - \zeta \cdot \dot{\epsilon}_{kk} \right) - c \right] \right\}, \quad (4.13)$$

where μ is the slope of the Mohr–Coulomb limbs (Fig. 4.1), and c is the cohesion value (the value of σ_{II} for $\sigma_I = 0$) defined relative to the tensile strength by $c = \mu \cdot T^*$, where T^* is defined as a fraction of P^* .

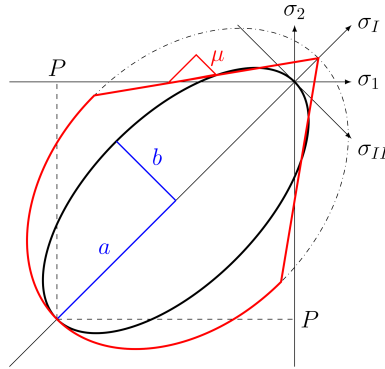


Figure 4.1: Elliptical yield curve (black) with ellipse aspect ratio $e = a/b = 2$. Coulombic yield curve (red) and elliptical capping with internal angle of friction (μ). Both e and μ are measures of the shear strength of the material. The normal flow rule applies only to the elliptical part of the yield curves. For the two straight limbs of the Coulombic yield curve, the flow is normal to the truncated ellipse (dashed-dotted line) with the same first stress invariant. Note that the axes σ_I , σ_2 and σ_I , σ_{II} do not have the same scale.

The theoretical angle of fracture θ can be calculated from the Mohr's circle of stress and yield curve written in the local (reference) coordinate system (Ip et al., 1991; Pritchard, 1988; Hibler and Schulson, 2000). Details are described in Section 3.3. For a Mohr–Coulomb yield criterion, θ follows immediately from the internal angle of friction or the material shear strength. An instructive analogue is the slope of a pile of sand on a table. Moist sand has a higher shear strength, and hence the slope angle can be steeper (i.e., the angle θ is smaller).

4.2.3 Idealized experiment

An idealized compressive test is used to investigate the modes of sea ice fracture (Fig. 4.2). This experiment is standard in engineering (Schulson, 2004; Weiss et al., 2007). The numerical configuration is inspired by Herman (2016) and similar to the one shown in Dansereau et al. (2016). All experiments presented below use the same setup unless specified otherwise. The values of parameters and constants are presented in Table 4.1.

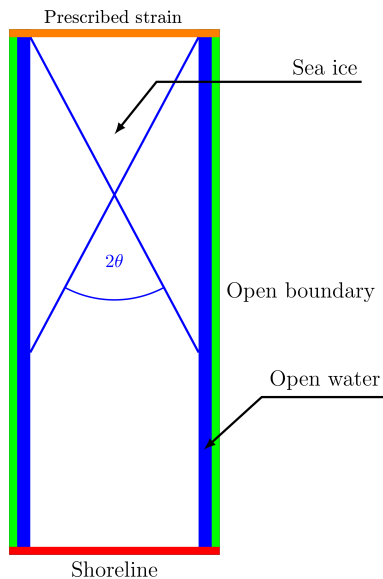


Figure 4.2: Model domain with a solid wall on the southern (red) boundary (Dirichlet boundary conditions with $\vec{u} = 0$) and prescribed southward velocities on the northern orange boundary ($u = 0, v = a_v \cdot t + v_i$; Eq. 4.15) and open boundaries to the east and the west (green) with von Neumann boundary conditions. θ is the measured fracture angle with the blue line representing an LKF.

The model domain is a rectangle of size $10 \text{ km} \times 25 \text{ km}$, except for the experiments presented in Sect. 4.3.2.1 and 4.3.2.2. An ice floe of size $8 \text{ km} \times 25 \text{ km}$, surrounded by 1 km of open water on the eastern and western sides, is compressed with a linearly (in time) increasing strain rate from the north against a solid southern boundary. The eastern and western strips of open water avoid interesting dynamics being confounded by the choice of lateral boundary conditions along the open boundaries. We use a no-slip condition for the southern boundary, constraining lateral ice motion. Note that the results presented below are not sensitive to the choice of boundary condition on the eastern and western boundaries. Because the simulation time and the ice velocities are small, the Coriolis force in the momentum equations are neglected. Ocean and sea ice are initially at rest. The only term left in the momentum equation (Eq. 4.1) that is relevant for our experiment is the stress divergence term, $\nabla \cdot \sigma$. The ice floe has a uniform concentration of 100% and a thickness of 1 m . The spatial resolution of the model is 25 m . The angle of fracture is measured with the angle measuring tool of the GNU Image Manipulation Program (GIMP, <https://www.gimp.org/>, Version 2.8.22, last access: 4 April 2019). All angles measured in this study have an error of approximately 1° . The finite size of the grid spacing widens the deformation line, and the fracture spreads over several pixels because of the obliquity of the fracture. Automatic algorithms

Table 4.1: Model parameters of the reference simulation.

Symbol	Definition	Value	Unit
ρ	Density of ice	910	kg m^{-3}
P^*	Ice strength	27.5	kN m^{-1}
C	Strength reduction parameter	20	
Δ_{\min}	Maximum viscosity	10^{-10}	s^{-1}
$\Delta x, \Delta y$	Grid spacing	25	m
C_w	Water drag coefficient	5.21×10^{-3}	
N_x, N_y	Size of the domain	400×1000	
L_x, L_y	Size of experiment	10×25	km
l_x, l_y	Ice floe's size	8×25	km
A	Initial ice concentration	100	%
h	Initial ice thickness	1.0	m
N_{lin}	No. linear iteration	1500	
N_{nl}	No. nonlinear iteration	1500	
ϵ_{err}	Max. error in LSR	10^{-11}	m s^{-1}
dt	Time step	0.1	s
e	Ellipse ratio (a/b)	2.0	
v_i	Initial velocity	0	m s^{-1}
a_v	Acceleration	$5 \cdot 10^{-4}$	m s^{-2}

for measuring LKF intersection angles are described in Linow and Dierking (2017) and Hutter et al. (2019).

We solve the nonlinear sea ice momentum equations with a Picard or fixed point iteration with 1500 nonlinear or outer-loop iterations. Within each nonlinear iteration, the nonlinear coefficients (drag coefficients and viscosities) are updated and a linearized system of equations is solved with a line successive (over-)relaxation (LSR) (Zhang and Hibler, 1997). The linear iteration is stopped when the maximum norm of the updates is less than $\epsilon_{\text{LSR}} = 10^{-11} \text{m s}^{-1}$, but we also limit the number iterations to 1500. Typically, 1500 nonlinear iterations are required to reach a state close enough to the converged solution. Note that this criterion is much stricter than that proposed by Lemieux and Tremblay (2009) – this is so because of slow convergence due to the highly nonlinear rheology term and the high spatial resolution.

On the open eastern and western boundaries, we use von Neumann boundary conditions for velocity, thickness and concentration, and ice can escape the domain without any restrictions:

$$\left. \frac{\partial u}{\partial x} \right|_{\text{E,W}} = \left. \frac{\partial v}{\partial x} \right|_{\text{E,W}} = \left. \frac{\partial A}{\partial x} \right|_{\text{E,W}} = \left. \frac{\partial h}{\partial x} \right|_{\text{E,W}} = 0, \quad (4.14)$$

where E and W denote the eastern and western boundaries, respectively. Strain is applied to the ice at the northern boundary by prescribing a velocity that increases linearly with time:

$$v|_{\text{N}}(t) = a_v \cdot t + v_i; \quad u|_{\text{N}} = 0; \quad \left. \frac{\partial A}{\partial y} \right|_{\text{N}} = \left. \frac{\partial h}{\partial y} \right|_{\text{N}} = 0, \quad (4.15)$$

where a_v is the prescribed acceleration, and N denotes the northern boundary.

4.3 Results

We use simple uni-axial loading experiments to investigate the creation of pair of conjugate faults and their intersection angle. After presenting the results of simulations with the default parameters (Sect. 4.3.1), we explore the effects of experimental choices: confining pressure, choice of boundary conditions (i.e., von Neumann versus Dirichlet), domain size, and spatial resolution and inhomogeneities (i.e., localized weakness) in the initial thickness and concentration field (Sect. 4.3.2). Finally, we study the behavior of two viscous–plastic rheologies with different yield curves and compare these dependencies to what we can infer from smaller- and larger-scale measurements from laboratory experiment and RGPS observations (Sect. 4.3.3).

4.3.1 Uni-axial compressive test – default parameters

With default parameters (Table 4.1), a diamond-shaped fracture appears in the shear strain rate and divergence fields after a few seconds of integration (Fig. 4.3). After one time step (or 0.1 s), the stress states already lie on the yield curve, and the fracture is readily seen in the deformation fields (divergence and shear). We iterate for a total of 20 s in order for the signal to be apparent in the thickness and concentration fields. We do this to more clearly show the link between position of the stress states on the yield curve and the resulting deformation defined by the normal flow rule in the standard VP rheology of Hibler (1979). The shear deformation ($\dot{\epsilon}_{II}$) shows where the ice slides in friction and deforms plastically. From Fig. 4.3, the simulated intersection angle is $\theta = (34 \pm 1)^\circ$.

After a few time steps, the ice thickness decreases, particularly along the LKFs (Fig. 4.3c) where divergence is maximal. Note that the loading axis in our simple 1-D experiment is also the second principal axis, and consequently the stress states are migrating along the σ_2 axis as the strain rate at the northern boundary increases. Fracture occurs after plastic failure when the stress state reaches the yield curve and the ice starts to move in divergence. This occurs in the half of the ellipse closer to the origin (for $e > 1$) where the normal to the flow rule points in the direction of positive divergence (or first strain rate invariant) (see Fig. 4.4). This explains the simulated divergent flow field and lower ice thickness particularly along LKFs.

4.3.2 Sensitivity experiments

In this section, we test the sensitivity of the standard VP model simulation (Sect. 4.3.1) to the choice of resolution, scale, and run time (Sect. 4.3.2.1), boundary conditions and confinement pressure (Sect. 4.3.2.2), and heterogeneity in the initial sea ice mass field (Sect. 4.3.2.3).

4.3.2.1 Domain size, spatial resolution, and length of integration

The angle of intersection between a pair of conjugate faults does not change with domain size and spatial resolution (Fig. 4.5). This is expected because non-dimensionalizing the divergence of the internal ice stress term (the only term that remains in this simple uni-axial test experiment) by setting $u' = u/U$, $x' = x/L$ gives the same equations in non-dimensional form, irrespective of the initial ice thickness or spatial resolution. Consequently, the control and sensitivity experiments are scale-

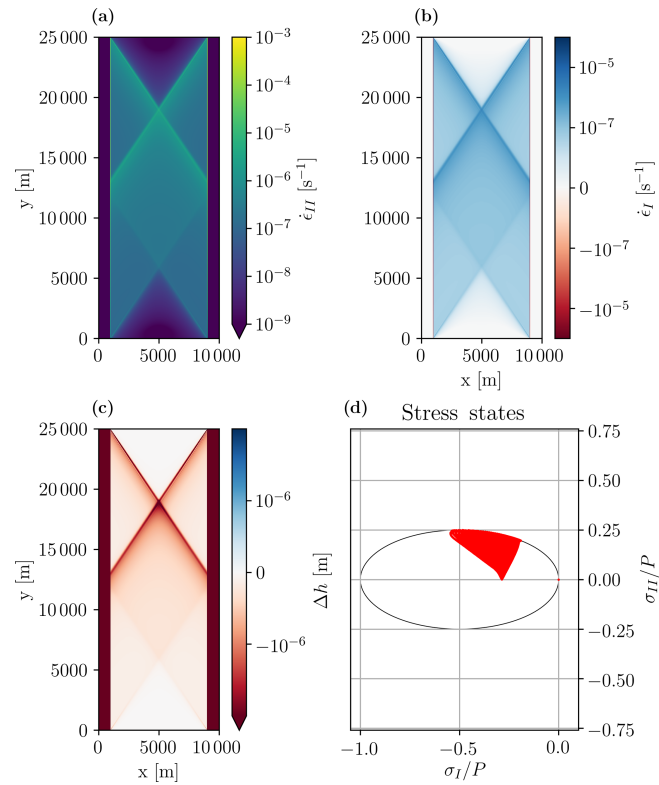


Figure 4.3: (a) First and (b) second strain invariants, (c) ice thickness anomaly ($\Delta h = h - 1$), and (d) stress states in normalized stress invariant space along with the elliptical yield curve after 5 s of integration. The first and second strain invariants represent the divergence and maximum shear strain rate, respectively. The modeled angle of fracture is $\theta = (34 \pm 1)^\circ$.

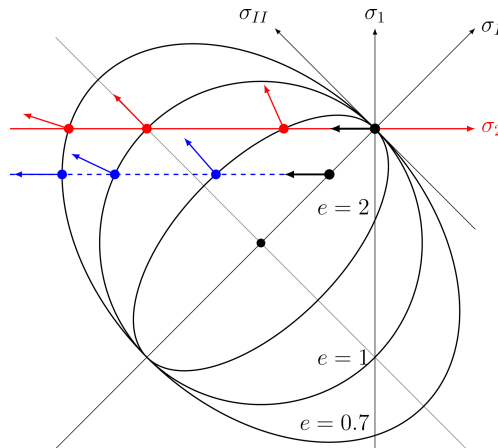


Figure 4.4: Schematic of stress states and failure in principal stress space. Black arrows show how stresses move from zero at the beginning of loading towards the yield curve until failure. Red points show the stress states at failure – the intersection point between the second principal axis 2 (in red) and the elliptical yield curve – for different ellipse ratios $e = 2, 1, 0.7$. The red arrows show the direction of deformation with a normal flow rule. The blue points and arrows show the case when the ice floe is confined and the loading will lead to extra stress in the direction of σ_1 .

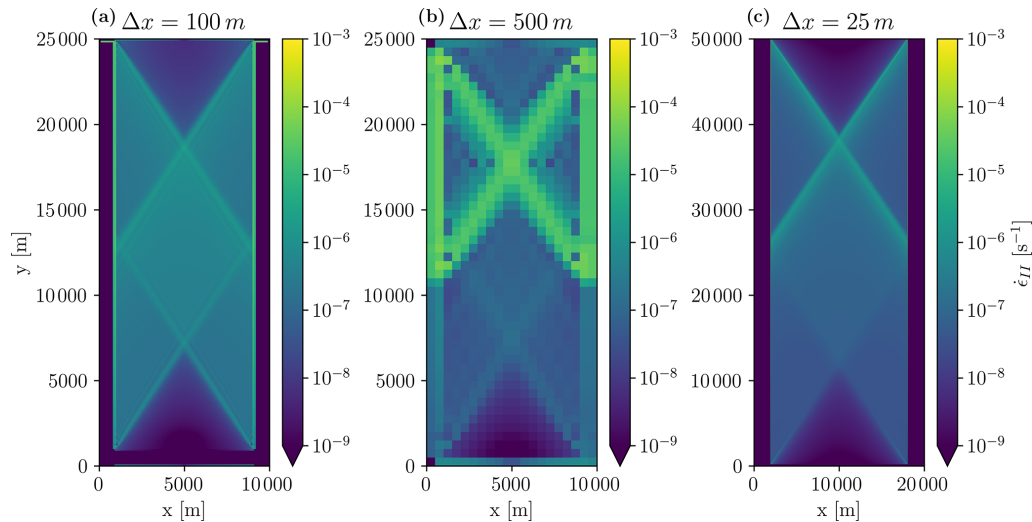


Figure 4.5: Maximum shear strain rate (second strain invariant) after 10 s of integration for the default domain size and $\Delta x = 100$ m **(a)** and 500 m **(b)** and for the default Δx and a doubled domain size of 20 km \times 50 km **(c)**. Note that for the case of the double domain **(c)**, the southward velocity at the northern boundary was also doubled to keep the deformation rate constant and that this simulation is limited to 2 s for numerical efficiency.

independent, and the behavior of the standard VP model can be readily compared with results from RGPS, AVHRR, or laboratory experiments.

Continuing the integration to 2700 s (45 min), compared to 20 s in the reference simulation, leads to the creation of smaller diamond-shaped ice floes due to secondary and tertiary fracture lines (Fig. 4.6). The openings are visible in the thickness and concentration fields with thinner, less concentrated ice in the lead. In this longer experiment, the sea ice also ridges, for instance, at the center of the domain, where the apex of the diamonds fails in compression. There is also some thicker ice at the northern boundary induced by the specified strain rate at the northern boundary. The fracture pattern and presence of secondary and tertiary fracture lines are in line with results from laboratory experiments (Schulson, 2004) and with AVHRR and RGPS observations.

In the following, we always show results after 5 s of integration because our main focus is on the initial fracture of the ice, that is, the instant when the ice breaks for the first time under compression.

4.3.2.2 Boundary conditions and geometry

The dynamics responsible for the ice fracture and location of the fracture (presented above) take place far away from the eastern and western boundaries and therefore do not depend on the choice of the corresponding boundary conditions. We now investigate the sensitivity of the results to the choice of boundary condition at the southern boundary. To this end, we force the fracture line to intersect the southern boundary by reducing the domain size to 10 km \times 10 km with an ice floe of 8 km \times 10 km in the interior. In this case, the fracture develops from corner to corner, and the angle is solely determined by the geometry of the ice floe, that is, $\theta = \arctan(l_x/l_y)$ (Fig. 4.7b). With a free-slip boundary condition at the southern boundary, the fracture angle is similar to the one from the control simulation

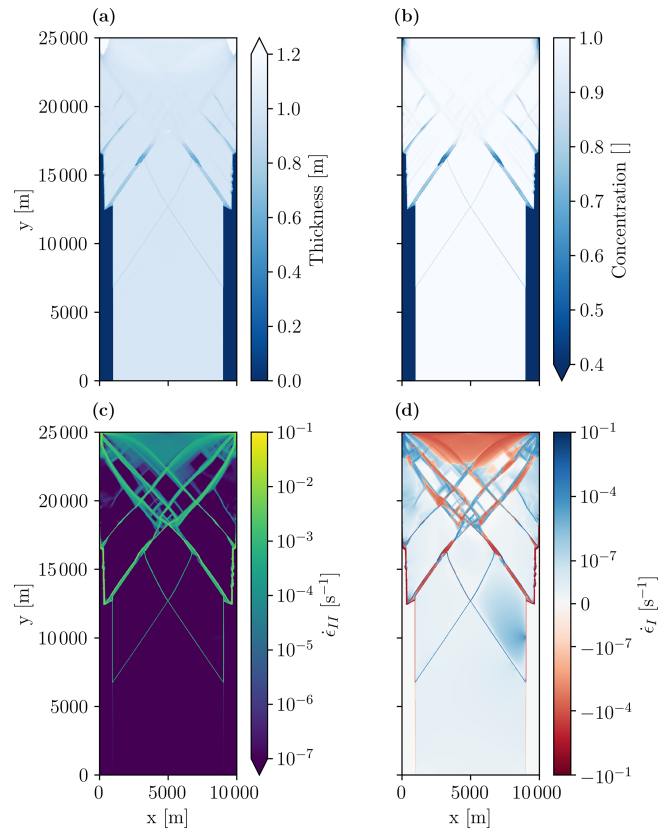


Figure 4.6: Sea ice thickness **(a)**, concentration **(b)**, maximum shear strain rate **(c)**, and divergence **(d)** after 45 min of integration (2700 s) in a uni-axial loading test. To make these longer simulations possible, both nonlinear and linear iterations are limited to 150 per time step. Results show the development of secondary fracture lines in all fields after the first fracture line has formed.

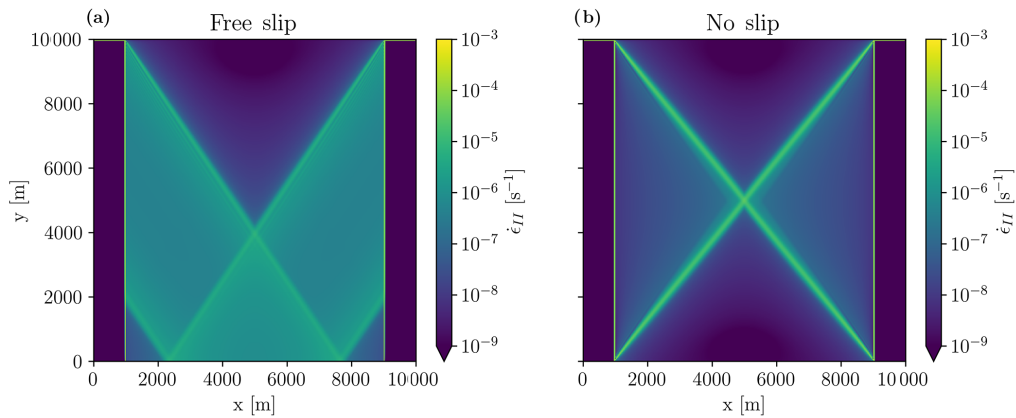


Figure 4.7: Maximum shear strain rate after 5 s of integration in a reduced size domain (8 km \times 10 km) with free-slip **(a)** and no-slip **(b)** boundary conditions. Note that the no-slip boundary condition forces the fracture to occur at the corner of the domain, leading to a larger angle of $\theta = 39^\circ$ versus $34 \pm 1^\circ$ in the control experiment. This suggests that the choice of boundary conditions in current sea ice models needs to be revisited.

(Fig. 4.7a). That is, the no-slip condition concentrates the stress to the corner of the ice floe touching the boundary and predetermines the fracture location. A free-slip boundary condition is therefore considered more physical in such idealized experiments where fractures lines can extend from one boundary to another. This result can have implications for simulation of LKFs in the Arctic that would extend from one boundary to another, for instance in the Beaufort Sea.

No-slip or free-slip boundary conditions have little impact on the fracture angle in the larger domain used in the control run simulation because the LKFs always only touch one boundary and end in open water (results not shown). With the free-slip boundary conditions, the stresses and strains are only different south of the diamond fracture pattern because ice can move along the southern boundary, and the second fracture cannot form.

We now explore the effect of confining pressure on the eastern and western boundaries on the angle of fracture when using a (convex) elliptical yield curve with a normal flow rule. To do so, we replace the open boundaries to the east and the west with solid walls and the open water gaps with ice of thicknesses h_c . Note that the ice strength is linearly related to the ice thickness (Eq. 4.4). Therefore the normal stress at the edge of the floe is completely defined by the thickness of the surrounding ice.

With an increasing lateral confinement pressure (i.e., an increasing ice thickness h_c next to the main floe), all stress states are moved to higher compressive stresses (blue curve in Fig. 4.4), and the fracture angle increases (Fig. 4.8). In this case, the stress states are again migrating in a direction parallel to the σ_2 axis but with a non-zero σ_1 value. The stress states of the ice along the fracture are therefore located in a region of higher compressive stresses on the yield curve where the divergence is reduced or even changes sign. With increasing confinement, the stress states of the ice floe move to more negative values of σ_1 along a line of constant σ_2 (blue line in Fig. 4.4) with deformation moving towards more convergent states. Between $h_c = 0.2$ and $h_c = 0.3$, the regime changes from lead opening to ridging, as the fracture angle increases to values above 45° . This is inconsistent with the behavior of a granular material where the angle of fracture is independent of confining pressure in uni-axial loading laboratory experiment.

4.3.2.3 Effects of the heterogeneity

So far, all initial conditions have been homogeneous in thickness and concentration within the ice floe. In practice, sea ice (in a numerical model but also in reality) is not homogeneous. A local weakness in the initial ice field is likely the starting point of a crack within the ice field (e.g., Herman, 2016, her Fig. 5c). Local failures raise the stress level in adjacent grid cells, and a crack can propagate. Note that the crack propagation in an “ideal” plastic model such as the VP model is instantaneous, and this propagation is not seen between time steps. As a consequence, lines of failure will likely develop between local weaknesses. The location of weaknesses in the ice field together with the ice rheology (yield curve and flow rule) both determine the fracture angles (Hibler and Schulson, 2000; Aksenov and Hibler, 2001). The influence of previous leads on subsequent lead creation have been studied with a discrete element model (Wilchinsky et al., 2011) and has been used to constrain new anisotropic rheologies that include the effects of embedded anisotropic leads (Wilchinsky and Feltham, 2011; Wilchinsky and Feltham, 2012).

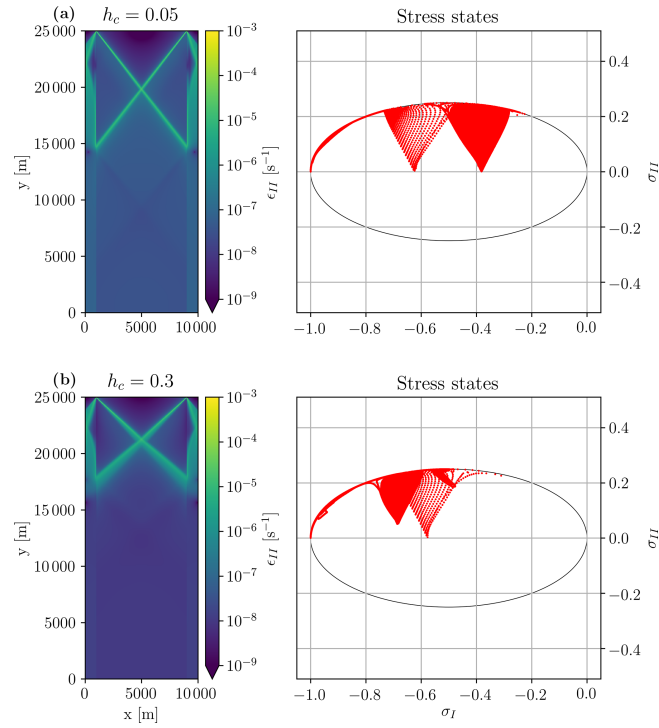


Figure 4.8: Maximum shear strain rates (left) and stress state in stress invariant space (right) after 5 s of integration for different confinement pressure: $h_c = 0.05$ m (a) and $h_c = 0.3$ m (b). Note how stress states with divergent strain rates (a) migrate left towards convergent strain rates (b).

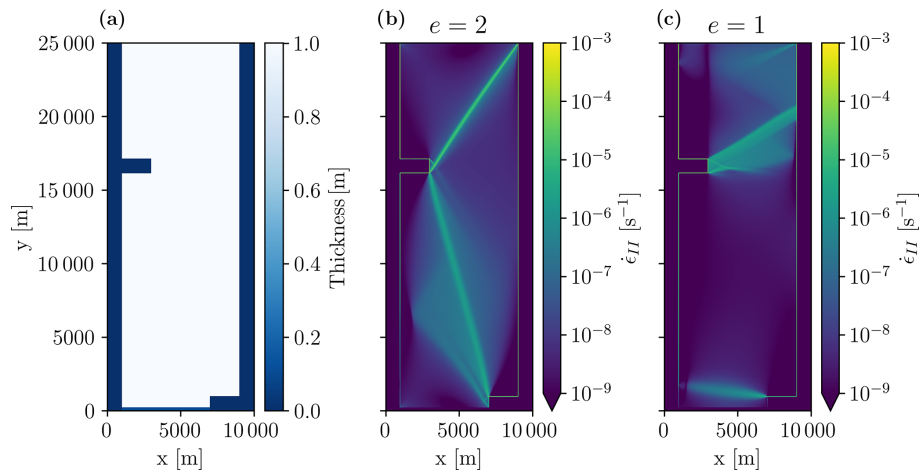


Figure 4.9: Sea ice thickness with two ice-free areas (a) and maximum shear strain rates for two different ellipse aspect ratios (b, c) after 5 s of integration. The position of the ice weaknesses determines the location and angle of the fracture lines, and also the rheology parameter e has an entirely different effect. The main fractures lines are at angles of 25 and 34° for $e = 2.0$ and 57.6° for $e = 1.0$.

To illustrate this behavior, we start new simulations from an initial ice field with two areas of zero ice thickness and zero ice concentration, hence weaker ice (Fig. 4.9a). After 5 s these simulations yield fracture patterns that are dramatically different from those of the control run simulation (Sect. 4.3.1): the fracture lines now start and terminate at the locations of the weak ice areas. Still, changing the shear strength of the ice (by changing e) changes the fracture pattern (Fig. 4.9b and c). With $e = 1$, the angles are much wider than with $e = 2$, which is consistent with the general dependence of fracture angles on e (see Sect. 4.3.3.1). Our simulations cannot lead to conclusive statements about the relative importance of heterogeneity of initial conditions and yield curve parameters for the fracture pattern, but we can state that both affect the simulations in a way that requires treating them separately to avoid confounding effects. Details are deferred to a dedicated study.

4.3.3 Effects of the yield curve on the fracture angle

4.3.3.1 Elliptical yield curve

Keeping $P^* = 27.5 \text{ kN m}^{-1}$ at its default value, the maximal shear strength $S^* = P^*/2e$ is varied by changing the ellipse ratio e . Scaling the absolute values of P^* and S^* while keeping e constant does not change the fracturing pattern as the tangent to the ellipse stays the same (not shown). Changing the ellipse aspect ratio e has a large effect on the fracture angle. The fracture angle decreases monotonically as the shear strength of the material (or e) decreases, from 61° for $e = 0.7$ to 32° for $e = 2.6$. This is clearly inconsistent with the behavior of a granular material; in the sand castle analogue this would correspond to a dry sand castle with steeper walls than a moist sand castle. From the simple schematic of Fig. 4.4, it becomes clear that with increasing e , the intersection of the σ_2 axis with the yield curve gradually migrates from the left side of the ellipse to the right, where the normal to the yield curve points increasingly towards convergent motion. We present a theoretical explanation for the sensitivity of the fracture angle to the shear strength of the material (e , for the ellipse) in Section 3.3 by rewriting the elliptical yield curve in local coordinates in the fracture plane (σ, τ) instead of principal or stress invariant coordinates. The fracture angle is then determined from the slope of the tangent to the yield curve in local coordinates, and this angle follows from the Mohr's circle (see, for instance, Popov, 1976).

Bouchat and Tremblay (2017) suggest a smaller ellipse aspect ratio (e.g., $e = 0.7$) to obtain a closer match with RADARSAT-derived distribution of deformation rates in pan-Arctic simulations at 10 km resolution. From Figs. 4.10 and 4.11, the corresponding fracture angle is $\theta = (61 \pm 1)^\circ$, that is, much larger than that is derived from RADARSAT images. e also changes the distribution of the stress states on the yield curve. As the stress state migrates along the principal stress σ_2 until it reaches the yield curve in our uni-axial compressive test, the stress states are in the second half of the ellipse for $e < 1$ and the resulting deformation is in convergence (or ridging). The ice thickness increases due to ridging along the shear lines (Fig. 4.11). In a longer simulation with $e = 0.7$ (not shown) the ice does not open but only ridges, with thicker ice building up within the ice floe. This is in strong contrast to the results with $e = 2.0$ presented in Sect. 4.3.2.1, where the initial floe breaks up and separate floes form.

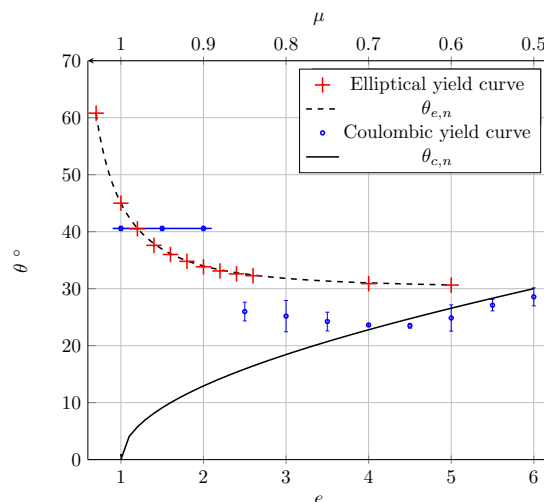


Figure 4.10: Fracture angles as a function of ellipse aspect ratio e with constant P^* (red, bottom scale; Sect. 4.3.3.1). The theoretical relationship $\theta_{e,n} = \frac{1}{2} \arccos \left[\frac{1}{2} \left(1 - \frac{1}{e^2} \right) \right]$ (dashed black curve; Eq. 3.27) fits the modeled angles almost perfectly with $R^2 = 0.9995$ and $\sqrt{\text{VAR}} = 0.089$. The simulated fracture angles for the Coulombic yield curve as a function of the slope of the Mohr–Coulomb limbs (blue, top scale; Sect. 3.4.6) fit the theoretical relationship $\theta_{c,n} = \frac{1}{2} \arccos(\mu)$ only for $\mu \leq 0.7$ (black line; Eq. 3.41). The errors bars mean that there was more than one unique fracture line: for a small μ , the ice breaks easily along the lateral edges of the floe. For $\mu > 0.7$ ($\phi = 44^\circ$), the ambiguity appears because the stress states are both on the linear limbs and on the elliptical cap. For $\mu \geq 0.9$ (blue line), the fracture angle is the same as for the ellipse for $e = 1.4$.

4.3.3.2 Coulombic yield curve

In this section, we replace the elliptical yield curve with a Coulombic yield curve (Hibler and Schulson, 2000). This yield curve consists of a Mohr–Coulomb failure envelope – two straight limbs in principal or stress invariant space with a slope μ – capped by an elliptical yield curve for high compressive stresses. Note that the flow rule applies only to the elliptical cap in this yield curve. For the two straight limbs, the yield curve is normal to the truncated ellipse with the first stress invariant σ_1 . For a Mohr–Coulomb yield curve, the fracture angle depends directly on the slope of the Mohr–Coulomb limb of the yield curve. Section 3.2 provides a theoretical explanation of how the angle of fracture depends on the internal angle of friction.

The slope of the Mohr–Coulomb limbs of the Coulombic yield curve μ is varied between 0.3 and 1.0 (corresponding to an internal angle of friction $\phi = \arcsin(\mu)$ of 17.5 to 90°) to study how the fracture angle depends on the shear strength of the material. In all experiments with the Coulombic yield curve, we use a tensile strength of 5% of P^* and an ellipse ratio $e = 1.4$, following Hibler and Schulson (2000). The tensile strength is introduced mainly for numerical reasons. With zero tensile strength, the state of stress in a simple uni-axial compressive test with no confinement pressure is tangential to the yield curve at the origin (failure in tension) and on the two straight limbs (failure in shear) simultaneously, resulting in a numerical instability. With tensile stress (or confinement pressure) included, the state of stress reaches the yield only on the two limbs of the yield curve (see

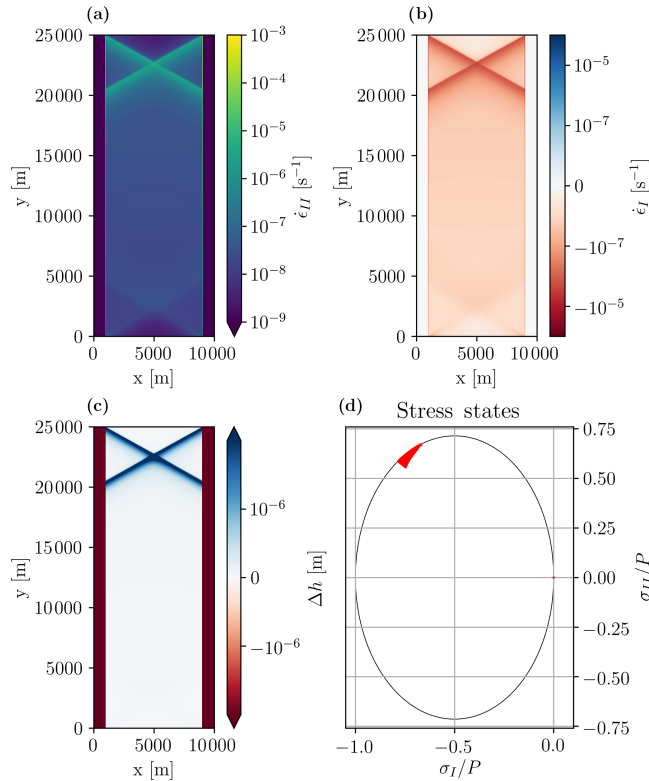


Figure 4.11: Maximum shear strain **(a)**, ice thickness anomaly **(b)**, divergence **(c)**, and stress state in stress invariant space **(d)** after 5 s of integration for a smaller ellipse aspect ration ($e = 0.7$ compared to $e = 2$ in the reference run in Sect. 4.3.1). Compared to the control run on Fig. 4.3, the angle of fracture is larger ($\theta = (61 \pm 1)^\circ$), the stress states are in the second half of the ellipse (with strain rates pointing into the convergent direction), and there is convergence along the fracture lines **(b)** in agreement with the schematic in Fig. 4.4.

Fig. 4.12a).

For the Coulombic yield curve, there are two distinct regimes of failure. When the σ_2 axis intersects the yield curve on the two straight limbs, which happens for our configuration for angles of friction $\phi < 45^\circ$ (Fig. 4.12a, left hand side for $\mu = 0.7$ or $\phi = 44^\circ$), the angle of fracture $\theta = \pi/4 - \phi/2$ as per standard theory (Section 3.2). When the σ_2 axis intersects the yield curve on the elliptical cap, which happens for $\phi > 45^\circ$ (Fig. 4.12c, for $\mu = 0.95$ or $\phi = 72^\circ$), we observed a discontinuity in the fracture angle associated with the non-differentiable corner in the yield curve. Note that this corner cannot be removed (by changing the P^* and e of the elliptical cap) as the two straight Mohr–Coulomb limbs are defined as a truncation of the ellipse. For $\phi \approx 45^\circ$ in our configuration, the numerical solver has difficulties reaching convergence because of the non-differentiable corner in the yield curve between the elliptical cap and the two straight limbs (Fig. 4.12b for $\mu = 0.8$ or $\phi = 53^\circ$). Finally for very small angles ϕ , a large number of fractures, as opposed to single well defined fracture lines, appear because of the weakness of the material in shear. This behavior is not something that is typically observed in a uni-axial compressive test of a granular material which generally have higher shear resistance. Note that the value of ϕ that is characteristic of the individual regimes depends on the amount of tensile strength.

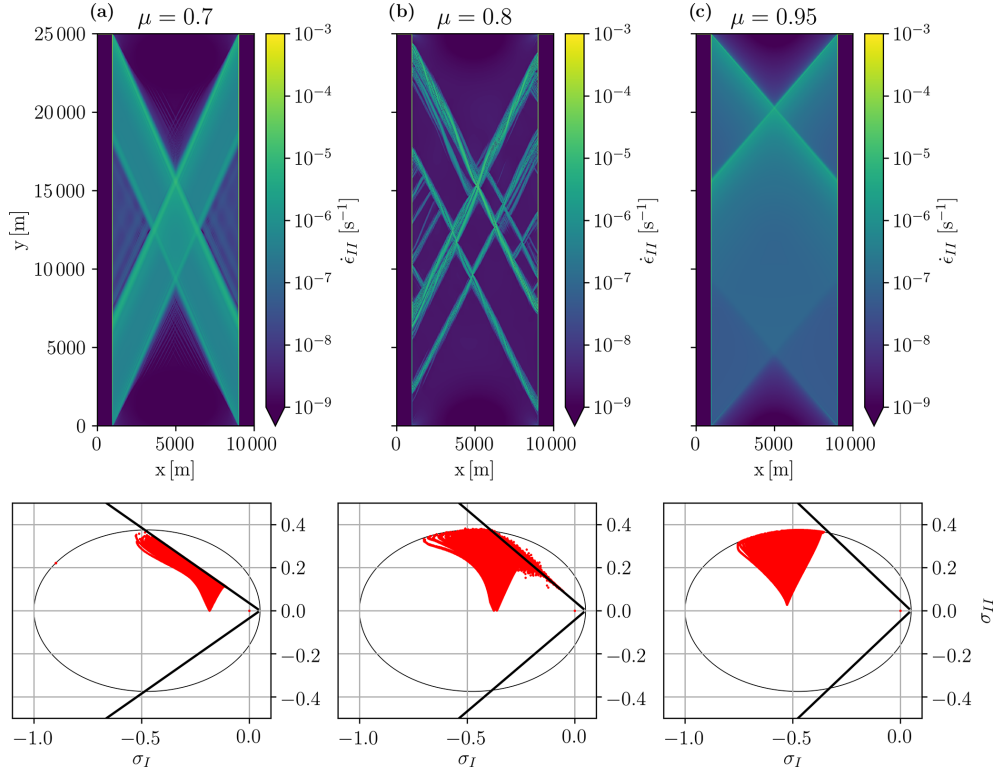


Figure 4.12: Maximum shear strain (top) and stress state in stress invariant space (bottom) for different internal angles of friction. **(a)** $\mu = 0.7$ or $\phi = 44^\circ$, **(b)** $\mu = 0.85$ or $\phi = 58^\circ$ and **(c)** $\mu = 0.95$ or $\phi = 72^\circ$ after 5 s of integration. The angles of fracture are $\theta = 23$, (28 ± 2) and 41° . Figure 4.10 illustrates how θ depends on μ for a Coulombic yield curve.

4.4 Discussion

Our idealized experiments using the VP rheologies resolve fracture lines as described by Hutchings et al. (2005) and akin to observations (Kwok, 2001). The fracturing of the ice floe creates smaller floes in a manner that appears realistic, for example, compared to Landsat-7 images (Schulson, 2004, Fig. 2). At the high resolution of 25 m the original interpretation of the continuity assumption, namely that each grid cell should represent a distribution of floes (Coon et al., 1974), is no longer valid, but we show that the fracture angle is independent of resolution and scale as expected. Instead, the emerging discontinuities and the polygonal diamond shape of the fracture lines that appear as floes spanning many grid cells are a consequence of the mathematical characteristics of the VP model (Pritchard, 1988). Diamond-shaped floes are observed in the Arctic Ocean (Erlingsson, 1988; Walter and Overland, 1993) and also modeled using a discrete element model (DEM) in an idealized experiment (Wilchinsky et al., 2010). The elastic anisotropic plastic (EAP) rheology assumes predominately diamond-shaped floes in sea ice (Wilchinsky and Feltham, 2006a). A sea ice model with EAP creates sharper fractures than a model with the elastic-viscous-plastic (EVP; Hunke and Dukowicz, 1997) rheology (Heorton et al., 2018). The authors concluded that the anisotropic model may improve the fracturing process for sea ice, especially by creating areas of oriented weaknesses, and particularly at coarse resolution where the fracture is not resolved by the grid spacing. In the experiments presented here, the VP rheologies lead to sharp and

anisotropic fracture lines without any additional assumptions.

We explored some experimental choices to separate their effects from those of the rheology parameters. The fracture angles do not depend on the spatial resolution and domain size as expected in our idealized numerical experiment setup (Sect. 4.3.2.1, Fig. 4.5). The maximum viscosities in the VP model are very high, and consequently, the VP model can be considered an ideal plastic material (i.e., a model with an elastic component that has an infinite elastic wave speed). For this reason, fracture in a VP model occurs almost instantaneously. Observed timescales of fracture are on the order of 10s for 60 m floe diameters (Dempsey et al., 2012, Fig. 6b), and from typical elastic wave speeds of 200–2000 m s⁻¹, large cracks of order 1000 km can form in minutes to hours (Marsan et al., 2012).

In our setup, the no-slip boundary condition has little effect on the fracture pattern, but our results suggest that in basin-wide simulations the choice of boundary conditions affects the fracture depending on the geometry and stress direction. The no-slip condition appears to be unphysical. It acts to concentrate the stress on the corners of the floe and forces the fracture to occur at this location. This should motivate a more thorough investigation of the boundary conditions for LKFs that form between one shoreline and another. Similar results were obtained from analytical solutions in idealized geometry for the Mohr–Coulomb yield curve with a double sliding deformation law (Sirven and Tremblay, 2014).

The confining pressure (i.e., thin ice imposed on the side of the domain) changes the distribution of stress within the domain. This results in different deformation patterns (shear and divergence) and different fracture angles because the yield curve is convex and uses a normal flow rule. From this we can conclude that by surrounding our floe with open water, we get the most acute angles from the rheology in this uni-axial compression setup. This is not consistent with the behavior of typical granular material for which an angle of fracture is independent of the confining pressure (Hutter and Rajagopal, 1994). Details of a heterogeneous ice cover also affect the fracture pattern. LKFs link the weaknesses in the ice cover, but the pattern still depends on the preferred fracture angles implied by the model rheology. In summary, we are confident that our choice of parameters allows us to isolate the effects of the rheology and the yield curve on the fracturing process.

In granular material, large shear resistance is linked to contact normals between floes that oppose the shear motion and lead to dilatation (Balendran and Nemat-Nasser, 1993). In our experiments, increasing shear strength in the standard VP model (reducing the ellipse aspect ratio e) does not decrease but increases the fracture angle. This is in contrast to the behavior of granular material where larger shear strength leads to lower fracture angles – think of a moist sand castle versus a dry sand castle. In addition, high shear strength in the VP model with the elliptical yield curve leads to convergence along the fracture plane, whereas observations (e.g., RADARSAT-derived deformation fields) show a range of positive and negative divergence along LKFs – in accordance with laboratory tests of granular material that show a variable internal angle of friction that depends on the distribution of the contact normals between individual floes (Hutter and Rajagopal, 1994). Inspection of the stress states in the 2-D stress plane suggests that the intersection of the yield curve with the σ_2 axis has an important role in the fracture process. This intersection point appears to determine the fracture angle. In fact, the angle is determined from the intersection of the Mohr’s circle of stress with the yield curve to give a theoretical relationship between the fracture angle and the ellipse ratio e . With our

experiments, we were able to confirm this relationship empirically.

Arctic-wide simulations improve metrics of sea ice concentration, thickness, and velocity by decreasing the value of e of the standard elliptical yield curve, that is, by adding shear and bi-axial tensile and compressive strength (Miller et al., 2005; Ungermann et al., 2017). The representation of sea ice arches improves with smaller e (Dumont et al., 2009), as do LKF statistics (Bouchat and Tremblay, 2017). Our results, however, show that this makes the fracture angles larger, which is in stark contrast to what we expect to be necessary to improve the creation of LKFs in sea ice models.

The fracture angle and the sea ice opening and ridging depending on the deformation states are consistent with the theory of the yield curve analysis developed in Pritchard (1988) and the Mohr’s circle framework that we present in Section 3.3. Interestingly, a change of ice maximum compressive strength P^* with a constant e has no influence on the LKF creation, although P^* is usually thought of as the principal parameter of sea ice models in climate simulations (e.g., Schmidt et al., 2014). The effects of bi-axial tensile strength T^* on fracture processes require further investigation, especially given the fact that the assumption of zero tensile strength is being challenged (Coon et al., 2007). The ice strength parameter C^* (the parameter governing the change of ice strength depending on ice concentration; Eq. 4.4) was not studied here, although it appears to be an important tuning parameter, and it also helps to improve basin-wide simulations (Ungermann et al., 2017). The simulations presented in this study are not realistic and cannot be compared directly to observations of ice floe fracture. For instance, our idealized ice floe is homogeneous, while sea ice is known to feature some weaknesses like thermal cracks or melt ponds.

With the Coulombic yield curve, the simulated fracture angle can be smaller than for the elliptical yield curve. For $\mu = 0.7$ ($\phi = 44^\circ$) theory predicts $\theta_{MC} = 22.8^\circ$ (Section 3.3). The simulated fracture angle with $\mu = 0.7$ of $\theta = 23.5^\circ$ is close to the $\simeq 20^\circ$ described in Hibler and Schulson (2000). Erlingsson (1988) developed a different Mohr–Coulomb theory linking the internal angle of friction and the fracture angle. This complex theory takes into account the fractal (or self-similar) nature of sea ice. It gives different results but is inadequate for a single ice floe simulated as presented here. Based on the results of Pritchard (1988), Wang (2007) used observed fracture patterns to design a curved diamond yield curve. But this yield curve also contains a non-differentiable point, which will be problematic for numerical reasons. The Coulombic yield curve used here uses a normal flow, and consequently divergence will always be present along shear lines. In situ measurements, however, show that the deformations follow a non-normal flow rule (Weiss et al., 2007), and large-scale observations show both divergence and convergence (ridges) along LKFs (Stern et al., 1995). There are alternative flow rules still to be explored, for example, a double-sliding law with (Ip et al., 1991) or without dilatation included (Balendran and Nemat-Nasser, 1993; Tremblay and Mysak, 1997).

4.5 Conclusions

Motivated by the observation that the intersection angles in a 2 km Arctic-wide simulation of sea ice are generally larger than in the RGPS dataset (Hutter et al., 2019), the fracturing of ice under compression was studied with two VP rheologies

in a highly idealized geometry and with very small grid spacing of 25 m. The main conclusions are given in the following.

In our experimental configuration with uni-axial compression, fracture angles below 30° are not possible in a VP model with an elliptical yield curve. Observations suggest much lower values. We find an empirical relationship between the fracture angle and the ellipse ratio e of the elliptical yield curve that can be fully explained by the convexity of the yield curve (Section 3.3). In contrast to expectations, increasing the maximum shear strength in the sea ice model increases the fracture angle. Along a fracture line, there can be both divergence and convergence depending on the shear strength of the ice, linked to the flow rule. The simulated ice opens and creates leads with an ellipse ratio $e > 1$ (shear strength is smaller than compressive strength) and ridges for $e < 1$ (shear strength is larger than compressive strength).

With a modified Coulombic yield curve, the fracture angle can be decreased to values expected from observations, but the non-differentiable corner points of this yield curve lead to numerical (convergence) issues and, for some values of the coefficient of internal friction μ , to fracture patterns that are difficult to interpret. At these corner points, two different slopes meet and give two non-unique solutions for fracture angles and deformation directions. We recommend avoiding non-differentiable yield curves (with a normal flow rule) in viscous-plastic sea ice models.

More generally, the model produces diamond-shaped fracture patterns. Later the ice floe disintegrates and several smaller floes develop. The fracturing process in the ice floe in our configuration is independent of the experiment resolution and scale but sensitive to boundary conditions (no-slip or free-slip). The fracture angle in the VP model is also sensitive to the confining pressure. This is not consistent with the notion of sea ice as a granular material. Unsurprisingly, the yield curve plays an important role in fracturing sea ice in a numerical model as it governs the deformation of the ice as a function of the applied stress.

The idealized experiment of a uni-dimensional compression is useful to explore the effects of the yield curve because all other parameters are controlled. Historically, the discrimination between the different yield curves was not possible because of the scarcity of sea ice drift data. Model comparisons to recent sea ice deformation datasets, such as from RADARSAT, imply that we would need to increase the shear strength with the ellipse in the standard VP rheology to match observations (Bouchat and Tremblay, 2017). We find that this increases the fracture angles, creating a dilemma. Therefore, the high-resolution idealized experiment presented in this work provides a framework to investigate and discriminate different rheologies – a yield curve and a flow rule.

If Arctic-wide sea ice simulations with a resolution of 25 m are not feasible today because of computational cost, we can still imagine small experiments being useful for process modeling on small scales when local and high-resolution observations (e.g., wind, ice velocities) are available. For example, such process modeling studies could be used to constrain the rheology with data from the upcoming MOSAiC campaign (Dethloff et al., 2016) that will provide a full year of sea ice observations in pack ice. Such simulations would also need to take into account the effects of heterogeneous ice cover and wind patterns, with potentially convergent and divergent wind forcing. Most climate models use the standard VP rheology (Stroeve et al., 2014) or one of its variants (e.g., EVP). Results presented here, however, imply that a more physical yield curve with a (possibly non-associative) flow rule is required.

Such a yield curve would have to be continuous in all representations, differentiable without corners, have some cohesion, and be consistent with available observations of fracture angles in convergent and divergent flow.

Chapter 5

Non-normal flow rules affect fracture angles in sea ice viscous-plastic rheologies

Note: The present chapter is a paper submitted to the journal *The Cryosphere* on June 8th 2020 (Ringeisen et al., 2020).

Authors Contributions: I designed the rheology and implemented the code changes with Martin Losch. I ran the experiments. I and Bruno Tremblay designed the theory linking sea ice rheologies and granular matter theory. I wrote the manuscript with contributions of Bruno Tremblay and Martin Losch.

Abstract

The standard viscous-plastic (VP) sea ice model with an elliptical yield curve and normal flow rule does not simulate fracture angles below 30° in uni-axial compression, in stark contrast with observations of Linear Kinematic Features (LKFs) in the Arctic Ocean. In this paper, we remove the normality constraint in the standard VP model and study its impact on the fracture angle in a simple uni-axial compressive loading test. To this end, we introduce a plastic potential independent of the yield curve that defines the post-fracture deformations or flow rule. The numerical experiments show that the fracture angle strongly depends on the flow rule details. For instance, a plastic potential with an ellipse aspect ratio smaller than that of the standard ellipse gives fracture angles that are as low as 22° . A newly adapted theory – based on one developed from observations of granular material – predicts numerical simulations of the fracture angles for plastic materials with a normal or non-normal flow rule with a root-mean-square error below 1.3° . Implementing an elliptical plastic potential in the standard VP sea ice model requires only minor modifications. The modified rheology, however, takes longer to solve numerically for a fixed level of numerical convergence. In conclusion, the use of a plastic potential addresses several issues with the standard VP rheology: the fracture angle can be reduced to values within the range of satellite observations and it can be decoupled from the exact shape of the yield curve. Furthermore, a different plastic potential function will be required to change the post-fracture deformation along the fracture lines (convergence or divergence) and to make the fracture angle independent on the confining pressure (as in observations).

5.1 Introduction

Sea ice plays a significant role in the energy budget of the climate system and therefore has a strong influence on future climate projections. Linear Kinematic Features (LKFs), narrow lines of deformation observed in the Arctic sea ice cover, emerge in high-resolution simulations (Kwok, 2001; Hutchings et al., 2005). LKFs in the Arctic sea ice cover influence the Earth system in many ways: heat and matter exchange take place primarily over open water (Badgley, 1965). Salt rejection during ice formation in leads creates dense water and influences the thermohaline circulation (Nguyen et al., 2011; Nguyen et al., 2012; Itkin et al., 2015). The ice strength locally depends on the ice thickness, which in turn is affected by sea ice fracture with thermodynamical growth in opening leads and with local dynamical growth during ridge formation.

In granular media like sea ice (Overland et al., 1998), deformation is localized along pairs of LKFs (Anderson, 1942; Erlingsson, 1988). Note, that in this study, we consider sea ice to be granular not only in the marginal ice zone, but also in pack ice, where ice floes are densely packed. The intersection angles between the LKFs influence the deformation field; thus, the local sea ice strength and the emergent sea ice anisotropy (Aksenov and Hibler, 2001). This anisotropy then influences future deformation and fracture line orientation, which will have impacts on the local sea ice mass balance. Therefore, reproducing the LKFs patterns, density, and orientation is important for accurate sea ice and climate projections at high-resolution.

LKFs have been studied for several decades using observations (Stern et al., 1995; Kwok, 2001; Schulson and Hibler, 2004; Weiss et al., 2007) and numerical models (Sprenn et al., 2017; Hutter et al., 2018). In viscous-plastic (VP) sea ice models, LKFs are created because the ice is modeled as a highly viscous material between narrow zones of plastic deformation (Hutchings et al., 2005). This behaviour has been argued to be the reason why temporal intermittency and spatial localization are low in VP models, leading to a spatial and temporal scaling of LKFs that is different from observations (Rampal et al., 2016). New models have been designed to represent sea ice fracture, for example, brittle models with a damage parameter that keeps the memory of previous fracture (Rampal et al., 2016; Dansereau et al., 2016), or anisotropic viscous-plastic rheologies models (Wilchinsky and Feltham, 2006b; Heorton et al., 2018). Still, as of today, the viscous-plastic rheology with elliptical yield curve and normal flow rule (Hibler, 1979) is the *de facto* standard rheology. For example, of the 33 Global Climate Models from the Climate Model Inter-comparison Project 5 (CMIP5), 30 use the standard VP rheology with an elliptical yield curve and normal flow rule (Stroeve et al., 2014).

Some of the criticised issues of the standard VP rheology have been addressed. For example, high-resolution VP models also reproduce observed intermittency and spatial localization, even without brittle fracture dynamics; and the origin of intermittency remains an open question (Bouchat and Tremblay, 2017; Hutter et al., 2018; Bouchat et al., 2020, submitted manuscript). However, the distribution of intersection angles between LKFs in the Radarsat Geophysical Processor System (RGPS) dataset and the standard sea ice VP model with an elliptical yield curve with ellipse ratio $e = 2$ (Hibler, 1979) do not agree (Hutter et al., 2019).

The orientation of LKFs has been the subject of many studies in the field of engineering and granular materials (called shear bands in this field). Two classical solutions coexist and set two limit angles for the orientation of fractures: the

Coulomb angle (static behaviour) and the Roscoe angle (dynamic behaviour). The Coulomb angle of fracture θ_C between the fracture line and the first principal stress is determined from the Mohr-Coulomb criterion. It is a function only of the internal angle of friction ϕ (Coulomb, 1773; Mohr, 1900):

$$\theta_C = \frac{\pi}{4} - \frac{\phi}{2}. \quad (5.1)$$

Roscoe (1970) challenged the coulombic theory by considering the case of dilatant material and found from experiments with sand that the dilatancy angle δ is the main parameter determining the orientation of shear bands (see Fig. 6 in Tremblay and Mysak, 1997, for a definition of the dilatancy angle δ in the context of sea ice modeling.). The Roscoe angle of fracture is

$$\theta_R = \frac{\pi}{4} - \frac{\delta}{2}. \quad (5.2)$$

A general theory derived from experiments with sand that takes into account both the angle of friction and the angle of dilation combines the Coulomb and Roscoe angles as (Arthur et al., 1977; Vardoulakis, 1980):

$$\theta_A = \frac{\pi}{4} - \frac{1}{4}(\phi + \delta). \quad (5.3)$$

Tremblay and Mysak (1997) used this general theory to design their sea ice rheology. Vermeer (1990) proposed a theoretical framework based the grain size and showed that the angle of fracture in most experiments lie between the two extremes: $\theta_C \leq \theta \leq \theta_R$, with $\delta < \phi$ in granular materials like sand. If $\phi = \delta$ then $\theta_R = \theta_C = \theta_A$, and the flow rule is normal to the yield curve. In other words, the principal axes of stress and the principal axes of strain are coaxial. This condition, however, is not generally satisfied for granular materials (Balendran and Nemat-Nasser, 1993). Experiments with sand have shown differences between ϕ and δ of the order of 30° (Vardoulakis and Graf, 1985; Bolton, 1986). Note that both mechanisms, friction and dilatancy, are not radically different: a larger dilatancy angle implies a larger grain size, more contact normals, hence more friction. Ringeisen et al. (2019) used the theory of the internal angle of friction with a normal flow rule in their appendix B to link fracture angles to rheology.

The fracture angles with the standard sea ice rheology cannot be smaller than 30° in uni-axial compression, even by changing the ellipse aspect ratio e (Ringeisen et al., 2019). This minimum angle is in conflict with observations that report fracture angles (half of the intersection angles) generally below 30° . Observations report fracture angles of 14° (Marko and Thomson, 1977), $15 \pm 1.5^\circ$ (Erlingsson, 1988), 17° to 18° (Cunningham et al., 1994), 24° ($\mu = 0.9$, Weiss and Schulson, 2009), and 20° to 25° (Hutter and Losch, 2020). Further, uni-axial compression experiments (Ringeisen et al., 2019) showed that: (1) the angle of fracture is a function of the gradient of shear strength to compressive strength set by the ellipse aspect ratio, (2) the ellipse aspect ratio determines the divergence along the LKFs, and (3) the fracture angle is a function of the confining pressure. These three properties of the standard VP rheology do not comply with the theory and observations of granular media behaviour, namely that shear band orientations and divergent/convergent motion at the slip lines are a function solely of the shear strength of the material

and orientation of the contact normals (or dilatation angle). This unphysical behaviour of the standard VP rheology is connected to the shape of the yield curve in conjunction with a normal flow rule.

The flow rule has the advantage that it can be observed with remote sensing methods, contrary to stress which need in-situ measurements. The ratio of shear and divergence along the LKFs allows to infer the dilatancy angle. Observations show that most of the deformation takes place in shear, with 98% of deformations showing more shear than divergence or convergence (Stern et al., 1995). The ellipse ratio of the standard model can be modified to fit this distribution (Bouchat and Tremblay, 2017). Also, laboratory experiments with first-year ice showed that flow rules are non-normal during brittle failures (Weiss et al., 2007). Separating the link between the fracture angle and the flow rule from the yield curve is necessary to design rheologies that are consistent with observed sea ice deformation.

This paper focuses on VP rheologies. Different models represent sea ice dynamics with different material properties, for example, Viscous-Plastic (VP, Hibler, 1977), Elastic-Plastic (EP, Coon et al., 1974), or Maxwell-Elasto-Brittle (MEB, Dansereau et al., 2016). In these different classes of models, various rheologies can be defined. In a VP rheology, a yield curve and plastic potential (flow rule) must be defined. The yield curve defines the stress criteria for the transition from small viscous deformations to large plastic deformations. The plastic potential determines the ensuing post-fracture deformation, called the flow rule. The flow rule is normal to the plastic potential (Drucker and Prager, 1952). The plastic potential can be set independently, or be equal to the yield curve. In the latter case, the flow rule is also perpendicular to the yield curve and is called a normal-flow rule or associated flow rule. Several yield curves have been used in sea ice models, some with a normal flow rule (Hibler, 1979; Zhang and Rothrock, 2005) and some with a non-normal flow rule (Ip et al., 1991; Tremblay and Mysak, 1997; Hibler and Schulson, 2000; Wang, 2007). It is important to note that two models with the same material properties sharing the same yield curve but with different flow rules are two different rheologies.

In this paper, we investigate the effects of a non-normal flow rule on fracture angles and present a generalized framework to use with viscous-plastic material with any flow rules (normal or non-normal). To this end, we introduce a plastic potential independent from yield curve. The new model is tested in simple uni-axial loading experiments where the relationship between fracture angle and flow-rule can be easily identified.

The paper is structured as follows. Section 5.2 describes the model (5.2.1), the new rheology (5.2.2), and a general theory linking the fracture angles and a general flow rule (5.2.3). The sections 5.3 and 5.4 describe the idealized experimental setup and the results. Section 5.5 discusses these results and their implication on current and future rheologies. Conclusions follow in section 5.6.

5.2 Sea ice Model and rheology

5.2.1 Building the sea ice VP constitutive equations

We consider sea ice as a 2D viscous-plastic material. The ice velocities are calculated from the sea ice momentum equations:

$$\rho h \frac{\partial \vec{u}}{\partial t} = -\rho h f \vec{k} \times \vec{u} + \vec{\tau}_a + \vec{\tau}_o - \rho h \nabla \phi(0) + \nabla \cdot \boldsymbol{\sigma}, \quad (5.4)$$

where ρ is the ice density, h is the grid cell averaged sea ice thickness, \vec{u} is the ice drift velocity field, f is the Coriolis parameter, \vec{k} is the vertical unit vector, $\vec{\tau}_a$ is the surface air stress, $\vec{\tau}_o$ is the ocean drag, $\nabla \phi(0)$ is acceleration from the gradient of sea surface height, and $\boldsymbol{\sigma}$ is the vertically integrated internal ice stress tensor defined by the sea ice VP constitutive equations. The constitutive equations link the stress tensor $\boldsymbol{\sigma}$ to the deformation tensor $\dot{\boldsymbol{\epsilon}}$ and the state variables χ (ice thickness, ice strength, ice concentration, etc.). The components of the strain rate tensor are computed from the velocities as $\dot{\epsilon}_{ij} = \frac{\partial u_i}{\partial x_j}$. The constitutive equations then have the form:

$$\boldsymbol{\sigma} = f(\dot{\boldsymbol{\epsilon}}, \chi). \quad (5.5)$$

In an ideal plastic model, the stresses are independent of the strain rates; in the VP model the stresses are independent of the strain rates for large deformation events (the plastic states with stresses on the yield curve) and they depend on the strain rates for small deformations (the viscous states with stresses inside the yield curve). It is this set of equations that defines the rheology of sea ice and determines the fracture pattern and the opening or closing along the fractures.

One of the state variables in the model is the maximal compressive strength P . This variable represents the maximal compressive stress that sea ice can bear in uniform compression before ridging. We use the simple standard relationship (Hibler, 1979):

$$P = P^* h e^{-C^*(1-A)}, \quad (5.6)$$

where C^* is a free parameter (typically $C^* = 20$), h is the mean ice thickness, A is the fractional sea ice area cover in a grid cell, and P^* is the ice strength of 1 m ice at 100% concentration ($A = 1$). Some other state variables are a function of P ; for instance, the tensile strength T is usually defined as $T = k_t \cdot P$, where the tensile factor $k_t > 0$ (König Beatty and Holland, 2010). Others are not, such as the ellipse aspect ratio (Hibler, 1979) or the internal angle of friction (Ip et al., 1991). The equation for the yield curve in a VP model is written in terms of the state variables.

For two-dimensional sea ice, stress is a rank two tensor; thus, it has four components. The yield curve represents the stress states that are deforming plastically while enclosing the states of stress for slow viscous deformations. We express the yield curve as a function of the stresses σ_{ij} and the state variables χ :

$$F(\sigma_{ij}, \chi) = 0. \quad (5.7)$$

The yield curve can be represented in principal stress (σ_1 and σ_2) or stress invariants space (σ_I and σ_{II}). Figure 5.1 shows an arbitrary yield curve in stress invariants space. Although equation (5.7) determines if the deformation is plastic or viscous,

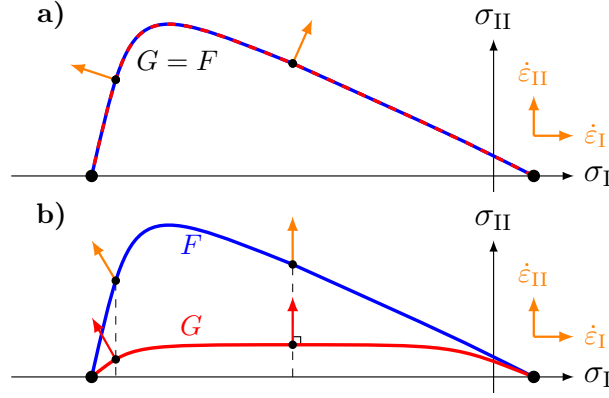


Figure 5.1: Schematic yield curve F (blue) and plastic potential G (red) for a normal (a) and non-normal (b) flow rule. The flow rule (orange) for a given stress on the yield curve is normal to the plastic potential (red) for the same σ_I . Note that the stress and strain invariant axes are assumed to coincide.

it does not determine how the ice will deform after fracture. In order to obtain a closed system of equations, we define a plastic potential that defines the flow rule.

The plastic potential determines the direction of deformation for stress states on the yield curve. Just as the yield curve, the plastic potential can be written as:

$$G(\sigma_{ij}, \chi) = 0. \quad (5.8)$$

The direction of the deformation, called the flow rule, is perpendicular to the plastic potential. This is shown in red on Fig. 5.1b and mathematically expressed by

$$\frac{\partial G}{\partial \sigma_{ij}}(\sigma_{ij}, \chi) = \lambda \dot{\epsilon}_{ij}, \quad (5.9)$$

where $\lambda > 0$ is the unknown flow rate. The flow rule is applied for stress states on the yield curve at the same compressive stresses (orange arrows in Fig. 5.1b). If the plastic potential and the yield curve are the same ($G = F$), the flow rule is called an *associative* or *normal* flow rule, as the flow rule is also perpendicular to the yield curve (see Fig. 5.1a).

Using Eq. (5.7) and Eq. (5.9), we can write a system of 5 equations (four from Eq. 5.9 and one from Eq. 5.7) for 5 unknowns (σ_{11} , σ_{22} , σ_{12} , σ_{12} , λ). Solving this system of equations allows us to write the constitutive equations for the sea ice model as function of the components of the strain-rate ($\dot{\epsilon}_{11}$, $\dot{\epsilon}_{22}$, $\dot{\epsilon}_{12}$, $\dot{\epsilon}_{21}$) and the state variables χ .

After deriving these constitutive equations, we assume that the stress and strain rate tensors are symmetric, that is, $\sigma_{12} = \sigma_{21}$ and $\dot{\epsilon}_{ij} = \frac{1}{2} \left(\frac{\partial u_i}{\partial x_j} + \frac{\partial u_j}{\partial x_i} \right)$. The symmetry follows from ignoring the rotation in an isotropic medium. Note that we first need to solve this system of equations without using the symmetry condition: the symmetry condition is only invoked at the end. Applying the symmetry before solving the system of equation changes the nature of the initial tensor, and the resulting constitutive equations would be different.

An ideal plastic model, with the stresses independent of the strain rates, has a singularity because the non-linear viscosities tend to infinity as the strain rates tend to zero. Hibler (1977) solved this issue with a regularization that limits the value

of the bulk and shear viscosities ζ and η to a maximum value. When the viscosities are capped to their maximum values, the stresses are linearly related to the strain rates and the material behaves as a viscous material.

5.2.2 Elliptical yield curve with non-normal flow rule

We now build a rheology with an elliptical yield curve and a non-normal flow rule, that is, we use a plastic potential G that is different from the yield curve F . We use a different, but still elliptical plastic potential for simplicity: this choice only requires only minor modifications to a typical VP sea ice model. We define the yield condition F and the plastic potential G as a function of the state variables χ : the ice compression strength P , the ice tensile strength $T = k_t P$ (König Beatty and Holland, 2010), the yield curve's ellipse ratio e_F , and the plastic potential's ellipse ratio e_G by

$$X(\sigma_I, P, e_X, k_t) = \left(\frac{\sigma_I + \frac{P(1-k_t)}{2}}{\frac{P(1+k_t)}{2}} \right)^2 + \left(\frac{\sigma_{II}}{\frac{P(1+k_t)}{2e_X}} \right)^2 - 1 = 0, \quad (5.10)$$

for $X = F, G$ for the yield curve or the plastic potential. Using Eq. (5.10), we write σ_{II} as a function of σ_I as:

$$\sigma_{II,X} = \frac{1}{e_X} \sqrt{P^2 k_t - \sigma_I^2 - \sigma_I P(1 - k_t)}. \quad (5.11)$$

Following Hibler (1977) and Hibler (1979), we derive the constitutive equations σ_{ij} :

$$\sigma_{ij} = 2\eta \dot{\epsilon}_{ij} + (\zeta - \eta) \dot{\epsilon}_{kk} \delta_{ij} - \frac{P(1 - k_t)}{2} \delta_{ij}, \quad (5.12)$$

where the shear and bulk viscosities η and ζ are defined by:

$$\zeta = \frac{P(1 + k_t)}{2\Delta} \text{ and } \eta = \frac{\zeta}{e_G^2} = \frac{P(1 + k_t)}{2e_G^2 \Delta} \quad (5.13)$$

with

$$\Delta = \sqrt{(\dot{\epsilon}_{11} - \dot{\epsilon}_{22})^2 + \frac{e_F^2}{e_G^4} ((\dot{\epsilon}_{11} - \dot{\epsilon}_{22})^2 + 4\dot{\epsilon}_{12}^2)}. \quad (5.14)$$

Figure 5.2 shows an example of yield curve and plastic potential, with the resulting flow rule. For $e_G > e_F$, the absolute value of the divergence is smaller and the shear strain rate is larger compared to a normal flow rule ($e_G = e_F$) and vice versa for $e_G < e_F$.

5.2.3 Linking fracture and flow rule

In this section, we generalize the theory linking the rheological model and the fracture angles in simple uni-axial compressive test (Ringelsen et al., 2019) to materials with a non-associated flow rule. To this end, we follow the theory of Roscoe (1970) where the angle of fracture depends uniquely on the angle of dilatancy of a granular material.

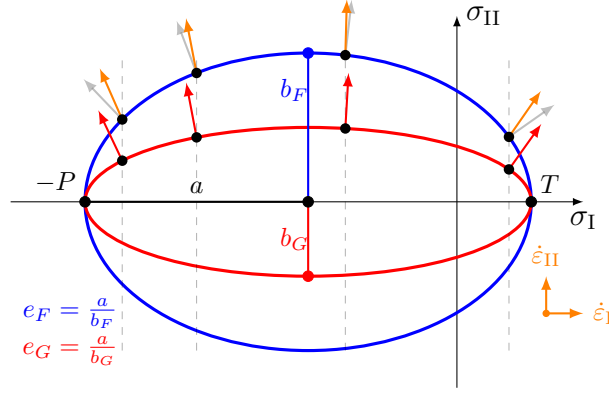


Figure 5.2: Elliptical yield curve with a non-normal flow rule, a yield curve ellipse aspect ratio $e_F = 2$ (blue) and a plastic potential ellipse aspect ratio $e_G = 4$ (red). The gray and orange arrows show the normal and non-normal flow rules, respectively.

Figure 5.3 illustrates the case of an arbitrary yield curve with an arbitrary plastic potential. The figure shows the geometrical construction that links the angle of dilatancy δ to the slope of the plastic potential $\tan(\gamma_G)$:

$$\sin(\delta) = \tan(\gamma_G) = -\frac{\partial\sigma_{II,G}}{\partial\sigma_I}. \quad (5.15)$$

Note that the minus sign above was included in the derivative of the yield curve in Eq. (B1) and (B2) of Ringeisen et al. (2019). This equation agrees with the definition of Roscoe (1970) $\sin(\delta) = \frac{\dot{\epsilon}_I}{\dot{\epsilon}_{II}}$, because the ratio of $\dot{\epsilon}_I$ to $\dot{\epsilon}_{II}$ is equal to the slope of the plastic potential $-\frac{\partial\sigma_{II,G}}{\partial\sigma_I}$, as the flow rule is perpendicular to the plastic potential. Figure 5.3 also shows the normal flow rule, which, in agreement with the coulombic theory, would lead to different fracture angles (light blue lines). From Fig. 5.3, the fracture angle can be written as:

$$\theta = \frac{\pi}{4} - \frac{\delta}{2}. \quad (5.16)$$

Substituting Eq. (5.15) in the equation above, the relationship between the fracture angle and the plastic potential becomes

$$\theta(\sigma_I) = \frac{1}{2} \left[\frac{\pi}{2} - \arcsin \left(-\frac{\partial\sigma_{II,G}}{\partial\sigma_I}(\sigma_I) \right) \right] = \frac{1}{2} \arccos \left(-\frac{\partial\sigma_{II,G}}{\partial\sigma_I}(\sigma_I) \right). \quad (5.17)$$

We calculate the fracture angles for the elliptical yield curve with non-normal flow rule in uni-axial compression along the y axis. In this case, $\sigma_{11} = \sigma_{12} = 0$, $\sigma_{22} < 0$, and the principal stresses and stress invariants can be written as:

$$\sigma_1 = \frac{1}{2} \left(\sigma_{11} + \sigma_{22} + \sqrt{(\sigma_{11} - \sigma_{22})^2 + 4\sigma_{12}^2} \right) = 0, \quad (5.18)$$

$$\sigma_2 = \frac{1}{2} \left(\sigma_{11} + \sigma_{22} - \sqrt{(\sigma_{11} - \sigma_{22})^2 + 4\sigma_{12}^2} \right) = \sigma_{22}. \quad (5.19)$$

$$\sigma_I = \frac{\sigma_1 + \sigma_2}{2} = \frac{\sigma_{22}}{2} \quad (5.20)$$

$$\sigma_{II} = \frac{\sigma_1 - \sigma_2}{2} = -\frac{\sigma_{22}}{2} = -\sigma_I. \quad (5.21)$$

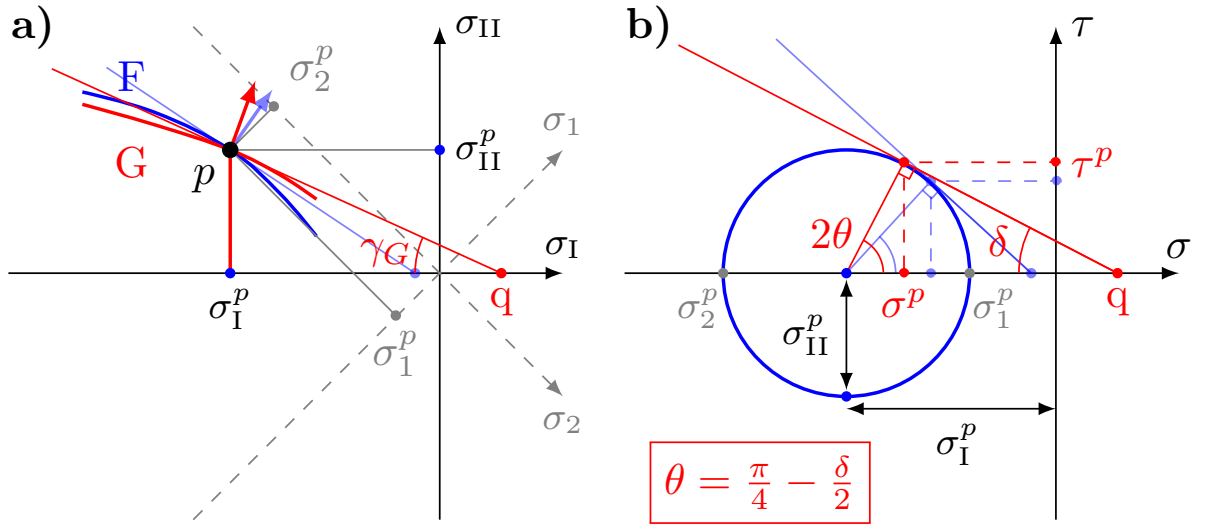


Figure 5.3: Link between fracture angle and the orientation of the flow rule: **a)** Arbitrary yield curve F (blue) and plastic potential G (red) in stress invariants space. The plastic potential and yield curve intersect at a stress state p for illustration purposes only. The orange arrow is perpendicular to G , but non-normal to the yield curve F . The tangent to the plastic potential G at point p has a slope $\mu_G = \tan(\gamma_G)$ and intersects the σ_I -axis at point q (thin red line). For reference, the normal and tangent to the yield curve F are shown as a thin blue arrow and line. Mohr's circle of stress for this stress state (blue) has a radius of σ_{II}^p and centers on σ_I^p on the σ_I axis. Gray dashed lines show the principal stress axes. **b)** Mohr's circle for the fracture state p in **a)** in the fracture plane of reference (σ, τ) of center σ_I^p and radius σ_{II}^p . The thin red line is the tangent to the Mohr's circle that passes through the point q on the σ axis. By this geometrical construction, $\sin(\delta) = \tan(\gamma_G) = \mu_G$ (for $|\mu_G| \leq 1$). δ is called the dilatancy angle. Again for comparison, the transparent blue lines show the corresponding construction for a normal flow rule from panel **a)**.

From Eq. 5.21, the maximum shear stress $\sigma_{II,F}^p$ in the fracture plane in uni-axial compression can be expressed as

$$\sigma_{II,F}^p(\sigma_I^p) = -\sigma_I^p, \quad (5.22)$$

where p indicates the stress state at the fracture. Figure 5.4 shows the stress trajectory in principal stress space for uni-axial compression. It also shows how the flow rule changes for the same stress state when using two different elliptical plastic potentials.

In the following, we use the normalized stress invariants $\sigma'_I = \frac{\sigma_I}{P}$ and $\sigma'_{II} = \frac{\sigma_{II}}{P}$ to simplify the notation. The slope of yield curve or the plastic potential depends only on e_F and e_G , but not on P . Substituting Eq. (5.11), σ'_I , and σ'_{II} in Eq. (5.22), we obtain,

$$\sigma'_{II}{}^p = -\sigma'_I{}^p = \frac{1}{e_F} \sqrt{k_t - \sigma'_I{}^p(\sigma'_I{}^p + 1 - k_t)}, \quad (5.23)$$

and solve the first stress invariant σ_I^p on the fracture plane in uni-axial compression

$$\sigma_I^p = \frac{(k_t - 1) - \sqrt{(1 - k_t)^2 + 4k_t(1 + e_F^2)}}{2(1 + e_F^2)}. \quad (5.24)$$

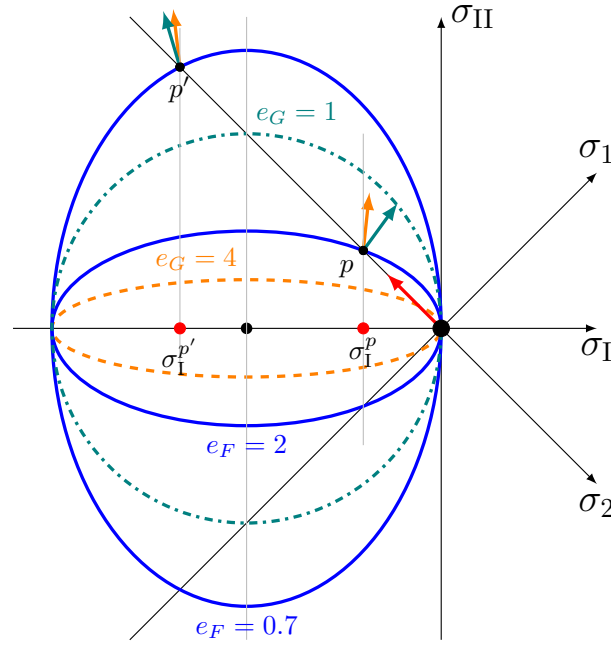


Figure 5.4: Trajectory of maximum normal stress (red arrow) in a uni-axial loading test experiment in a material with two different elliptical yield curves (blue) and plastic potentials (dashed orange and dash-dotted teal). The orange and teal arrows show the flow rule normal to the plastic potential of the same colour for the same stress state. For $e_G < e_F$, the ratio of divergence to shear increases. The opposite is true for $e_G > e_F$. A similar figure in principal stress space is presented in Ringeisen et al. (2019)

The slope of the tangent at σ_I^p to the plastic potential is given by the derivative of Eq. (5.11):

$$\frac{\partial \sigma'_{II,G}}{\partial \sigma'_I}(\sigma_I^p) = \frac{1}{2e_G} \frac{-2\sigma_I^p - 1 + k_t}{\sqrt{k_t - \sigma_I^p(\sigma_I^p + 1 - k_t)}}. \quad (5.25)$$

Substituting Eq. (5.24) into Eq. (5.25), yields

$$\left. \frac{\partial \sigma'_{II,G}}{\partial \sigma'_I} \right|_{\sigma_I^p} = \frac{1}{e_G e_F} \left(1 - \frac{(1 + e_F^2)}{1 + \sqrt{1 + 4 \frac{k_t}{(1-k_t)^2} (1 + e_F^2)}} \right). \quad (5.26)$$

or for zero tensile strength ($k_t = 0$),

$$\left. \frac{\partial \sigma'_{II,G}}{\partial \sigma'_I} \right|_{\sigma_I^p, k_t=0} = \frac{1}{2e_F e_G} (1 - e_F^2). \quad (5.27)$$

The fracture angle can finally be written as a function of e_G and e_F from Eq. (5.17):

$$\theta_{e,nn}(e_F, e_G) = \frac{1}{2} \arccos \left(\frac{1}{2e_F e_G} (e_F^2 - 1) \right). \quad (5.28)$$

As expected, for $e_F = e_G = e$ we recover the fracture angle derived in Ringeisen et al. (2019):

$$\theta_{e,n}(e) = \frac{1}{2} \arccos \left[\frac{1}{2} \left(1 - \frac{1}{e^2} \right) \right]. \quad (5.29)$$

5.3 Experimental setup and numerical scheme

Following Ringeisen et al. (2019), we load a rectangular ice floe of 8 km by 25 km with a thickness of $h = 1$ m and a sea ice concentration of $A = 1.0$ (see Fig. 5.5). The numerical domain has the dimensions $L_x = 10$ km and $L_y = 25$ km. At $y = 0$, we use a closed, solid boundary with a no slip condition (i.e., $u = v = 0$). At $x = 0$ and L_x , we use Neumann boundary conditions:

$$\left. \frac{\partial A}{\partial x} \right|_{x=0, L_x} = \left. \frac{\partial h}{\partial x} \right|_{x=0, L_x} = \left. \frac{\partial u}{\partial x} \right|_{x=0, L_x} = \left. \frac{\partial v}{\partial x} \right|_{x=0, L_x} = 0. \quad (5.30)$$

On the left and right sides of the domain ($x < 1$ km and $x > 9$ km), we have open water between the ice floe and the boundary to ensure that the boundaries have no effect on the simulation. At ($y = L_y$), we use a Dirichlet boundary condition for ice velocity (v the velocity in y -direction increasing linearly in time simulating an axial loading test) and a Neumann boundary condition for ice thickness and concentration :

$$v(t)|_{y=L_y} = a_v \cdot t, \quad u(t)|_{y=L_y} = 0; \quad \left. \frac{\partial A}{\partial y} \right|_{y=L_y} = \left. \frac{\partial h}{\partial y} \right|_{y=L_y} = 0 \quad (5.31)$$

with $a_v = -5 \cdot 10^{-4} \text{ m s}^{-2}$. The grid spacing of the domain is 25 m, and the timestep is 0.1 s.

The non-linear momentum equations are integrated using a Picard solver with 15 000 non-linear (or outer-loop) iterations (Losch et al., 2010). For the linearized problem within each iteration, we use a line successive (over-)relaxation (LSR) method (Zhang and Hibler, 1997), with a tolerance criterion of $|u_k - u_{k-1}|_{\max} < 10^{-11} \text{ m s}^{-1}$, where k is the linear iteration index. We use an inexact approach with only a maximum of 200 linear iterations for the linearized equations; the linearized system does not reach the tolerance criterion for the first non-linear iterations, but does so as the non-linear system approaches a converged solution. We chose a very small tolerance and residual norm for the solution of the linear and non-linear problem in order to simulate a clean fracture with a well defined fracture angle - for comparison with theory and observations. These criteria are much stricter than common recommendations for Arctic sea ice simulations (e.g. Lemieux and Tremblay, 2009). We expect modeling sea ice with a non-normal flow rule to be more challenging than with a normal flow rule. The non-coaxiality of the deviatoric stress and strain rate introduces more complexity because Drucker's postulate for stability is not respected (Vermeer and De Borst, 1984; Balendran and Nemat-Nasser, 1993). This particular uni-axial loading experiment is also complex to solve numerically because the forcing is localized on the boundary, in contrast to real geophysical system integrations where wind and ocean currents are acting over the entire surface of the ice.

The intersection angles between the LKFs are measured with the *Measure Tool* from the GNU Image Manipulation Program (GIMP, version 2.8.16, gimp.org). The first 5 seconds of simulations are used to define the sea ice fracture and calculate the fracture angle. The angle of each fracture lines is measured and used to compute the average fracture angle and the standard deviation $\sigma = \sqrt{\text{VAR}}$. Note that the fracture angles do not depend on resolution, scale, geometry, or boundary conditions (see Ringeisen et al., 2019, their Sec. 3.2). We do not use a replacement pressure

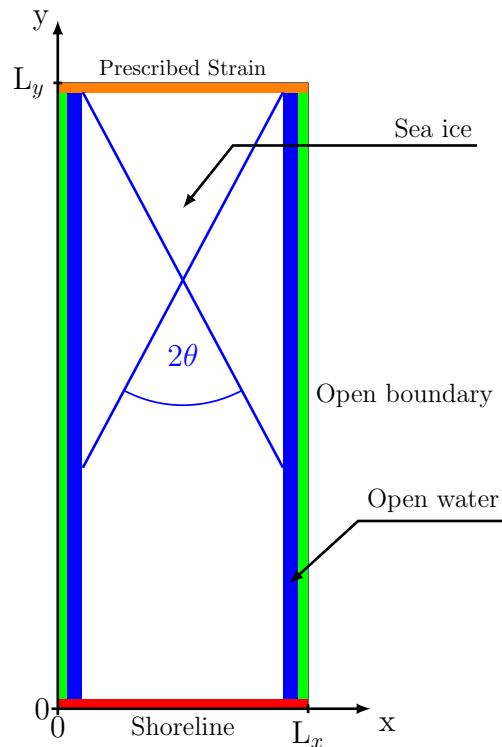


Figure 5.5: Model domain with a solid wall at $y = 0$ (red), Dirichlet boundary conditions with $\vec{u} = 0$ at $y = 0$ and prescribed velocities at $y = L_y$. Open boundaries at $x = 0, L_x$ (green) with Neumann boundary conditions. For the conservation of mass, ice thickness and concentration equations (h, A) Neumann boundary conditions are used on all boundaries. θ is the measured fracture angle with respect to the vertical; the blue line represents an LKF.

scheme (Ip et al., 1991; Ip, 1993), because it has no influence with the angle of fracture (not shown).

5.4 Results

We study the evolution of the fracture angle θ when the plastic potential changes while the yield curve stays the same (see Fig. 5.4 for details). In this manner, the ice breaks for the exact same stress state but with a different flow rule. For simplicity, we test here the elliptical yield curve without tensile strength ($k_t = 0$).

Figure 5.6 shows the fracture pattern for the standard yield curve ellipse ratio $e_F = 2.0$ and three values of the plastic potential ellipse ratio $e_G = 1.4, 2.0,$ and 4.0 . Following observations and laboratory experiment, the ice fractures have a diamond shape pattern (Erlingsson, 1988; Wilchinsky et al., 2010). With a normal flow rule ($e_G = 2.0$), single pairs of fracture lines with one unique fracture angle, large deformation along the LKFs, and smaller deformations (by several orders of magnitude) within diamond-shape floes are simulated. With the non-normal flow rule ($e_G = 1.4$ and $e_G = 4$) we make three observations:

1. Asymmetric secondary fracture lines appear, in contrast to the normal flow rule simulation. We attribute the asymmetry and presence of secondary frac-

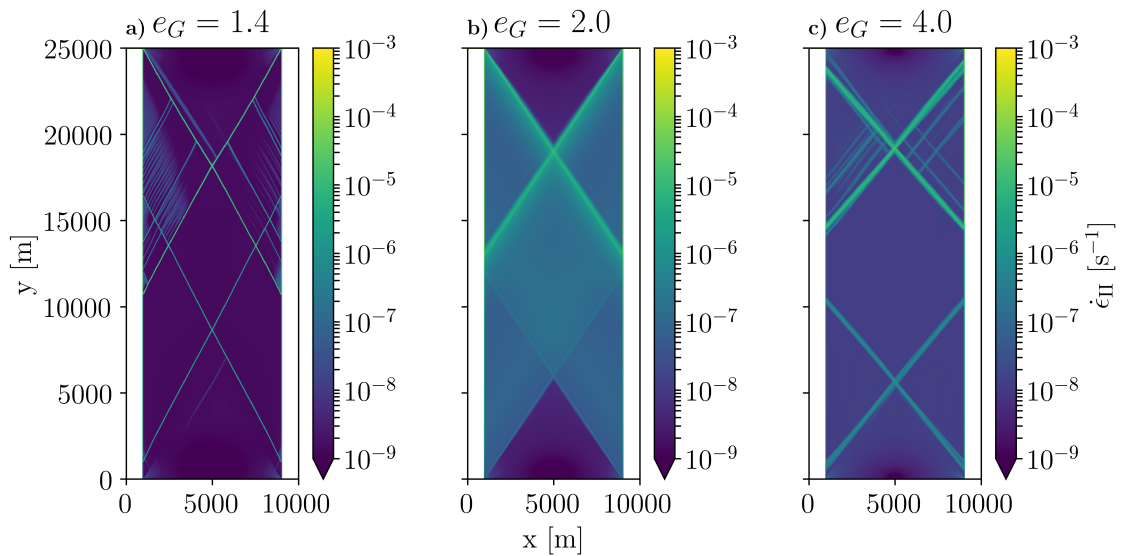


Figure 5.6: Diamond-shaped fracture pattern for $e_F = 2.0$ and three different values of e_G after five seconds of simulation. For the non-normal flow rule (panels a and c), there are primary and secondary fracture lines, in contrast to the normal flow rule (panel b) where single pair of fracture lines are simulated. The fracture angles are $29.92 \pm 1.28^\circ$ for $e_G = 1.4$, $34.3 \pm 0.25^\circ$ for $e_G = 2.0$, and $40.7 \pm 0.94^\circ$ for $e_G = 4.0$. The error corresponds to two standard deviation (2σ) of the measured fracture angles.

tures to the lack of full numerical convergence associated with the violation of Drucker’s principle, or the non-normality of the flow rule (the ratio of divergence to shear strain rate differs from that of the shear to normal stress). For instance, the grid-cell average residual norm (R) decreases by four orders of magnitude for the normal flow rule compared with two orders of magnitude for the non-normal flow rule for the same number of non-linear iterations (15 000); specifically to $R = 8 \times 10^{-4}$ for $e_G = e_F = 2$ to $R = 6 \times 10^{-2}$ for $e_G = 1.4$ and $e_F = 2$. Note that a Jacobian-free Newton-Krylov (JFNK) solver with a quadratic local numerical convergence does not perform better because the global convergence is poor with a combination of localized forcing and high grid resolution (Losch et al., 2014; Williams et al., 2017).

2. The width and activity of the LKFs is also affected by the flow rule. With $e_G = 1.4$, the lines are thinner, the shear along the LKFs is smaller and there is little shear between the fracture lines. With $e_G = 4.0$, the fracture lines are broader, the shear along the LKFs is higher and there is more shear between the fracture lines. With $e_G = 1.4$ the flow rule at the fracture is mainly in divergence, while for $e_G = 4.0$, the flow rule is mainly in shear and there is more stress transmitted to the ice in between the fracture lines.
3. The fracture angle changes as the plastic potential changes. The angles are wider with $e_G = 4$ than $e_G = 1.4$. The effect of flow rule orientation on the fracture angles is discussed below.

We now present results from four sets of simulations with fixed yield curve ellipse ratios at $e_F = 0.7, 1.0, 2.0, 4.0$. For each of these, we test the sensitivity of the

results to changes in the plastic potential ellipse ratio e_G . The choice of yield curve ellipse ratios e_F are: the standard value of (Hibler, 1979), values suggested by Bouchat and Tremblay (2017) and Dumont et al. (2009), and an extreme value resulting in a very small shear strength and smaller fracture angles.

Figure 5.7a shows how the fracture angles evolve as the plastic potential ellipse ratio e_G changes for each of the four values of e_F . There is a clear dependence of the fracture angles on the relative eccentricity of the plastic potential and yield curve. For $e_G > e_F$, the shear strain rate increases along the LKFs and the fracture angle tend toward 45° as e_G increases, in agreement with the theory (Eq. 5.17). For $e_G < e_F$, the flow rule implies more divergence (for $e_F > 1$, or convergence for $e_F < 1$) and less shear along the LKFs, and the fracture angles move away from 45° as e_G decreases. More generally, for $e_F < 1$, the fracture angle increases with increasing convergence along the LKFs as e_G decreases. For $e_F > 1$, the fracture angle decreases with increasing divergence as e_G becomes smaller. For $e_F = 1$ (a circular yield curve), the fracture angles are independent of e_G because the fracture takes place at the peak of the yield curve and the flow rule is not affected by changes of the plastic potential ellipse ratio (e_G).

The coloured dashed lines in Fig. 5.7 show the fracture angles $\theta_{e,nn}(e_F, e_G)$ predicted by Eq. (5.28). The coefficient of determination R^2 and the root-mean-square error (RMSE) between the simulated angle of fracture and theoretical predictions are 0.974 and 0.37° for $e_F = 0.7$, 0.953 and 1.22° for $e_F = 2.0$, and 0.968 and 0.47° for $e_F = 4.0$. The RMSE is 0.37° for $e_F = 1.0$, R^2 being inapplicable. That is, the theory predicts the fracture angles accurately. This result shows that the flow rule plays a major part in the simulated fracture angle for a given rheology. The black dashed line show the evolution of the fracture angle with a normal flow rule ($e_G = e_F$, Eq. (5.29)).

For completeness, Figure 5.7b also show the theoretical predictions for a constant plastic potential ellipse ratio e_G as the yield curve ellipse ratio e_F changes. The modeled angles for $e_G = 4.0$ are shown as an example. The fracture angles become smaller as the e_F increase. Yield curve ellipse ratio smaller than $e_F = 1$ do not create fracture angles below 45° .

5.5 Discussion

The idealized experiments using the elliptical yield curve with a non-normal flow rule show that the type of deformation and the fracture angle are intimately linked with the shape of plastic potential. We observe that a yield curve ellipse ratio $e_F < 1$ does not allow for fracture angles smaller than 45° in uni-axial compression when using an elliptical plastic potential, irrespective of the plastic potential elliptical aspect ratio. To reduce the fracture angles with yield curve ellipse ratios $e_F > 1$, one needs to use plastic potential ellipse ratios e_G smaller than the yield curve ellipse ratio, that is, $e_G < e_F$. The numerical experiments show that the use of a plastic potential in a viscous-plastic model allows separating the yield criterion from the resulting deformation (flow rule). This allows to decouple the mechanical strength properties of the material (ice) from its post-fracture behaviour. The results illustrate clearly how the yield curve defines the stress for which the ice will deform, that is, the transition between viscous and plastic deformation, and how the relative shape of the plastic potential with respect to the yield curve defines both the type of deformation

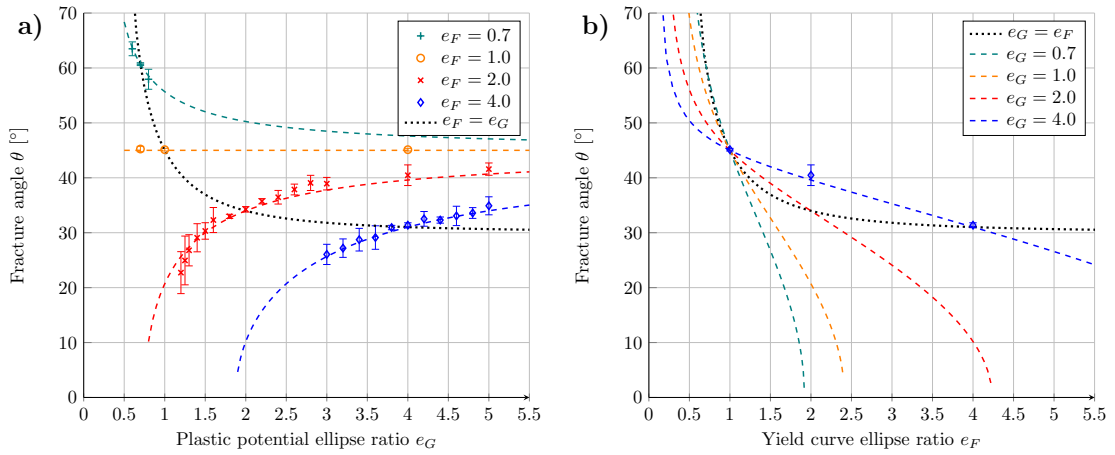


Figure 5.7: **a)** Fracture angles as function of the plastic potential ellipse ratio e_G for different yield curve ellipse ratios ($e_F = 0.7, 1.0, 2.0$, and 4.0). The markers with ranges are the mean and variation (2σ) of the fracture angles. The dashed lines show the prediction from the theory (Eq. 5.28). The R^2 between theory and modeled angles for $e_F = 0.7, 2.0$, and 4.0 are $0.97, 0.95$, and 0.97 . **b)** Theoretical predictions of the fracture angle as function of e_F with a constant e_G . The black dotted line for the normal flow rule ($e_F = e_G$), is indicated for reference.

(convergence or shear) along the fracture line and the fracture angle. The resulting fracture angles are in excellent agreement with the Roscoe angle predictions (Roscoe, 1970).

Understanding the link between rheology and fracture angle is necessary for choosing or designing a rheology that is capable of reproducing the observed angle of intersection between LKFs and consequently the emerging anisotropy. In principle, it may be possible to solve several inconsistencies of the standard elliptical yield curve with a normal flow rule Ringeisen et al. (discussed in 2019) by using a plastic potential that is independent of the yield curve, namely:

1. In the standard VP model with elliptical yield curve and normal flow rule, adding shear strength increases the fracture angle, contrary to granular matter theory (Coulomb, 1773). This behaviour is linked to the shape of the elliptical yield curve. In principle, we can decrease the fracture angle with increasing shear strength (e_F decreasing) by decreasing e_G , but only if $e_F > 1$. When doing this, the flow rule becomes very non-normal, making the numerical convergence difficult.
2. The angle of fracture in the standard VP model changes with confining pressure unlike laboratory experiments with granular materials (e.g. sand) where the fracture angle is relatively insensitive to the confining pressure (Alshibli and Sture, 2000). This behaviour cannot be eliminated with an elliptical plastic potential, as the normal stresses along the LKFs increases with confining pressure and the flow rule changes from divergence to convergence. A different plastic potential function would change this behaviour. However, this would make the model implementation and numerical convergence more difficult. However, we note that a 3D granular material like sand cannot release

stress by ridging as sea ice does. A 2D material, such as sea ice, can ridge and “escape to the 3rd dimension” after fracture.

3. In the standard VP model with a normal flow rule, the divergence and convergence are set by the ellipse ratio of the yield curve, and thus by the relative amounts of compressive and shear stress. The plastic potential ellipse ratio e_G changes the flow rule but does not change the sign of the divergence along the LKFs which is solely determined by the yield curve ellipse ratio e_F . With the elliptical plastic potential, convergent motion remains convergent and only the ratio of shear to convergence changes. To change this behaviour, a different shape of plastic potential is required, for example a teardrop plastic potential.
4. The fracture angles in the standard VP models are larger than observed. Using a non-normal flow rule allows us to change the fracture angle in uni-axial compression to values below 30° ; something that is not possible with a normal flow rule (Ringeisen et al., 2019).

Other yield curves have been used in previous studies; for instance, the Mohr–Coulomb, the Coulombic yield curve, or the teardrop yield curves. The use of a plastic potential in conjunction with these yield curves may also prove useful in solving these issues. A detailed analysis of the simulations using the family of Mohr–Coulomb and Teardrop yield curves is beyond the scope of this work and will be presented in a subsequent study. Below, we apply knowledge gained from the simulations presented above, and discuss how alternative yield curves may address deficiencies in the standard VP rheology.

It is possible to include different (non-normal) flow rules with the Mohr–Coulomb family of yield curve. The Mohr–Coulomb yield curve with a pure shear flow rule (Ip et al., 1991) would create fracture angle approximately equal to 45° , independently of the slope of the yield curve. It corresponds to the case $e_G \gg e_F$, hence $\delta \simeq 0$ and $\theta = 45^\circ$, as shown in Fig. 5.7). This contradicts the Coulomb angle theory, which predicts an angle of fracture that depends solely on the internal angle of friction (Eq. 5.1). Including an angle of dilatancy with a Mohr–Coulomb yield curve (Tremblay and Mysak, 1997) would allow for different angles of fracture with shear and divergence or convergence along the LKFs depending on δ . Such fracture angle and divergence would be independent of the shear strength and the confining pressure in agreement with Roscoe’s angle of fracture. Such a rheology could potentially solve the all four issues. It is also important to note that the Mohr–Coulomb yield curves do not satisfy the convexity requirements of Drucker’s postulate of stability. Mohr–Coulomb yield curves in plastic earth mantle models showed different fracture angles corresponding to the Coulomb angle, Roscoe angle, and the intermediate Arthur angles (Buiter et al., 2006; Kaus, 2010; Mancktelow, 2006). However, such geological models are usually incompressible, and making inferences for the compressible formulation of sea ice models is difficult. The investigation of the fracture angles with Mohr–Coulomb yield curves is left for future work.

The Coulombic yield curve uses the two straight limbs from the Mohr–Coulomb yield curve and an elliptical cap of the standard VP rheology for large compressive stresses (Hibler and Schulson, 2000). In this rheology, the flow rule over the two straight limbs is defined by the elliptical yield curve; that is, the ellipse serves as a plastic potential for the Mohr–Coulomb yield curve. The Coulombic yield curve leads to unrealistic and asymmetrical fracture lines $i)$ when the stress states lie at

the non-differentiable intersection between the straight limbs and the elliptical cap (Ringeisen et al., 2019), and *ii*) when the stress states lie on the two straight limbs with the non-normal flow rule. Note that straight and symmetric fracture lines in this rheology are only possible when all the stress states are located on the Mohr–Coulomb limbs and the flow rule at the fracture line is near-normal, that is, at the location where the normal to the ellipse plastic potential is nearly perpendicular to the limbs of the Mohr–Coulomb yield curve (Ringeisen et al., 2019).

The teardrop yield curve with a normal flow rule (Rothrock, 1975a; Zhang and Rothrock, 2005) is divergent for a wide range of normal stresses and for all practical purposes consists of a continuously differentiable version of the Coulombic yield curve. This asymmetry between divergent and convergent deformation for different normal stresses decreases the effect of confinement on the fracture angle – issue 2 – and reduces the fracture angle for any confinement pressure – issue 4. This yield curve does not address issue 1, because adding shear strength in the tear-drop yield curve also increases the fracture angle.

The main disadvantage of a non-normal flow rule is the slower numerical convergence. Solving the momentum equation accurately requires more solver iterations and failure to converge is more frequent than for standard normal-flow-rule rheologies. In our simulations, this numerical issue manifests itself by the presence of multiple and asymmetrical fracture lines despite the fact that our experiments are entirely symmetrical. The fracture lines with a normal flow rule are symmetrical and come in pairs (Ringeisen et al., 2019). The poorer numerical convergence in practice will go unnoticed in high-resolution simulations using realistic geometries, since the number of iterations typically used ($O(10)$) is much smaller than that required for full convergence. On the upside, at each time-step, a new iteration typically use the solution from the previous timestep as initial conditions. This, together with slowly varying forcing in space and time, the number of solver iterations per forcing cycle is large, in contrast to the fast changing forcing in this study. Whether this behaviour (asymmetry and multiple fracture lines) will also be present in realistic simulation using spatially and temporally varying wind forcing remains to be tested.

The following criteria should be considered when building a new rheology. The spatial and temporal scaling of sea-ice deformation should agree with observations (Bouchat and Tremblay, 2017; Hutter et al., 2018); the flow rule should reproduce the correct divergence along LKFs (Stern et al., 1995); the yield curve includes some tensile strength (Coon et al., 2007) and reproduces observed distributions of internal stress when ice deforms (Weiss and Schulson, 2009); the distribution of fracture angles should agree with observations (Marko and Thomson, 1977; Erlingsson, 1988; Cunningham et al., 1994; Hutter et al., 2019); the sea ice mechanical strength properties (yield curve) and deformation (flow rule) should vary in time and space depending on the time-varying distribution of the contact normals and floe size distributions, as per observations and laboratory or numerical experiments (Overland et al., 1998; Hutter et al., 2019; Horvat and Tziperman, 2017; Roach et al., 2018; Balendran and Nemat-Nasser, 1993; Dansereau et al., 2016).

Although high spatial resolution observations from satellite are available from optical instruments (e.g., from the Landsat or Sentinel programs), higher temporal resolution of sea ice deformation and flow size distributions are still lacking. So is the combined knowledge of the failure stresses and their associated deformation of sea ice as a 2D granular material. Sea ice floating on the ocean surface can “escape” vertically when ridging under confined compression (Hopkins, 1994). This

behaviour differs from laboratory test that use axial symmetry and general knowledge about 3D granular material like sand. Generally, information about sea ice resistance in different configurations (e.g., confinement) and the resulting fracture angles and deformation (ridging or opening) is also still missing, although laboratory scale experimental results are available Weiss et al. (2007), Schulson et al. (2006), and Weiss and Schulson (2009). The sea ice flow size distribution varies in time (summer/winter) and space (marginal ice zone/central Arctic) (Rothrock and Thorndike, 1984). These variations change the mechanical properties (e.g., distribution of contact normals) and thermodynamic properties (e.g., lateral melt) of sea ice (Horvat and Tziperman, 2017). Consolidated observations of these two physical processes are needed to design new rheologies for high-resolution climate modelling.

5.6 Conclusions

The flow rule, which dictates the post-fracture deformation, has a fundamental effect on the orientation of fractures lines in a viscous-plastic sea ice model. To test this, we added an elliptical plastic potential (allowing for a non-normal flow rule) to the standard viscous plastic rheology with an elliptical yield curve. We tested this new rheology with numerical experiments in uni-axial compression using the standard viscous-plastic model of Hibler (1979). The modeled fracture angles are in agreement with the Roscoe angle, a theory based on experiments with granular materials that includes an angle of dilatancy (Roscoe, 1970; Tremblay and Mysak, 1997). This new rheology partially solves issues raised in an earlier study (Ringeisen et al., 2019). The use of a plastic potential or non-normal flow rule allows for the simulations of smaller fracture angles between pairs of Linear Kinematic Features, in agreement with satellite observations. The fracture angles, however, still depend on the confinement pressure, and the elliptical plastic potential does not modify the direction of deformation at the fracture lines (convergence or divergence), only the ratio of divergence relative to shear. The momentum equations for a rheological model with a non-normal flow rule are more difficult to solve numerically, and produce multiple lines of fractures that are asymmetrical (despite symmetry of the problem), in contrast with a model with a normal flow rule. Understanding the effect of the flow rule on the fracture angle is necessary to design VP rheologies for high-resolution sea-ice modeling that both reproduce fracture angles and deformation along the fracture lines, and the behaviour of sea ice as a granular material.

Designing a rheology for high-resolution simulation requires information on sea ice fracture angles and sea ice strength in a wide range of stress conditions (i.e., compression with or without confinement, pure shear, tension), yet unavailable at high temporal and spatial resolution. The observations of the Multidisciplinary drifting Observatory for the Study of Arctic Climate (MOSAIC, Dethloff et al., 2016) in 2019/2020 may provide valuable data from continuous ice radar imaging, stress sensors, and arrays of drift buoys that will greatly help improve sea ice model dynamics.

Chapter 6

Fracture angles with alternative VP rheologies

The tuaq [shorefast ice] used to be very thick, and it froze a long distance from shore. Nowadays our ocean doesn't freeze far from shore, and our tuaq and rivers become unsuitable for hunting because they are too thin and dangerous. And last year, we really couldn't go out seal hunting [in Kongiganak and Kwigillingok] because the shorefast ice was too thin.

— *SIKU: Knowing Our Ice: Documenting Inuit Sea Ice Knowledge and Use (Krupnik et al., 2010)*

— *John PHILLIP, comments collected in October 2005 in Kongiganak*

Chapter 4 and Chapter 5 described the link between VP rheologies with elliptical yield curves and the fracture angles using idealized experiments. In this chapter, I complete these work by testing the remaining sea ice VP rheologies presented in Chapter 2. I compare the modeled fracture angles with the predictions from theory of the internal angle of friction (Coulomb angle), with predictions from the angle of dilatancy (Roscoe angle), and with the combined solution, which includes both theories, called the Arthur angle.

6.1 Experimental setup

To be consistent, I use the same experimental setup as in Chapter 4 and Chapter 5. Again, I use the MIT general circulation model (MITgcm, Marshall et al., 1997; Losch et al., 2010), and implemented the alternative rheologies in its sea ice package. The model parameters are listed on Table 6.1.

6.2 Alternative rheologies

6.2.1 Mohr–Coulomb yield curve with shear flow rule

6.2.1.1 MCS rheology

In this section, I test the Mohr–Coulomb yield curve with shear flow rule as described in Section 2.2.3. I refer to this rheology as the MCS rheology. This rheology is special because it uses a semi-plastic flow rule for stress states on the yield curve with $\sigma_I \in] - P, k_t P[$.

Table 6.1: Model parameters for the idealized compression experiment

Symbol	Definition	Value	Unit
ρ	Density of ice	910	kg m^{-3}
P^*	Ice strength	27.5	kN m^{-1}
C	Strength reduction parameter	20	
Δ_{min}	Maximum Viscosity	10^{-10}	s^{-1}
C_w	Water drag coefficient	5.21×10^{-3}	
N_x, N_y	Size of the domain	400×1000	
$\Delta x, \Delta y$	Grid spacing	25	m
L_x, L_y	Size of experiment	10×25	km
l_x, l_y	Ice floe's size	8×25	km
A	Initial ice concentration	100	%
h	Initial ice thickness	1.0	m
N_{lin}	Nbr. linear iteration	200	
N_{nlin}	Nbr. nonlinear iteration	15000	
ϵ_{err}	Max. error in LSR	10^{-11}	m s^{-1}
dt	Timestep	0.1	s
a_v	Acceleration of prescribed velocity	$5 \cdot 10^{-4}$	m s^{-2}

With the MCS rheology, the fracture patterns visible in the shear and divergence have multiple asymmetric fractures (Figure 6.1). The fractures are very wide with complex structures. These structures look similar to the one observed with the Coulombic yield curve on Figure 4.12. The small variations of the fracture angles with μ will be investigated in Section 6.2.1.3.

Figure 6.2 shows the stress states corresponding to the simulations in Figure 6.1 with the yield envelope. A large number of stress states are outside the yield curve. This is an indication of bad numerical convergence. The convergence gets better as μ becomes smaller. The residuals of the solver for these simulations are 1.61×10^1 , 4.72×10^1 , and 8.45×10^1 for $\mu = 0.6, 0.7,$ and 0.8 , respectively.

6.2.1.2 MCE rheology

As an alternative to the MCS rheology, I proposed in Section 2.2.4 a Mohr–Coulomb yield curve with an elliptical plastic potential (referred to as the MCE rheology) inspired by the Coulombic yield curve (Hibler and Schulson, 2000). It has the advantage of a plastic flow rule in both shear and divergence, like the elliptical yield curve. The orientation of the flow rule changes with the ellipse ratio of the plastic potential. This behavior can be used to create the Mohr–Coulomb yield curve with a quasi-shear flow rule.

To create such an flow rule, I increase the ellipse ratio to $e = 50$. The ellipse becomes very thin and all flow rule vectors are approximately aligned with the shear direction (Figure 6.3). The MCE rheology with $e = 50$ is referred to by the acronym MCES.

Figure 6.4 shows the shear and divergence deformation after 5 s of simulation with the MCES rheology for three values of the slope parameter $\mu = 0.6, 0.7,$ and 0.8 and with an tensile factor $k_t = 0.1$. The fracture is better defined than with the half-plastic flow rule in MCS, with only a few thin fracture lines. The divergence is

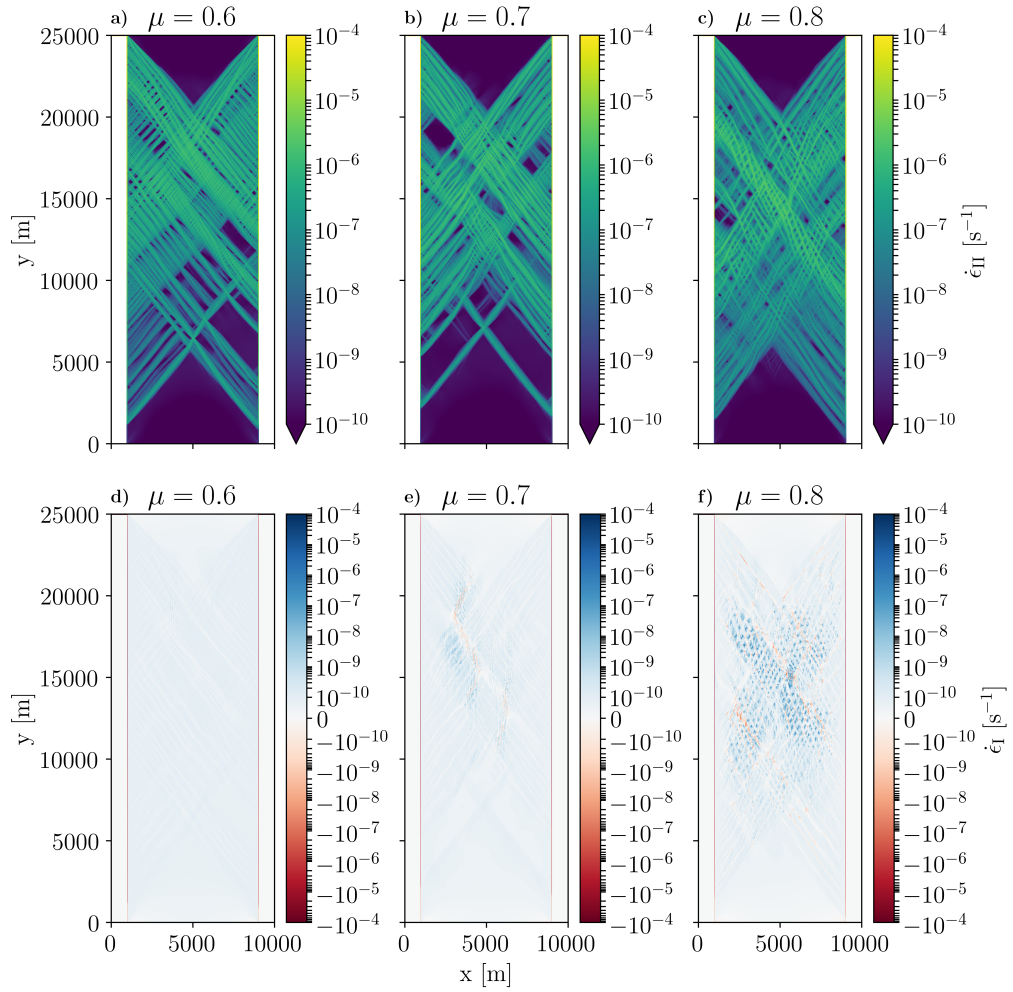


Figure 6.1: Shear $\dot{\epsilon}_{II}$ (top) and divergence $\dot{\epsilon}_I$ (bottom) strain rates after 5 s of simulation with the MCS rheology with three values of the slope parameter μ . The fracture lines are very broad with a complex structure. The divergence is negligible and only emerges for $\mu = 0.8$ when the solution has not converged.

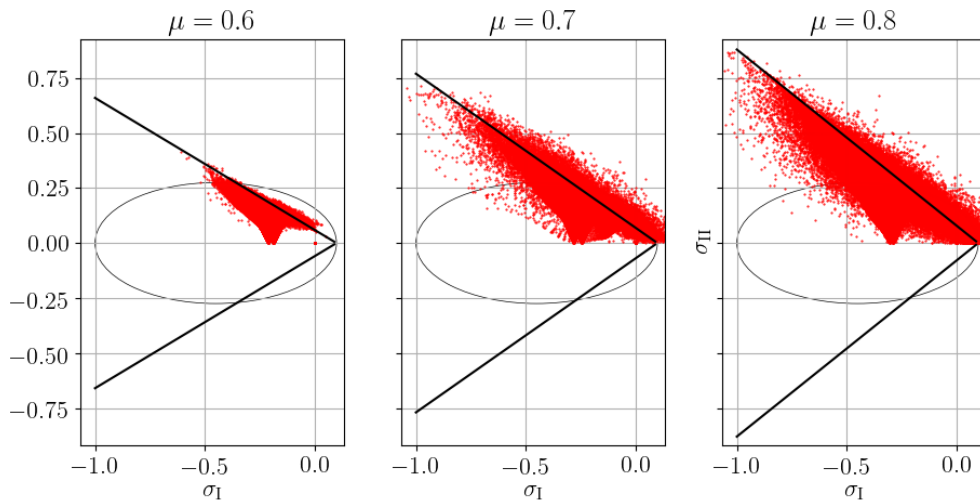


Figure 6.2: Stress states after 5 s of simulation for three values of the yield curve slope parameters $\mu = 0.6, 0.7,$ and 0.8 , with the MCS rheology.

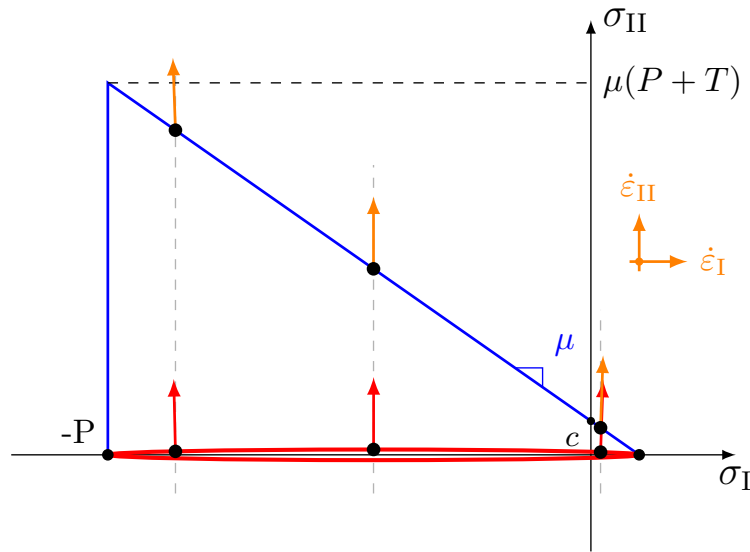


Figure 6.3: Schematics of the MCE yield curve with a plastic potential ellipse ratio $e = 50$. The flow rule is perpendicular to the plastic potential and oriented almost exclusively in shear, with very little divergence (positive $\dot{\epsilon}_I$) or convergence (negative $\dot{\epsilon}_{II}$).

non-zero, because with the MCEs flow rule there is a small amount of divergence or convergence.

Figure 6.5 shows the stress states corresponding to the simulations on Figure 6.4. More stress states are inside the yield curves than for the MCS rheology, a sign of better numerical convergence. The residuals of these simulations are 0.177×10^1 , 0.218×10^1 , and 1.81×10^1 for $\mu = 0.6$, 0.7 , and 0.8 , respectively. That is, the convergence is improved by one to two orders of magnitude compared to the MCS rheology.

6.2.1.3 Fracture angle as function of μ

I now investigate the relationship between the fracture angles and the slope parameter μ with MCS and MCEs rheologies. Despite the chaotic fracture pattern (Figure 6.1), an average fracture angle of the multiple fracture lines as a function of the slope parameter μ can be measured (Figure 6.6 1.7) and compared to the theoretical values of the Coulomb angle ($\theta_{MCS,n}$), Roscoe angle ($\theta_{MCS,nn}$), and Arthur angle

$$\theta_A = \frac{1}{2} (\theta_{MCS,nn} + \theta_{MCS,n}), \quad (6.1)$$

as defined in Chapter 3. The measured angles of the simulations are similar for both rheologies, but the angles from the MCEs rheology are systematically smaller and closer to the Arthur angles. The simulated angles are large, and do not agree with observed fracture angles.

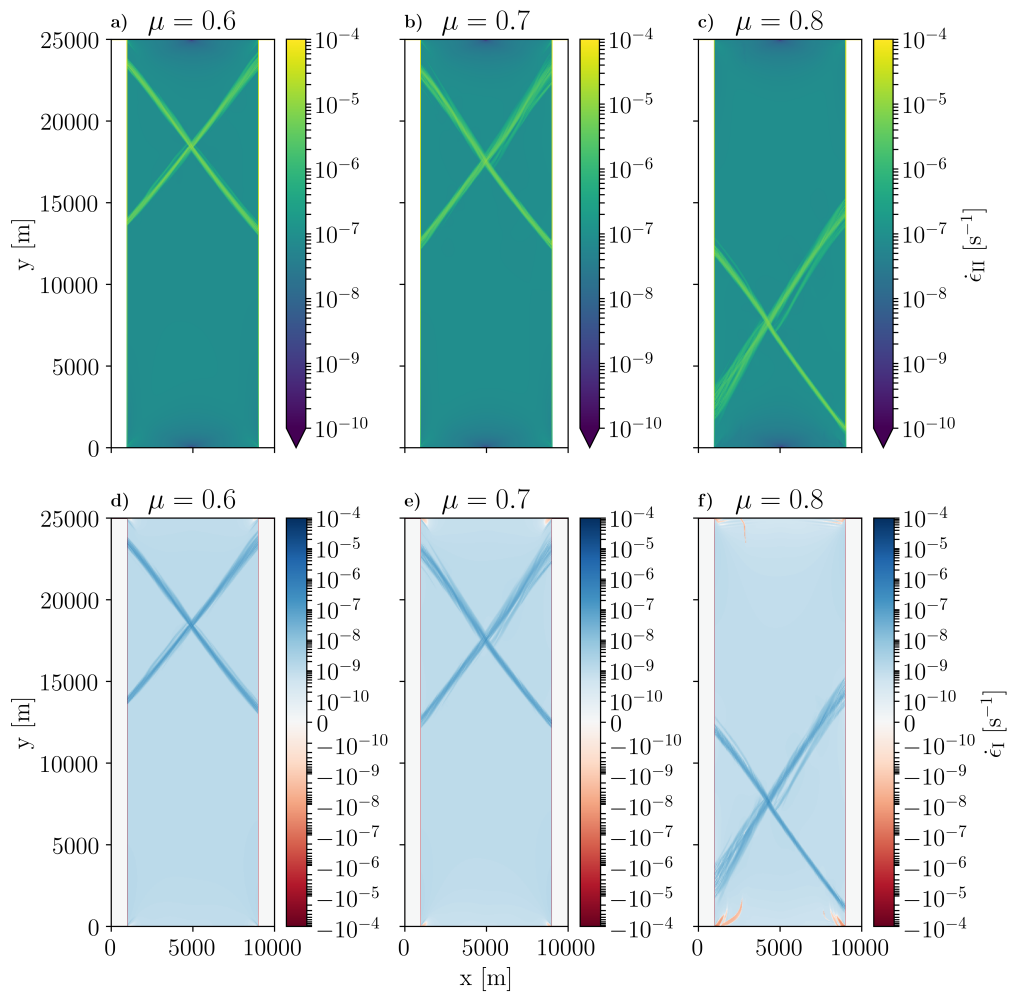


Figure 6.4: Shear ($\dot{\epsilon}_{II}$, top) and divergence ($\dot{\epsilon}_I$, bottom) strain rate after 5 s of simulation with the MCES rheology with $k_t = 0.1$ for three values of the Mohr-Coulomb slope parameter μ .

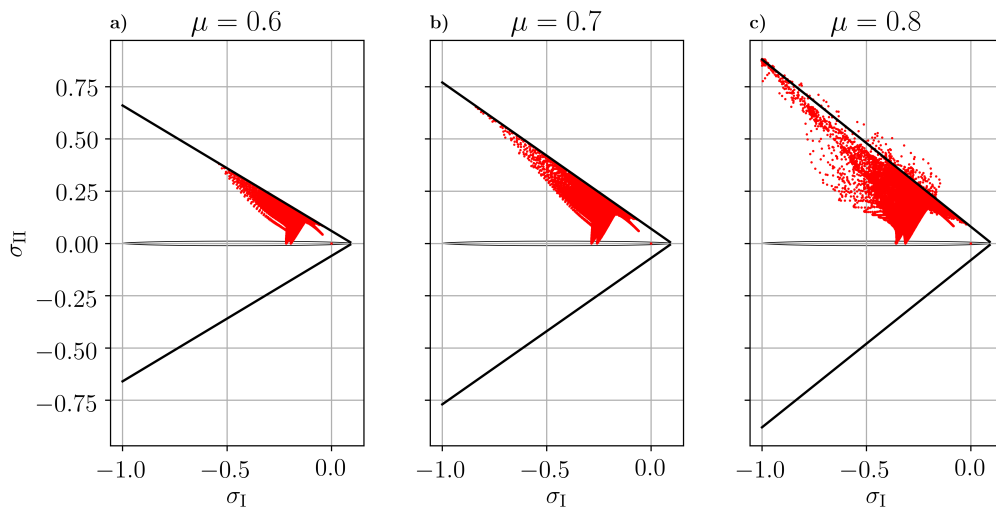


Figure 6.5: Stress states after 5 s of simulation for three values of the yield curve slope parameters $\mu = 0.6$, 0.7 , and 0.8 , with the MCES rheology.

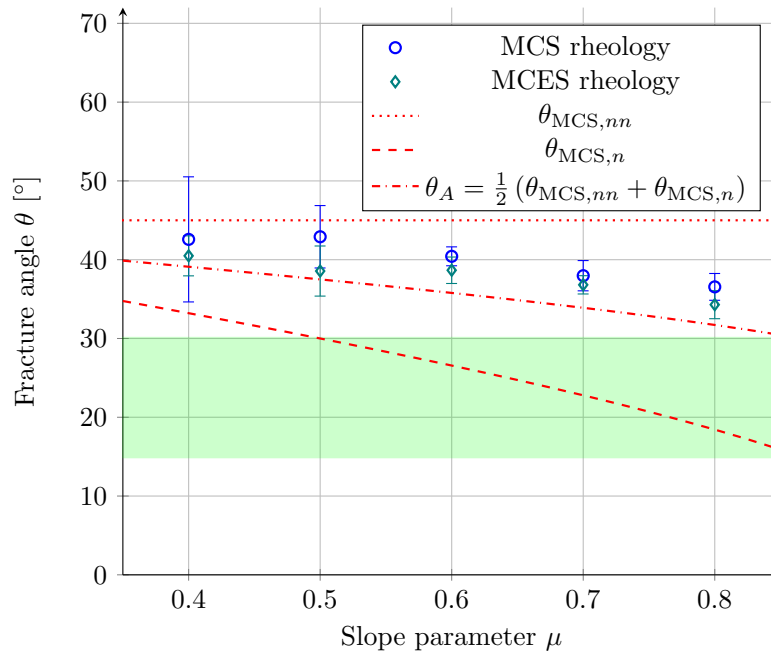


Figure 6.6: Simulated fracture angle as a function of the slope parameter μ for the MCS rheology and the MCES rheology. The ranges are the 2σ deviations of the modeled angles. The Arthur angles θ_A are a better prediction of the modeled angles than Coulomb angles ($\theta_{\text{MCS},n}$) or the Roscoe angles ($\theta_{\text{MCS},nn}$). The shaded green area on the graph shows the range of fracture angle in Arctic observations.

6.2.2 Mohr–Coulomb yield curve with elliptical plastic potential (MCE rheology)

In the previous Section 6.2.1, I tested the Mohr–Coulomb yield curve with an elliptical plastic potential, but only with a quasi-shear flow rule. Here, I extend the study of this rheology for different flow rule settings. In a first step, the yield curve is kept constant (i.e., the slope parameter μ is constant) and I study the effect of changing the orientation of the flow rule (i.e., by changing e). In a second step, the plastic potential is kept constant (i.e., e is constant), and I change the yield curve slope parameter μ . For all the experiments, a tensile strength factor of 5% ($k_t = 0.05$) is used.

Figure 6.7 shows the modeled fracture angles as a function of the plastic potential ellipse ratio e for a constant slope parameter $\mu = 0.7$. The fracture angles change with the flow rule orientation in contradiction with the coulombic theory of the internal angle of friction which does not account for the orientation of flow rule but only the slope of the yield curve. However, the angles do not follow the predictions given by the Roscoe angles either. The simulated angle agree best with the Arthur angle θ_A (Equation 6.1), although even the Arthur angle underestimates the fracture angles slightly. For $e \approx 1.35$, the flow rule is normal (the point where all three predictions are the same), the simulations develop clear fracture lines with a very small variation range.

Figures 6.8 show the modeled fracture angles as function of the slope parameter μ for a constant value of the ellipse ratio e . I chose two values for the plastic potential ellipse ratio: $e = 1.4$ and $e_G = 4.0$. For both series of experiments, the

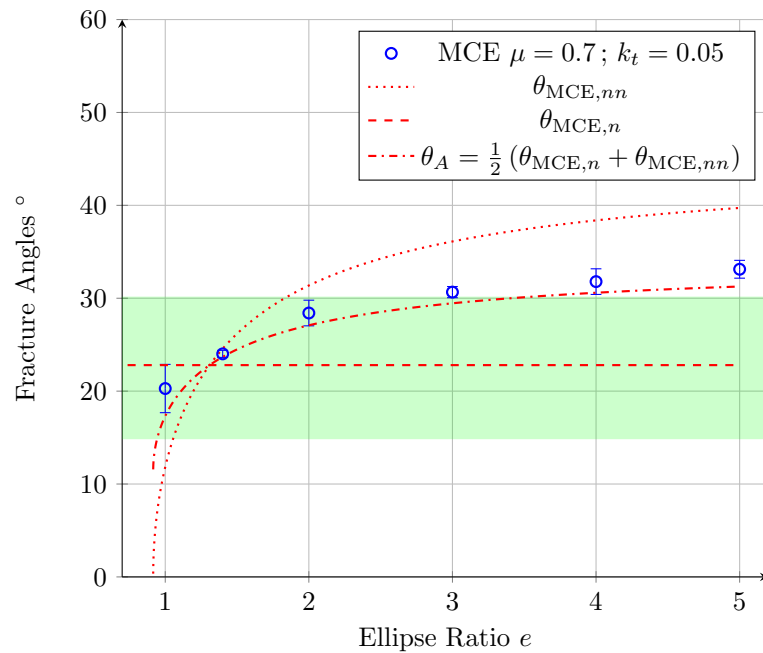


Figure 6.7: Average fracture angles as function of the plastic potential ellipse ratio e , in blue, with the theoretical predictions, in red. The ranges show the 2σ deviation. With a normal flow rule, at the intersection of the predictions, the variations are minimal. The shaded green area on the graph shows the range of fracture angles in Arctic observations.

modeled angles show a good agreement with the Arthur angles. The fracture angles are influenced by both the yield curve shape and the flow rule direction. As for Figure 6.7, and for both values of e , the Arthur's angle prediction underestimate the angles slightly. With $e = 1.4$, no fracture angles are shown for $\mu = 0.3$ and $\mu = 0.4$ because there is no clear fracture pattern. For these two cases, note that no angles could be derived from Roscoe angle predictions, because the absolute value of the slope of the plastic potential is greater than 1. It appear to be necessary that both Coulomb and Roscoe angle are defined to create a fracture line.

6.2.3 Teardrop and Parabolic Lens rheologies

In this section, I study the angle of fracture with the Teardrop and Parabolic Lens yield curve with normal flow rules, referred to as the TD and PL rheologies (Zhang and Rothrock, 2005). I use my modifications described in Section 2.2.6 and 2.2.7.

I investigate the dependence of the fracture angles on the tensile factor k_t , which is the only parameter in the TD and PL rheologies. First, the fracture the fracture lines form a diamond for both rheologies, as observed with the other yield curves (Figure 6.9). Note that without the modifications, no fracture pattern could be obtained (not shown).

The angle of fracture increases with k_t , in agreement with the theoretical predictions (Figure 6.10). The flow rule is normal so that all the predictions are equal. For the TD rheology, the RMS error and the R^2 number between the modeled angles and the predictions are 0.458° and 0.992. For the PL rheology, the RMS error is 0.24° , and the R^2 is 0.998. For values of k_t below 0.05, the fracture angles are small

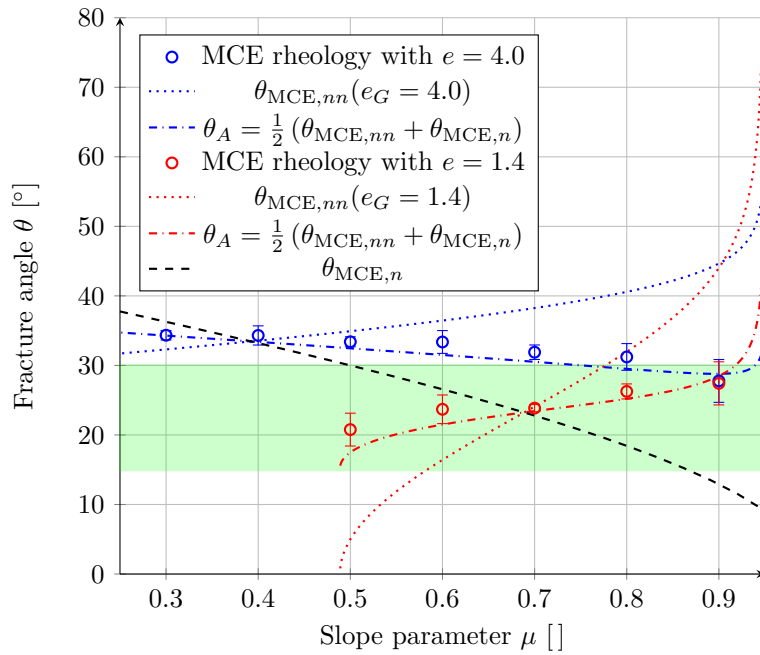


Figure 6.8: Average fracture angles as function of the yield curve slope μ for $e = 1.4$ (red) and $e = 4.0$ (blue). The theoretical predictions of the Roscoe angles and the Arthur angles are shown in the corresponding color. The predictions from the Coulomb angle are the same for both cases and are shown in black. The error ranges are the 2σ deviation of the measure angles. With a normal flow rule, at the intersection of the predictions, the angles variations are minimal. The shaded green area on the graph shows the range of fracture angles in observations.

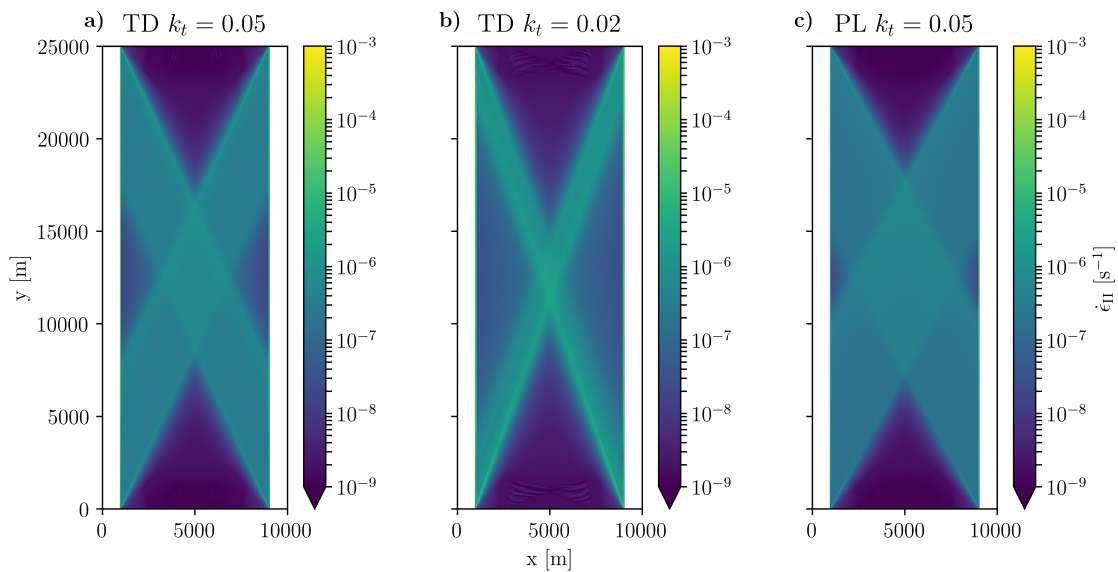


Figure 6.9: Shear strain rate $\dot{\epsilon}_{II}$ after 5 seconds with the Teardrop (TD, panels a and b) and Parabolic Lens (PL, panel c) rheologies.

and below 30° . For the same value of k_t , the fracture angles of the parabolic lens rheology are always larger than with the teardrop rheology.

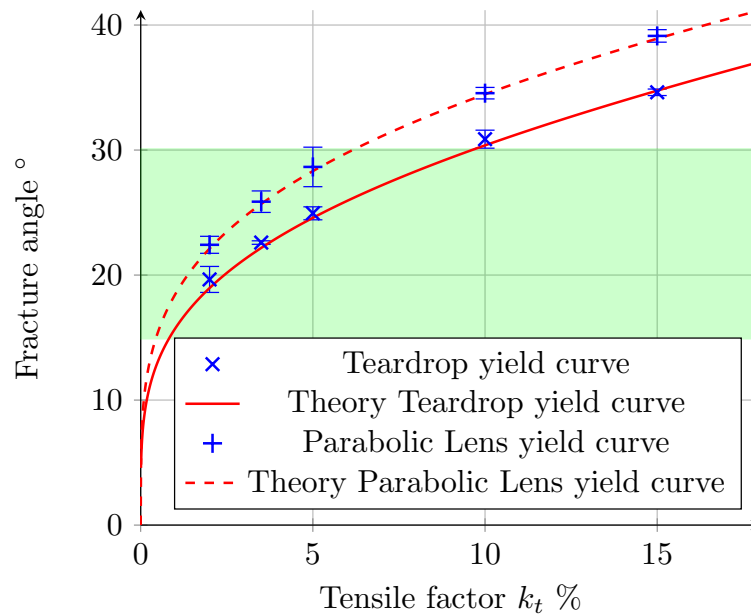


Figure 6.10: Fracture angles for the Teardrop and the Parabolic Lens yield curve. The error ranges correspond to 2σ deviations. The shaded green area on the graph shows the range of fracture angles in observations.

6.3 Discussion

6.3.1 Mohr-Coulomb yield curves

The flow rule has to be fully plastic to ensure numerical convergence and the creation of narrow fracture lines. I have compared two formulations of a Mohr–Coulomb yield curve with a shear flow rule: The first rheology (MCS) has a plastic flow rule in shear and a viscous flow rule for convergent and divergent motion (see Section 2.2.3). The second rheology (MCES) has a flow rule defined by an elliptical plastic potential, thus the flow rule is plastic in both shear and convergent motion (Section 2.2.4). Results show that the differences in formulation have a strong impact on the numerical convergence in favor of the MCES rheology. The MCES rheology has fewer fracture lines that are also narrower and more symmetric. The stress states are mostly inside the yield curve, in strong contrast with the MCS rheology. The residuals of the numerical solver for the MCES rheology are reduced by one order of magnitude compared to the MCS rheology. Even for the MCES rheology, the fracture angles vary considerably: the flow rule is non-normal so the convergence is more difficult to achieve, as described in Chapter 5. A downside of the MCES rheology is that while it approximates a pure shear flow rule, the deformation in convergence and divergence is still non-zero. Finally, both shear-only rheologies have similar fracture angles, which corresponds best to the Arthur angles (Arthur et al., 1977; Vardoulakis and Graf, 1985).

The fracture angles with the Mohr–Coulomb yield curve with elliptical plastic potential (MCE) also follow the Arthur angles (Arthur et al., 1977; Vermeer, 1990). In three series of simulations with various slope parameters μ and plastic potential ellipse ratio e_G , the modeled fracture angles are influenced by both the slope of the yield curve and the orientation of the flow rule. This combined theory can be called a macroscopic angle of friction that results from the equal and joint influence of a microscopic angle of friction and an angle of dilatancy (Balendran and Nemat-Nasser, 1993; Tremblay and Mysak, 1997). This finding disagree with the results of Chapter 5, where the orientation of the flow rule alone predicted the fracture angles, following the Roscoe angle (Roscoe, 1970). The origin of difference between these two rheologies is still unclear. I speculate about several explanations:

- The difference may come from the method used to build the constitutive equations for Mohr–Coulomb rheologies. Contrary to the rheologies with elliptical yield curves, the shape of the yield curve is not set by solving the constitutive equations, but by enforcing a modified expression for the shear viscosity η a-posteriori.
- With the Mohr–Coulomb yield curves, the ratio of shear and normal stress is not unique. All grid cells that deform plastically have the same stress ratio, given by slope of the yield curve μ . This non-uniqueness of the stress could modify the propagation of stress between the grid cells and affect the angle of fracture.
- With the same argument of non-uniqueness, note that the Mohr–Coulomb yield curves do not satisfy the convexity condition of Drucker’s postulate of stability (Drucker and Prager, 1952; Kelly, 2020).

For these reasons, investigating a rheology and its expected fracture angle in idealized experiments provides valuable of insight.

Using an MCE rheology can reduce the angles of fracture of conjugate faults in sea ice models below the 30° threshold of the standard rheology. With $\mu \in [0.6, 0.8]$ (Schulson, 2004; Weiss and Schulson, 2009), this is achieved by having a plastic potential ellipse ratio $e_G \in [1.2, 2]$. Having an very small ellipse ratio ($e < 1.0$) is counter-productive, as the area of the yield curve where fracture can create reduces. As shown with the Mohr’s circle in Chapter 3, a fracture can be only created if the slope of the yield curve and the plastic potential are inside the range $[-1, 1]$. We observe this behavior in Figure 6.8, where no fracture pattern could be found for $\mu < 0.5$.

The MCE rheology appears as a suitable candidate for high resolution sea ice modeling with realistic fracture patterns. It has a well defined flow rule, that includes divergent behavior for open-water creation, convergent behavior for ridge creation, and the range in between, as observed (Stern et al., 1995; Bouchat and Tremblay, 2017). In Chapter 4, I have shown that the standard rheology, the elliptical yield curve with normal flow rule, suffers from several issues. These issues are addressed with the MCE rheology: The angle of fracture and the post-fracture deformation are partially decoupled from the yield curve and the confinement pressure will have less of an effect than with an elliptical yield curve.

6.3.2 Teardrop and Parabolic yield curve

Teardrop (TD) and Parabolic Lens (PL) rheologies show very small fracture angles when used with a small tensile strength factor ($k_t < 5\%$). Both rheologies show very good agreement with the theoretical prediction of fracture angles with a normal flow rule. After the modifications proposed in Sections 2.2.6 and 2.2.7, the fracture patterns are very clear and are similar to the fracture with the standard rheology. These two rheologies are defined with a normal flow rule, an advantage of stability that favors the solver's numerical convergence.

However, these two rheologies are not without drawbacks: First, the fracture angles are linked to the tensile factor k_t and cannot be set independently. Second, only after important modifications to the original formulations of the rheologies (Zhang and Rothrock, 2005), it was possible to obtain realistic a fracture angles in uniaxial compression. For more complicated situations, the numerical robustness of these rheologies is unclear.

6.4 Summary

In this chapter, I investigated the angle of fracture of alternative rheologies. Results show that a different viscous formulation leads to increased numerical errors, therefore using a fully plastic flow rule is preferable. The Mohr–Coulomb rheologies create LKFs with fracture angles that agree with the Arthur angle. This result disagree with the results of Chapter 5 where the Roscoe angle gave precise predictions. The reasons for this difference are still unclear. The Mohr–Coulomb yield curve with an elliptical plastic potential can be used to reduce the fracture angle below 30° . The Teardrop and Parabolic Lens rheologies agree well with all theories and can create very small fracture angles when used with small tensile strength.

Chapter 7

Fracture angles with heterogeneous sea ice cover

We never tired of watching our little craft cut her way through the unbroken pans of ice. The great masses of ice were thrust aside very readily; sometimes a piece was split from a large floe and wedged under a still larger one, pushing this out of the way, the commotion causing the ice in the immediate vicinity fairly to boil.

— *Josephine Diebitsch Peary, My Arctic Journal, 1893*

The idealized uniaxial compression experiment proved to be a valuable tool to investigate the sea ice VP rheology. The idealized initial and boundary conditions allow to isolate the effect of the different rheologies. Results presented in previous chapters and sections show that the rheology determines the magnitude of stress at fracture, the fracture angle, and the post-fracture behavior (e.g., ridging or lead opening). Different shapes of yield curve and plastic potential lead to different behaviour. The shapes of the yield curve and plastic potential can be designed to represent the observed fracture angles in sea ice simulations. However, sea ice dynamics is more complex and involves many processes that are not represented in idealized experiments.

In this chapter, I generalize the idealized experiment by using a more realistic initial sea ice cover. Figure 4.9 showed that the geometry of the initial sea ice cover has an influence on the fracture angle, but the sea ice field was not very realistic. Sea ice is not an homogeneous medium, its heterogeneity appears at different scales and influence the sea ice dynamics. For example, brine channels form over time in initially homogenous new ice, creating a network of small scale weaknesses (Petrich et al., 2007). As temperatures vary with the seasons, ice dilates and contracts. This deformation creates thermal cracks (Johnson and Metzner, 1990), which serve as points of weakness for future deformations. After a fracture event, leads open or ridges form, which creates local weak (thin ice) or strong points (refrozen leads). Finally, sea ice leads range from tenth of meters to thousand of kilometers, influencing ice heterogeneity at all scales (Hutter et al., 2018; Bouchat and Tremblay, 2017). To summarize, sea ice heterogeneity influences the ice dynamics at all scales: weaknesses act as stress localisators for deformations, while strong regions transmit stresses without breaking and straining.

7.1 Initial heterogeneous ice cover

To create initial conditions with an heterogeneous ice cover, I use the initial conditions from Herman (2016), available as supplement to their study. The initial ice thickness and concentration for their discrete element sea ice element model consist of circular ice floes of diameters between 50 and 150 meters, with a thickness of 1.5 m. Some pairs of ice floes are linked with a *bond* of 1 m thick ice. The width of the bond is determined by the diameter of the smaller ice floe of the pair. The initial conditions do not represent a floe, but an assemblage of floes. The new domain is wider to enclose the new initial condition. Table 7.1 list the modified parameters of the experiments.

Table 7.1: Altered model parameters from to Table 6.1

Symbol	Definition	Value	Unit
N_x, N_y	Size of the domain	560×1000	
L_x, L_y	Size of experiment	14×25	km
l_x, l_y	Ice floe's size	$\simeq 13 \times 25$	km
A	Average initial ice concentration	97.1	%
h	Average initial ice thickness	1.38	m

To recreate these initial thickness and concentration field for our setup, a 5 m grid is superposed over the field, and given the position of the ice floes and ice bonds, grid cells are filled with ice with the corresponding thickness. All cells outside of the floes and bonds are left as open-water. The simulation resolution is 25 m, so the thickness and concentration fields are coarse-grained, each new pixel being the average value of 25 pixels of the previous grid (5 by 5 square). Some of the initial ice floes are left out on the northern and southern boundaries in order to have a straight boundary with enough ice to be able to prescribe a velocity on the assemblage of floes.

Figure 7.1 shows the results of this reconstruction process. The average ice thickness and ice concentration in the field are of 1.38 m and 97.1%. There are two large weaknesses in the initial ice thickness and concentration (indicated by red boxes), with fewer ice floes than in the rest of the field. These two weaknesses play a role as fracture localization in the original DEM compression study, see Herman (2016, their Figure 5).

7.2 Results

7.2.1 Elliptical yield curve with normal flow rule (ENFR)

Figures 7.2 shows the shear $\dot{\epsilon}_{II}$ and divergence $\dot{\epsilon}_I$ inside the ice pack after 5 seconds of simulation for the standard elliptical yield curve with normal flow rule and three ellipse ratios $e = 0.7, 2.0,$ and 5.0 . For these three parameters, the large weaknesses act as stress localisators: the main fracture lines start or terminate where the ice is weaker. In addition to the main fracture lines, small secondary fractures link smaller weaknesses and create a network of fracture lines with multiple diamond shapes. The main fracture lines in in panels b and c agree qualitatively with the two fracture lines shown in Herman (2016, their Figure 5).

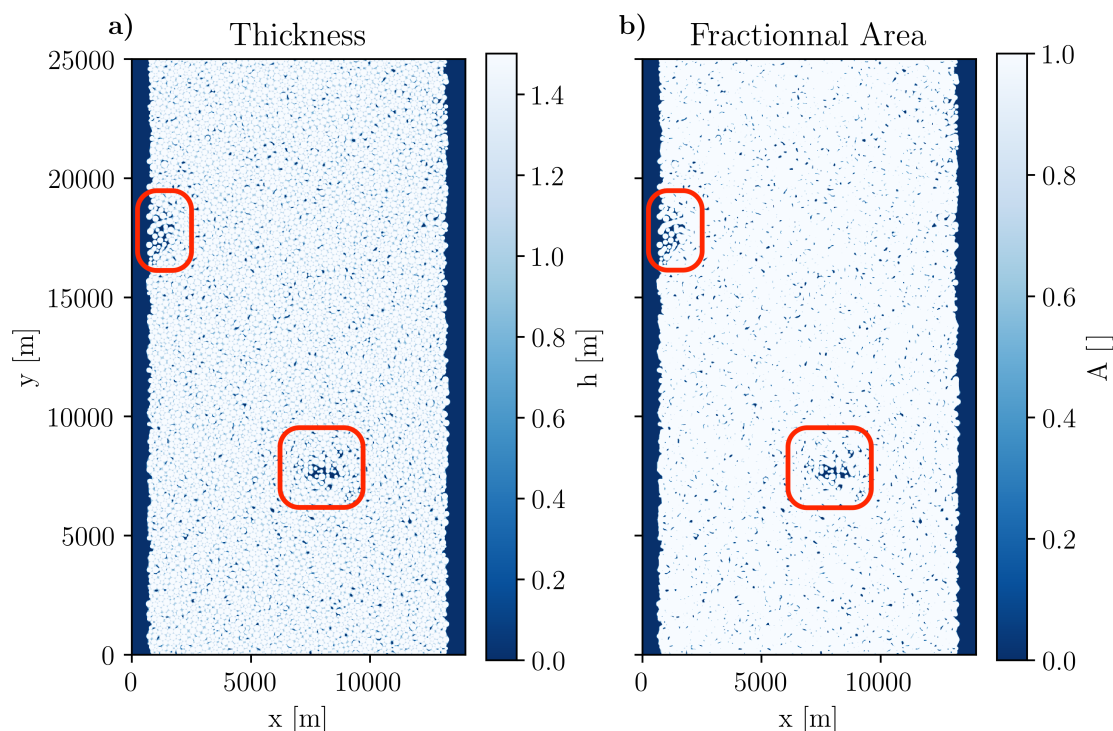


Figure 7.1: Ice thickness (a) and fractional area (b) reproduced from Herman (2016). Two weaknesses are embedded in the assemblage of floes, circled in red.

Besides the effect the weak points, the rheology influences the creation of the fracture lines. The fracture angles follow the results presented in Chapter 4. The fracture angles are larger for $e = 0.7$ than for the large values of e and only for $e = 0.7$ there is convergence (red colours) within the densely packed floes. This experiment also includes fewer secondary fractures than with $e = 2.0$ or $e = 5.0$ because the shear strength is higher. The fracture pattern with $e = 2.0$ features more divergence and smaller angles. Finally, a large ellipse ratio $e = 5.0$ does not change the fracture angles compared to $e = 2.0$: the fracture angles cannot get smaller than with the elliptical yield curve with a normal flow rule, see Figure 4.10.

Surprisingly, there are small regions of convergence along the divergent fracture lines with $e = 2.0$ and $e = 5.0$ (shown in red in Figure 7.2e and f). Figure 7.3 is a zoom of Figure 7.2e. The ridging originate from the heterogeneity and especially from the presence of thinner ice between the ice floes.

7.2.2 Elliptical yield curve with non-normal flow rule (ENNFR)

Including an elliptical plastic potential with a different ellipse ratio than the yield curve can reduce the fracture angle (Chapter 5). I investigate here the effect of changing the plastic potential ellipse ratio while keeping the yield curve constant with the heterogeneous ice cover. I use the standard ellipse aspect ratio $e_F = 2.0$. Figure 7.4 shows the fracture pattern ($\dot{\epsilon}_I$ and $\dot{\epsilon}_{II}$) for three plastic potential ellipse ratios: $e_G = 1.2$, 1.4, and 5.0.

With $e_G = 1.2$ (panels a and d), the fracture angles are very acute, many lines appear almost aligned with the direction of forcing, the y-axis, with an angle of 0° . A

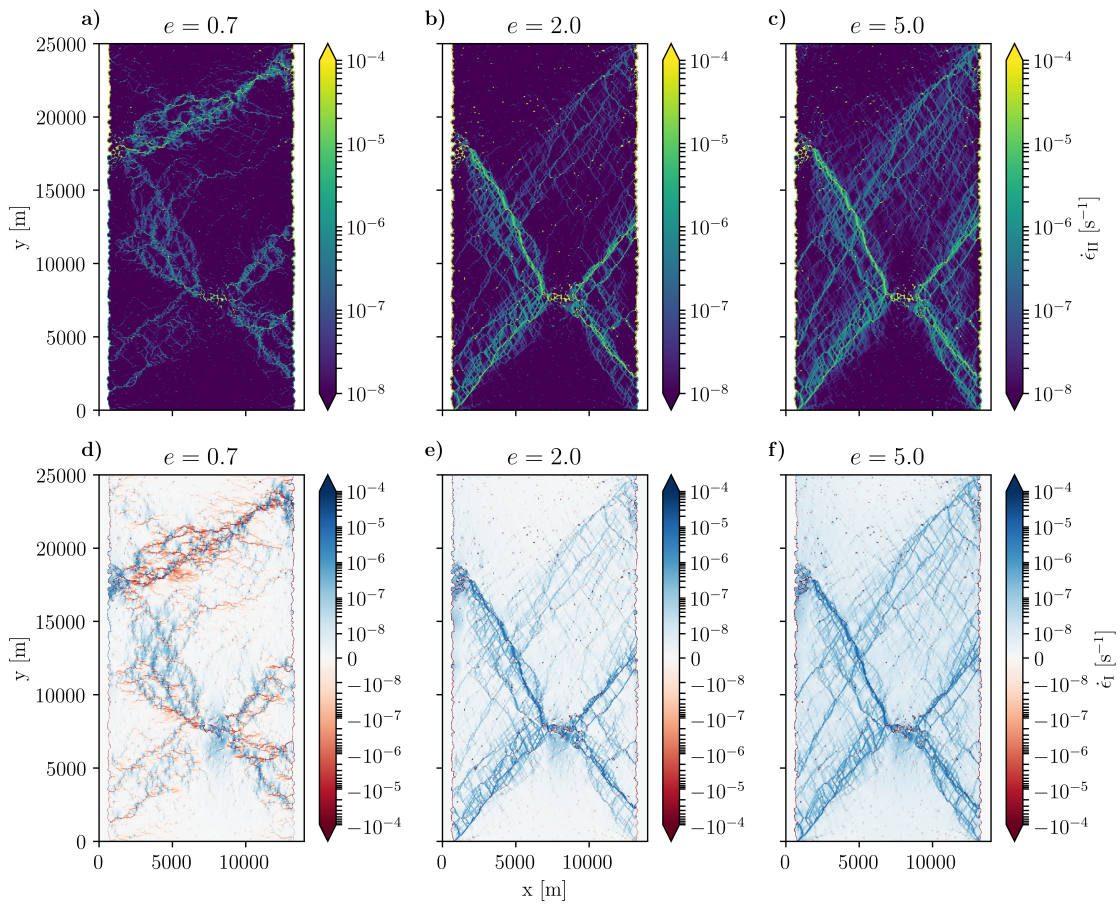


Figure 7.2: Shear $\dot{\epsilon}_{II}$ and divergence $\dot{\epsilon}_I$ after 5 seconds of simulation with an ellipse ratio of $e = 0.7$ (panel a and d), $e = 2.0$ (panel b and e), and $e = 5.0$ (panel c and f). The central panels (b and e) show the results with the standard sea ice rheology (Hibler, 1979).

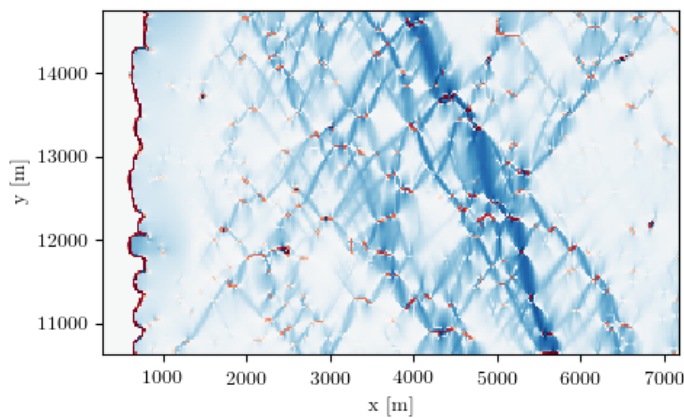


Figure 7.3: Detail of Figure 7.2e. Divergence $\dot{\epsilon}_I$ with the standard rheology. There is localized convergence (dark red) in the middle of divergent fracture line (dark blue.)

fracture line with very small fracture angles starts from the top-left corner and joins one of the major fracture lines. The fracture lines are not very straight. The whole fracture pattern does not appear very realistic. Most of fracture lines observed at

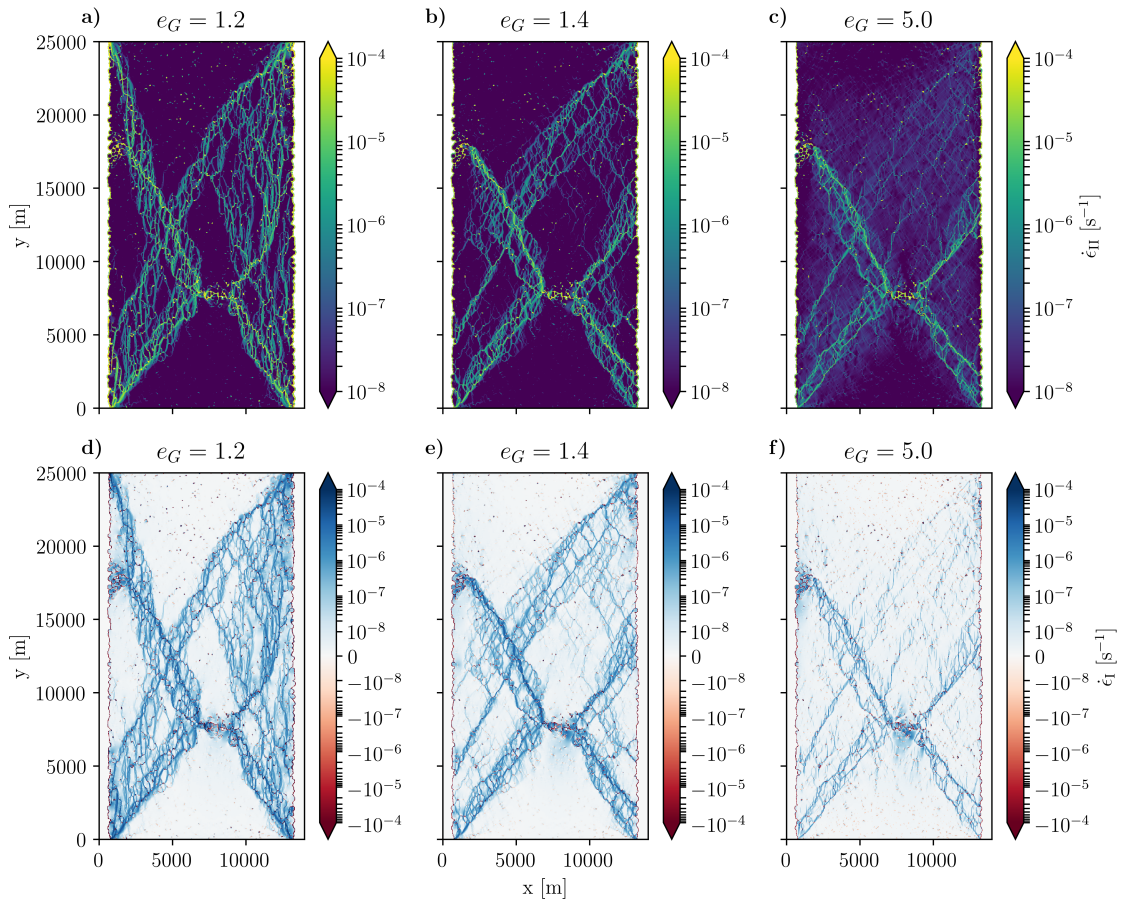


Figure 7.4: Shear $\dot{\epsilon}_{II}$ (a,b,c) and divergence $\dot{\epsilon}_I$ (d,e,f) strain rates with the Elliptical yield curve with non-normal flow rule for three plastic potential ellipse ratio e_G . The yield curve ellipse ratio is $e_F = 2$ for all three simulations.

the floe scale in the Arctic sea ice are linear and with sharp angles. With $e_G = 1.4$ (panels b and e), a more realistic fracture pattern appears with acute angles and many diamond shaped deformation patterns. With $e_G = 5.0$ (panels c and f), only the main fracture lines remain. The secondary fractures lines are weak and some are aligned with the y -axis, and there is a diffuse shear deformation. This behavior is very unrealistic.

7.2.3 Mohr–Coulomb yield curve with an elliptical plastic potential (MCE)

The MCE rheology also allows to reduce the fracture angle, see Section 6.2.2. Figure 7.5 shows the fracture pattern ($\dot{\epsilon}_I$ and $\dot{\epsilon}_{II}$) for three different settings. The tensile factor is kept constant at $k_t = 0.05$.

With $e = 2.0$ and $\mu = 0.7$ (panels a and d), there are many secondary fractures in between the main fracture lines when compared to the standard rheology. These fracture lines may appear because the strength of sea ice for small compressive stress is reduced with a Mohr–Coulomb yield curve compared to an elliptical yield curve. With $e = 1.0$ and $\mu = 0.7$ (panels b and e). The fracture angles are as acute as for the elliptical yield curve with a non-normal flow rule (ENNFR, Figure 7.4a and d), but the fracture lines are more straight. A fracture line is also created from the top

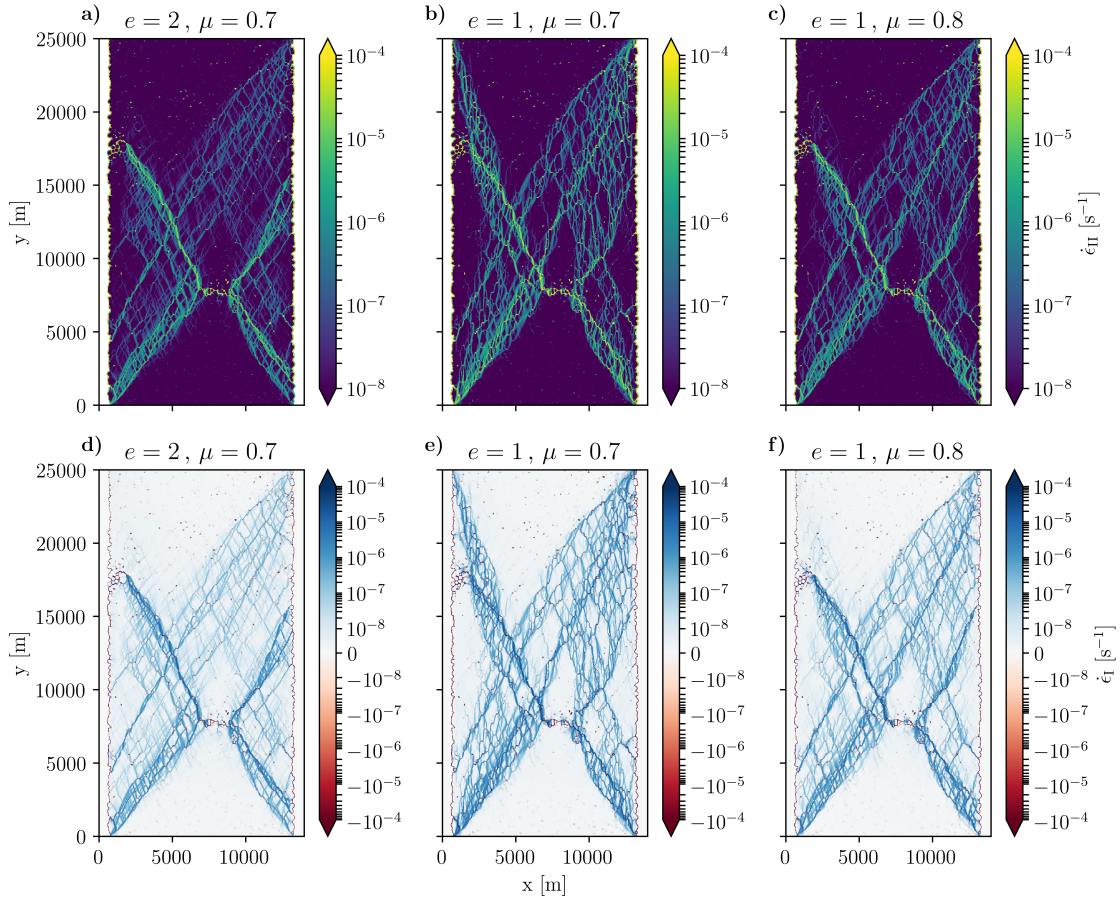


Figure 7.5: Shear $\dot{\epsilon}_{II}$ (a,b,c) and divergence $\dot{\epsilon}_I$ (d,e,f) strain rates with the Mohr–Coulomb yield curve with elliptical plastic potential (MCE). The tensile factor is $k_t = 0.05$ for all simulations.

left corner and joins the main fracture. With $e = 1.0$ and $\mu = 0.8$ (panels c and f). The fracture lines are look similar to the case with $e = 2.0$ and $\mu = 0.7$ (panels a and d), although the $e = 1$ and $\mu = 0.8$ settings favor fracture lines with small fracture angles.

The fracture angle in uni-axial loading is degenerated with this rheology and several sets of parameters (μ, e, k_t) create the same angle of fracture, as it also appears from the theoretical predictions shown on Figure 3.8.

7.2.4 Teardrop and Parabolic Lens rheologies

Unfortunately, it was not possible to obtain a converged solution with the Teardrop and Parabolic Lens rheologies with a heterogeneous ice cover. In contrast to the experiment with a uniform ice cover, the experiments with heterogeneous ice cover create more diverse stress and strain conditions, lead to more diverse stress states inside the field. The problem appear to stem from the tips of the yield curve, that is, at stress states $\frac{\sigma_I}{P} \simeq -1$ or $\frac{\sigma_I}{P} \simeq k_t$, and from the band from the viscous states during small deformation. I found that numerical overflow errors appear in the evaluation of the square root of very large values of $h = \frac{\dot{\epsilon}_I}{\dot{\epsilon}_{II}}$ in the expression of u (Equation 2.76), that lead to very large errors in the approximations.

I propose several strategies to improve this rheology and make it suitable for more realistic simulations:

- The tensile tip of the yield curve ($\frac{\sigma_I}{P} \simeq k_t$) can be replaced by the tip of the elliptical yield curve with normal flow rule. This as to be done in a way that will ensure continuity and differentiability of the yield curve and the flow rule.
- For high compressive stress ($\frac{\sigma_I}{P} \simeq -1$), a Taylor expansion can be used to regularize the function and avoid numerical overflow errors in the square-root.
- The treatment of viscous deformation in these rheologies requires additional thought. The main difference between these two rheology and the elliptical yield curve is that viscosities η and ζ are consistently regularized, that is, limiting to maximum values need to correspond to each other. I fixed this issue for the uni-axial compression experiment, but the solution seems to fail for the tips of the yield curves, when $\dot{\epsilon}_{II}$ is small in comparison to $\dot{\epsilon}_I$.

Only when these problems are solved, then these rheologies will be useful at high-resolution in realistic experiments.

7.2.5 Fracture Angles

Table 7.2 presents the average values and ranges of the modeled angles with a heterogeneous ice cover for the nine simulations shown in Figures 7.2, 7.4, 7.5. The modeled angles were measured only for deformation lines with $\dot{\epsilon}_{II} > 10^{-7}$. For comparison, Table 7.2 also shows the predicted angles. The predictions are given by the Roscoe angles for the ENNFR rheologies, while they are given by the Arthur angles for the MCE rheologies. In the case of the ENFR rheologies, all theories predict the same values.

The variation among the angles are much larger than with a homogeneous ice cover with $2\sigma \approx 10^\circ$. Note that the variation range is smaller for the Mohr–Coulomb rheologies. For most of the rheologies, the modeled angles are larger than the predicted value, with the notable exceptions of the ENFR rheology with $e = 0.7$, and the ENNFR rheology with $e_F = 2.0$; $e_G = 5.0$.

7.3 Discussion

The uni-axial loading experiments with a realistic initial sea ice covers allow several concluding remarks:

- Fracture lines are primarily determined by the position of weaknesses in the ice. They link these weaknesses with some modification incurred by the rheology. On the one hand, large weaknesses have a strong impact on the fracture lines. Results shows that they act as localization points for the most active shear lines. On the other hand, small weaknesses also act as localization points, but with a larger impact of the rheology. The rheologies defines the succession of fracture lines that link the small weaknesses as the assemblage of floes fails under compression. Different rheologies lead to a different pattern of secondary fractures, while the main fracture lines depend on the large weak points. In

Table 7.2: Modeled and predicted angles with a heterogeneous ice cover. Error ranges correspond to two standard deviation (2σ ; 95% interval). For the predicted angle θ , the indices denote the different theories: R for Roscoe, A for Arthur, and $*$ for all. The highlighting color indicates that: the average fracture angles larger than the standard rheology (red), the average fracture angle smaller than the standard rheology but above 30° (orange), and the average angle is smaller than 30° (green). ENFR refers to the Elliptical yield curve with normal flow rule, ENNFR refers to the Elliptical yield curve with non-normal flow rule, and MCE refers to the Mohr–Coulomb rheology with an elliptical plastic potential.

Rheology	Parameters	Modeled angle	Predicted angle (Theory)
ENFR	$e = 0.7$	(51.11 ± 14.60)°	60.68° (θ_*)
	$e = 2.0$	(37.69 ± 11.26)°	33.99° (θ_*)
	$e = 5.0$	(35.94 ± 11.32)°	30.67° (θ_*)
ENNFR	$e_F = 2.0$; $e_G = 1.2$	(23.71 ± 11.28)°	25.66° (θ_R)
	$e_F = 2.0$; $e_G = 1.4$	(32.32 ± 9.040)°	28.80° (θ_R)
	$e_F = 2.0$; $e_G = 5.0$	(34.25 ± 8.040)°	40.69° (θ_R)
MCE	$e = 2.0$; $\mu = 0.7$	(31.95 ± 8.080)°	26.93° (θ_A)
	$e = 1.0$; $\mu = 0.7$	(26.45 ± 9.920)°	16.63° (θ_A)
	$e = 1.0$; $\mu = 0.8$	(28.54 ± 7.040)°	22.23° (θ_A)

special cases, the change in the rheology is large enough that even the major fracture lines are changed.

- Ridging takes place along fracture lines, where two ice floes interact. Localized ridging is characteristic for the granular nature of sea ice: ridging appears along the lines of fracture as two ice floes ridge on localized points. The ridging during shear is included in the redistribution function of the Ice Thickness Distribution (ITD) (Thorndike et al., 1975). Localized ridging is present with all the rheologies with heterogeneous ice cover but not with homogeneous ice cover. If this behavior emerges because of the initial conditions, question remains about the capacity of high-resolution models to recreate such an heterogeneity.
- The fracture lines still follow the results of the uniaxial compression experiments. With alternative rheologies, the fracture angle can be decreased even with an heterogeneous sea ice cover. Using the ENNFR rheology or the MCE rheology allow to create fracture angles below the limit of the ENFR rheology of 30° . I infer: the presence of the main weaknesses favours one fracture angle, the rest of the ice deformation is then determined the rheology.
- The distribution of fracture angles is broad with a heterogeneous ice cover. Incorporating weaknesses in the initial sea ice cover creates a broader range of strain and stress condition, the plastic deformation does not only happen during uniaxial compression condition (i.e., $\sigma_{12} \neq 0$). The MCE rheology shows smaller variations in the fracture angles. I infer that this behaviour comes from the straight Mohr–Coulomb part of the yield curve.

The results illustrate the effect of a heterogeneous ice cover on the fracture. However, these experiments include many more parameters than idealized geometries. The effects of these parameters on the fracture pattern remain to be studied. For example, the two major weaknesses could be filled with more floes and bonds. Additionally, the effect of the floe size on the fracture should be studied. Also, the ice cover used here is more realistic than a uniform thickness, but an observed sea ice cover will yield yet again different results, especially with non circular ice floes. Finally, a thorough comparison between DEM and the continuous VP model is, to my knowledge, still missing.

Besides the heterogeneity of the sea ice cover, there is two other factors that modify the angle of fracture:

- **The heterogeneity of forcing** The forces that puts in sea ice in motion are surface forcing like wind and ocean currents. Such forcing is very different with the forcing in the idealized experiments. The main difference with surface forcing is that stresses are applied along the sea ice field, and stress add up as they are transmitted to surrounding ice. This type of forcing creates stress gradients along the ice field, and these gradients may influence the angle of fracture. Preliminary experiments with the standard rheology show that a gradient of stress has a tendency to create fracture curves rather than fracture lines.
- **The geometry of the coastline** The closed boundary against which the ice is pushed in the idealized experiments is a straight line and does not present any roughness that would influence the orientation of the fracture lines. In the Arctic ocean, and in a lesser extent to Antarctic waters, sea ice dynamics are influenced by the coastline. Sea ice is compressed by wind in between the coasts. Geographical features such as capes or points initiate fracture lines, while bays, fjords, and shallow waters acts as anchor points for landfast ice. Preliminary experiments show that the coastline geometry does not influence the angles of fracture, but affects the localization of the fracture lines.

Lemieux et al. (2020) recently presented a downscaling scheme for ice pressure, between the modelling scale (ca. 10 km) and the ship scale (ca. 10 m). They analyzed the pressure on a ship at the tip of a linear lead embedded in an homogeneous ice cover. They show that local ice stress can reach up to three times the large scale ice stress. More realistic heterogeneous ice covers or different rheologies may influence these results. Furthermore, using ship data could be used to discriminate between rheologies, for example from observation gathered during the SHEBA or MOSAiC expeditions.

7.4 Summary

In this chapter, I investigated the creation of fractures in a heterogeneous initial ice cover. The initial ice thickness field featured two major weaknesses and multiple small weaknesses. Results show that major weaknesses act as localization points for LKFs and influence the angle of fracture. LKFs have a tendency to link the weak points, but with modification due to of the rheology. The fracture angles with a heterogeneous ice cover follow the same trends with a homogeneous ice cover.

The deformations with a heterogeneous ice cover creates localized convergence along divergent fracture lines. Fractures angles with the Mohr–Coulomb yield curve show smaller variations than other rheologies with elliptical yield curves. Finally, both the elliptical yield curve with a non-normal flow rule and the Mohr–Coulomb yield curve with elliptical plastic potential lead to fracture angles below 30° .

Chapter 8

Conclusions and outlook

Celui qui médite vit dans l'obscurité ; celui qui ne médite pas vit dans l'aveuglement. Nous n'avons que le choix du noir.

— Victor Hugo

8.1 Conclusions

This thesis shows that the formulation and parameters of the viscous-plastic (VP) rheologies set the fracture angles in sea ice simulations. Two parameterizations characterize a sea ice VP rheology: the yield curve sets the ice strength, and the flow rule sets the post-fracture behavior. Different theories are used to predict the orientation of fracture lines (or shear bands) in plastic models. I used the Mohr's circle of stress to adapt two of these theories to the context of sea ice modeling. For a flow rule normal to the yield curve, both theories are equivalent, and the predicted angles are equal. For a non-normal flow rule, three different predictions are competing, influenced by the yield curve (Coulomb angle), the flow rule (Roscoe angle), or both together (Arthur angle).

The standard VP sea ice rheology, with an elliptical yield curve and a normal plastic flow rule, is unable to produce angles of fracture below 30° in uniaxial compression. The elliptical shape of the yield curve is responsible for this behavior. The general theory predicts this behavior accurately. The results also highlight that this rheology is unable to reproduce sea ice's behavior as a granular material: the fracture angles are highly dependent on confinement. Also post-fracture deformations (lead opening or ridging) depend on the shape of the yield curve.

The orientation of the non-normal flow rule influences the angle of fracture in sea ice VP rheologies. With a new rheology with an elliptical yield curve and a non-normal flow rule, I show that changing the orientation of the plastic flow rule with a constant yield curve has a strong impact on the fracture angles. In this case, the Roscoe Angle predicts precisely the angles of fracture. This new rheology addresses some issues of standard rheology: the post-fracture behavior is not linked only to the yield curve, and the effect of confinement pressure can be reduced. The non-normal flow rule comes to the cost of slower numerical convergence but can create fracture angles as low as 22° .

I have tested alternatives to the elliptical rheologies. Results show that both the yield curve and the flow rule influence the fracture angles with Mohr–Coulomb (MC) yield curves, and the fracture angle corresponds to the Arthur angle. I compared two equivalent MC rheologies with different formulations and showed that the flow rule has to be fully plastic to model fracture lines. With a new MC yield curve, it is possible to reduce the fracture angles below 30° . The Teardrop and Parabolic lens

yield curves with normal flow rule showed good agreement with the general fracture theory, and can create small fracture angles.

The relationship between fracture angles and rheology observed in homogeneous sea ice experiment is still valid with a heterogeneous ice cover. Inhomogeneities in the sea ice cover play the role of seeds for deformation, the rheology then influences the creation of the fractures between them. The elliptical yield curve with a non-normal yield curve and the new MC yield curve can reduce the fracture angles below that of the standard rheology. They are candidates to reduce the angle of fracture in high-resolution sea ice simulations.

To summarize, the results of the idealized experiments allow answering all three research questions outlined on page 17: **RQ1**: The fracture angles depend on both the shape of the yield curve and the orientation of the flow rule, but not on the absolute value of the ice strength. **RQ2**: Theoretical predictions correspond to the modeled fracture angles accurately with normal flow rules. With a non-normal flow rule, the best theoretical prediction depends on the shape of the plastic potential. **RQ3**: I propose two yield curves that can potentially reduce the fracture angles in high-resolution arctic simulations. Furthermore, the knowledge gained by answering these questions opens the field of sea ice modeling to new VP rheologies and more accurate sea ice modeling for new generations of climate models.

8.2 Outlook

One of the goals of the MOSAiC (Multidisciplinary drifting Observatory for the Study of Arctic Climate, Dethloff et al., 2016) expedition in 2019/2020 is to observe sea ice dynamics during a full year. The high-resolution observations of sea ice stress and deformation can help design new rheologies based on spatial and temporal high-resolution observations. The simultaneous measurements of both sea ice deformation, thickness, and sea ice stresses would indicate the orientation of the flow rule for different stress states. Such a simultaneous dataset is available at the laboratory scale (Weiss and Schulson, 2009), but not at the sea ice floe scale.

Also, observations made during MOSAiC could be used to compare the performance of different sea ice rheologies at very high resolution. I can outlay the design of such an experiment: a very high-resolution modeling domain surrounds the ship with a grid spacing of 10 m to 25 m. The ice cover (ice thickness and concentration) is initialized from the measurements of different instruments. Meteorologic and oceanic forcings are taken from local measurements (wind, temperature, humidity, heat fluxes). The high-resolution domain's boundary conditions are set either by the extended network of buoys or by a surrounding pan-arctic model at lower resolution (i.e., nested models approach). The performance of the different sea ice rheologies is assessed with different sets of measurements: the high-resolution sea ice drift from the shipborne sea ice radar, the large scale drift from the close and extended network, and the ice stress buoys. Such a high-resolution experiment could also be used to explore and test new methods of data assimilation for sea ice models (i.e., Giannakis, 2019).

New rheologies for high-resolution sea ice models can include more parameterizations to represent the dynamical processes at the subgrid-scale. These new parameterizations can then be linked to the rheology. For instance, the granular nature of sea ice can be modeled by including Floe Size Distribution (FSD) (Horvat

and Tziperman, 2015; Roach et al., 2018). Such parametrization gives valuable information for ship navigation in sea ice and can be used to set an ice strength that varies in time and space. Furthermore, the FSD could be back-fed to a rheology for granular material, for example, a $\mu(I)$ rheology (Jop et al., 2006; Forterre and Pouliquen, 2008). The $\mu(I)$ rheology features a variable Mohr–Coulomb yield curve that changes shape depending on the grain size. Alternatively, the FSD can influence the rheology by changing the angle of dilatancy based on a double sliding rule (Balendran and Nemat-Nasser, 1993; Tremblay and Mysak, 1997).

Once suitable rheologies have been designed, the next step would be to test them in Arctic high-resolution (ca. 1 km) sea ice simulations. The modeled LKFs should be compared to metrics based on observations. Not only the distribution of the intersection angles needs to be reproduced (Hutter and Losch, 2020) but also the spatial and temporal scaling law of LKFs (Bouchat and Tremblay, 2017; Hutter et al., 2018), the sign and magnitude of divergence along the LKFs (Stern et al., 1995; Bouchat and Tremblay, 2017), or the presence of fast ice (Lemieux et al., 2016; Olason, 2012). At a larger scale, such a rheology should be able to reproduce the decay of sea ice area, extent, and volume due to the current anthropogenic climate change.

Acknowledgments

I first would like to thank Martin Losch for his supervision all along my PhD project, for his motivating comments, and for pushing me further when I could not see the way. I would like to thank Bruno Tremblay for having me as a visiting student in Montreal, for being so passionate about my project, his positivity that gave me the motivation to continue, and always showing me the value of my work. Thanks to Thomas Jung and Sergey Danilov for their help and guidance during these three years. Finally, I would like to thank Christian Haas for accepting to review this thesis.

In addition, I would like to thank: Mathieu Plante for the long discussions about rheologies, yield curves and other flow rules, during his visits in Germany or my stay in Canada. Nils Hutter for the numerous discussion on sea ice models, academic life, writing, and more, and its comments on the first two chapters of this work. Amélie Bouchat and Jean-François Lemieux for their help with the Mohr–Coulomb yield curve and stimulating discussions on sea ice rheologies.

The work in this thesis was supported by the Deutsche Forschungsgemeinschaft (DFG) through the International Research Training Group “Processes and impacts of climate change in the North Atlantic Ocean and the Canadian Arctic” (IRTG 1904 ArcTrain).

Thanks to Nico, my dear friend, flatmate, and colleague during these past years for his strong friendship and motivating support. Thanks to Jean-Louis and Alix, without you, this time in Bremerhaven would not have been as joyful as it was. Thanks to Janin for this amazing friendship, your kindness and support. Thanks to Malena for the good moments spend together. Thanks to Lenni, Ragi and their little Anuka for their kindness and the wonderful time we shared as flatmates and friends. Thanks to Niels, Vincent and Cora for making sharing a flat a wonderful experience, even during the tensed COVID-19 period. Thanks to Stephan and Franzi who welcomed us so well in Bremerhaven and for these good climbing times, I wish them the best with their Jonas. Thanks to all my officemates through the years for a pleasant (and sometimes fun) office: Vibe, Claudia, Elena, Margarita, Deniz and Yuqing. Thanks to the community of PhD students at the AWI, there is too many names to be cited, but I would like to thank the AWI DokTeam for a fun year together: Thomy, Anna, Franzi, Jana, Santi, Nicole and Nico.

Thanks to the ArcTrainees, from Germany, Canada and beyond, for these years together, our common support, our common activities. Thanks to ArcTrain for the wonderful opportunities they offer, especially the ArcTrain Floating University PS115.2 on Polarstern and the ArcTrain summer school 2019. Thanks to all Canadian people that made my research stay in Montréal a wonderful time and all the

McGill CAOS students, faculty and staff; and I hope seeing you all very soon again. A special thank you to Magali and her cat for the great time sharing your flat.

Un grand merci à Bernadette et Pierre, mes deux parents pour le soutien qu'ils m'ont toujours offert et leur volonté de toujours me pousser plus loin. Merci aux familles Ringeisen et Perrel pour leur intérêt tout au long de ce doctorat. Merci au copains des éclaireurs, plus 10 ans que l'on dort sous la tente de nos amitiés!

List of Figures

1.1	Temperature anomaly and arctic amplification	13
1.2	Comparison Arctic sea ice between 1979 and 2018	14
1.3	Aerial photograph of sea ice floes and fracture	15
2.1	1D Elastic-Plastic and Viscous-Plastic models	20
2.2	2D viscous-plastic yield curve and flow rule	21
2.3	Example of yield curve and plastic potential	24
2.4	Elliptical yield curve with normal flow rule	26
2.5	Elliptical yield curve with non-normal flow rule	31
2.6	Mohr-Coulomb yield curve with shear only	33
2.7	Mohr-Coulomb yield curve with elliptical plastic potential	34
2.8	Coulombic (or TEM) yield curve	35
2.9	Teardrop and Parabolic Lens yield curves	36
3.1	Illustration of the internal angle of friction and the angle of dilatancy	42
3.2	Stress on a sea ice element	43
3.3	Mohr's circle and Coulomb's failure criterion	45
3.4	Linking the slope of yield curve and the internal angle of friction	46
3.5	Linking the slope of yield curve and the flow rule	47
3.6	Stress and flow rule in uni-axial compression	49
3.7	Mohr's circle applied to the elliptical yield curve	50
3.8	Theoretical fracture angle with the MCE rheology	53
3.9	Mohr's circle applied to the Coulombic yield curve	53
3.10	Theoretical fracture angle with the TD and PL rheologies	55
4.1	Elliptical and Coulombic yield curve	63
4.2	Experimental schematics for uniaxial compression	64
4.3	Deformation pattern with the reference simulation	67
4.4	Evolution of stresses in uni-axial compression	67
4.5	Deformation pattern at different resolutions and scales	68
4.6	Creation of leads and floes at high-resolution	69
4.7	Deformation pattern with the effect of free-slip and no-slip boundary conditions	69
4.8	Deformation pattern with the effects of confining pressure	71
4.9	Deformation pattern with heterogeneous sea ice initial conditions	71
4.10	Fracture angles as a function of ellipse aspect ratio e and slope parameter μ	73
4.11	Deformation pattern with ellipse ratio $e = 0.7$	74
4.12	Deformation pattern with the Coulombic rheology	75
5.1	Yield curve and plastic potential with normal and non-normal flow rule	86

5.2	Elliptical yield curve with a non-normal flow rule	88
5.3	Geometrical construction linking flow rule and fracture angle	89
5.4	Uniaxial compression with a non-normal flow rule	90
5.5	Schematics of the experiment	92
5.6	Deformation pattern with different plastic potentials	93
5.7	Fracture angles as function of the shape of the yield curve and the plastic potential	95
6.1	Deformation pattern with the MCS rheology	101
6.2	Stress states and yield curve with the MCS rheology	101
6.3	Schematics of the MCES rheology	102
6.4	Deformation pattern with the MCES rheology	103
6.5	Stress states and yield curve with the MCES rheology	103
6.6	Fracture angle as function of μ for the MCS and MCES rheologies	104
6.7	Fracture angle as function of e for the MCE rheology	105
6.8	Fracture angle as function of μ for the MCE rheology	106
6.9	Deformation pattern with the TD and PL rheologies	106
6.10	Fracture angle as function of k_t for the TD and PL rheologies	107
7.1	Heterogeneous initial ice cover	113
7.2	Deformation pattern with the ENFR rheology and the heterogeneous ice cover	114
7.3	Detail of Figure 7.2e showing local convergent motion	114
7.4	Deformation pattern with the ENNFR rheology and the heterogeneous ice cover	115
7.5	Deformation pattern with the MCE rheology and the heterogeneous ice cover	116

List of Tables

4.1	Model parameters of the reference simulation.	65
6.1	Model parameters for the idealized compression experiment	100
7.1	Altered model parameters from to Table 6.1	112
7.2	Modeled and predicted angles with a heterogeneous ice cover	118

List of Abbreviations

ENFR	Elliptical yield curve with normal flow rule
ENNFR	Elliptical yield curve with non-normal flow rule
GHG	GreenHouse Gases
MC	Mohr–Coulomb
MCE	Mohr–Coulomb yield curve with elliptical plastic potential
MCES	MCE rheology with $e = 50$ (shear flow rule)
MCS	Mohr–Coulomb yield curve with shear flow rule
PL	Parabolic Lens yield curve with normal flow rule
TD	Teardrop yield curve with normal flow rule
VP	Viscous-Plastic

Bibliography

- Aksenov, Ye. and W. D. Hibler (2001). “Failure Propagation Effects in an Anisotropic Sea Ice Dynamics Model”. en. In: *IUTAM Symposium on Scaling Laws in Ice Mechanics and Ice Dynamics*. Edited by J. P. Dempsey and H. H. Shen. Solid Mechanics and Its Applications. Springer Netherlands, pages 363–372 (cited on pages 70, 82).
- Alshibli, Khalid A. and Stein Sture (2000). “Shear Band Formation in Plane Strain Experiments of Sand”. In: *Journal of Geotechnical and Geoenvironmental Engineering* 126.6, pages 495–503. DOI: 10.1061/(ASCE)1090-0241(2000)126:6(495) (cited on page 95).
- Anderson, Ernest Masson (1942). *The dynamics of faulting and dyke formation with applications to Britain*. Oliver and Boyd (cited on page 82).
- Arthur, J. R. F. et al. (1977). “Plastic deformation and failure in granular media”. In: *Géotechnique* 27.1, pages 53–74. DOI: 10.1680/geot.1977.27.1.53 (cited on pages 42, 83, 107, 108).
- Astarita, Giovanni and Giuseppe Marrucci (1974). *Principles of non-Newtonian fluid mechanics*. en. McGraw-Hill (cited on page 21).
- Babić, Marijan, Hayley H. Shen, and Hung Tao Shen (1990). “The stress tensor in granular shear flows of uniform, deformable disks at high solids concentrations”. en. In: *Journal of Fluid Mechanics* 219, pages 81–118. DOI: 10.1017/S0022112090002877 (cited on page 50).
- Badgley, F. I. (1965). “Heat balance at the surface of the Arctic Ocean”. In: *US-IGY Drifting Station Alpha Arctic Ocean 1957-1958*, page 69 (cited on page 82).
- Balendran, B. and Sia Nemat-Nasser (1993). “Double sliding model for cyclic deformation of granular materials, including dilatancy effects”. In: *Journal of the Mechanics and Physics of Solids* 41.3, pages 573–612. DOI: 10.1016/0022-5096(93)90049-L (cited on pages 76, 77, 83, 91, 97, 108, 123).
- Bingham, Eugene C. (1933). “The New Science of Rheology”. In: *Review of Scientific Instruments* 4.9, pages 473–476. DOI: 10.1063/1.1749180 (cited on pages 16, 19).
- Blockley, Ed et al. (2020). “The future of sea ice modelling: where do we go from here?” In: *Bulletin of the American Meteorological Society*. DOI: 10.1175/BAMS-D-20-0073.1 (cited on page 16).
- Bolton, M. D. (1986). “The strength and dilatancy of sands”. In: *Géotechnique* 36.1, pages 65–78. DOI: 10.1680/geot.1986.36.1.65 (cited on page 83).
- Bouchat, Amélie and Bruno Tremblay (2014). “Energy dissipation in viscous-plastic sea-ice models”. en. In: *Journal of Geophysical Research: Oceans* 119.2, pages 976–994. DOI: 10.1002/2013JC009436 (cited on page 59).
- Bouchat, Amélie and Bruno Tremblay (2017). “Using sea-ice deformation fields to constrain the mechanical strength parameters of geophysical sea ice”. en. In:

- Journal of Geophysical Research: Oceans*, n/a–n/a. DOI: 10.1002/2017JC013020 (cited on pages 13, 17, 26, 59, 63, 72, 77, 78, 82, 84, 94, 97, 108, 111, 123).
- Bouchat, Amélie, L. Bruno Tremblay, and Nils Hutter (2020). “Scaling and statistical properties of sea-ice deformation fields from models participating in the FAMOS Sea-Ice Rheology Experiment”. In: *Journal of Geophysical Research: Oceans In Review* (cited on page 82).
- Bouillon, Sylvain and Pierre Rampal (2015). “Presentation of the dynamical core of neXtSIM, a new sea ice model”. In: *Ocean Modelling* 91, pages 23–37. DOI: 10.1016/j.ocemod.2015.04.005 (cited on page 16).
- Bröhan, David and Lars Kaleschke (2014). “A Nine-Year Climatology of Arctic Sea Ice Lead Orientation and Frequency from AMSR-E”. en. In: *Remote Sensing* 6.2, pages 1451–1475. DOI: 10.3390/rs6021451 (cited on page 60).
- Bronshstein, I. N. et al. (2015). *Handbook of Mathematics*. English. 6th ed. 2015 edition. Heidelberg New York Dordrecht London: Springer (cited on page 54).
- Buiter, Susanne J. H. et al. (2006). “The numerical sandbox: comparison of model results for a shortening and an extension experiment”. en. In: *Geological Society, London, Special Publications* 253.1, pages 29–64. DOI: 10.1144/GSL.SP.2006.253.01.02 (cited on page 96).
- Coon, M. D. et al. (1974). “Modeling The Pack Ice as an Elastic-Plastic Material”. In: *AIDJEX BULLETIN* No. 24. Numerical Modeling Report, pages 1–106 (cited on pages 16, 19, 20, 38, 39, 58, 75, 84).
- Coon, Max et al. (2007). “Arctic Ice Dynamics Joint Experiment (AIDJEX) assumptions revisited and found inadequate”. en. In: *Journal of Geophysical Research: Oceans* 112.C11, C11S90. DOI: 10.1029/2005JC003393 (cited on pages 16, 48, 58, 77, 97).
- Coulomb, C. (1773). “Test on the applications of the rules of maxima and minima to some problems of statics related to architecture”. In: *Mem Math Phys* 7, pages 343–382 (cited on pages 13, 41, 43, 50, 56, 83, 95).
- Cox, G. F. N. and J. A. Richter-Menge (1985). “Tensile Strength of Multi-Year Pressure Ridge Sea Ice Samples”. In: *Journal of Energy Resources Technology* 107.3, pages 375–380. DOI: 10.1115/1.3231204 (cited on page 50).
- Cunningham, G.F., R. Kwok, and J. Banfield (1994). “Ice lead orientation characteristics in the winter Beaufort Sea”. In: *Proceedings of IGARSS '94 - 1994 IEEE International Geoscience and Remote Sensing Symposium*. Volume 3, 1747–1749 vol.3. DOI: 10.1109/IGARSS.1994.399553 (cited on pages 16, 52, 83, 97).
- Curry, Judith A., Julie L. Schramm, and Elizabeth E. Ebert (1995). “Sea Ice-Albedo Climate Feedback Mechanism”. In: *Journal of Climate* 8.2, pages 240–247. DOI: 10.1175/1520-0442(1995)008<0240:SIACFM>2.0.CO;2 (cited on page 13).
- Dansereau, V. et al. (2016). “A Maxwell elasto-brittle rheology for sea ice modelling”. In: *The Cryosphere* 10.3, pages 1339–1359. DOI: 10.5194/tc-10-1339-2016 (cited on pages 16, 19, 58–60, 64, 82, 84, 97).
- Dansereau, Véronique et al. (2019). “Collective Damage Growth Controls Fault Orientation in Quasibrittle Compressive Failure”. In: *Physical Review Letters* 122.8, page 085501. DOI: 10.1103/PhysRevLett.122.085501 (cited on pages 17, 60).
- Dempsey, J. P. et al. (2012). “Fracture of a ridged multi-year Arctic sea ice floe”. In: *Cold Regions Science and Technology*. Max Coon Special issue 76-77, pages 63–68. DOI: 10.1016/j.coldregions.2011.09.012 (cited on pages 14, 76).

- Dethloff, Klaus, Markus Rex, and Matthew Shupe (2016). “Multidisciplinary drifting Observatory for the Study of Arctic Climate (MOSAiC)”. In: *EGU General Assembly Conference Abstracts* 18 (cited on pages 78, 98, 122).
- Donner, Leo J. and William G. Large (2008). “Climate Modeling”. In: *Annual Review of Environment and Resources* 33.1, pages 1–17. DOI: 10.1146/annurev. environ.33.020707.160752 (cited on page 11).
- Drucker, Daniel Charles and William Prager (1952). “Soil mechanics and plastic analysis or limit design”. In: *Quarterly of applied mathematics* 10.2, pages 157–165 (cited on pages 84, 108).
- Dumont, Dany, Yves Gratton, and Todd E. Arbetter (2009). “Modeling the Dynamics of the North Water Polynya Ice Bridge”. In: *Journal of Physical Oceanography* 39.6, pages 1448–1461. DOI: 10.1175/2008JP03965.1 (cited on pages 17, 60, 77, 94).
- Erlingsson, Björn (1988). “Two-dimensional deformation patterns in sea ice”. In: *Journal of Glaciology* 34.118, pages 301–308 (cited on pages 16, 60, 75, 77, 82, 83, 92, 97).
- Feltham, Daniel L. (2008). “Sea Ice Rheology”. In: *Annual Review of Fluid Mechanics* 40.1, pages 91–112. DOI: 10.1146/annurev. fluid.40.111406.102151 (cited on page 59).
- Fetterer, F. et al. (2017). *Sea Ice Index, Version 3*. English (cited on page 14).
- Forterre, Yoël and Olivier Pouliquen (2008). “Flows of Dense Granular Media”. In: *Annual Review of Fluid Mechanics* 40.1, pages 1–24. DOI: 10.1146/annurev. fluid.40.111406.102142 (cited on page 123).
- Francis, Jennifer A. and Stephen J. Vavrus (2012). “Evidence linking Arctic amplification to extreme weather in mid-latitudes”. en. In: *Geophysical Research Letters* 39.6. DOI: 10.1029/2012GL051000 (cited on page 12).
- Giannakis, Dimitrios (2019). “Quantum mechanics and data assimilation”. In: *Physical Review E* 100.3, page 032207. DOI: 10.1103/PhysRevE.100.032207 (cited on page 122).
- Girard, L. et al. (2009). “Evaluation of high-resolution sea ice models on the basis of statistical and scaling properties of Arctic sea ice drift and deformation”. en. In: *Journal of Geophysical Research: Oceans* 114.C8, page C08015. DOI: 10.1029/2008JC005182 (cited on pages 17, 59).
- Girard, Lucas et al. (2011). “A new modeling framework for sea-ice mechanics based on elasto-brittle rheology”. In: *Annals of Glaciology* 52.57, pages 123–132. DOI: 10.3189/172756411795931499 (cited on pages 16, 19, 59).
- Haas, Christian et al. (2009). “Helicopter-borne measurements of sea ice thickness, using a small and lightweight, digital EM system”. en. In: *Journal of Applied Geophysics*. Airborne Geophysics 67.3, pages 234–241. DOI: 10.1016/j. jappgeo. 2008.05.005 (cited on page 15).
- Harrison, V. G. W. (1940). “The Science of Rheology”. en. In: *Nature* 146.3705, pages 580–582. DOI: 10.1038/146580a0 (cited on page 16).
- Hausfather, Zeke et al. (2020). “Evaluating the Performance of Past Climate Model Projections”. en. In: *Geophysical Research Letters* 47.1, e2019GL085378. DOI: 10.1029/2019GL085378 (cited on page 11).
- Heorton, H. D. B. S., D. L. Feltham, and M. Tsamados (2018). “Stress and deformation characteristics of sea ice in a high-resolution, anisotropic sea ice model”. en. In: *Phil. Trans. R. Soc. A* 376.2129, page 20170349. DOI: 10.1098/rsta. 2017.0349 (cited on pages 17, 60, 75, 82).

- Herman, A. (2017). “Wave-induced stress and breaking of sea ice in a coupled hydrodynamic–discrete-element wave–ice model”. In: *The Cryosphere Discuss.* 2017, pages 1–21. DOI: 10.5194/tc-2017-95 (cited on page 14).
- Herman, Agnieszka (2016). “Discrete-Element bonded-particle Sea Ice model DESIGN, version 1.3a - model description and implementation”. In: *Geoscientific Model Development* 9. DOI: 10.5194/gmd-9-1219-2016 (cited on pages 17, 64, 70, 112, 113).
- Hibler, W. D. (1977). “A viscous sea ice law as a stochastic average of plasticity”. en. In: *Journal of Geophysical Research* 82.27, pages 3932–3938. DOI: 10.1029/JC082i027p03932 (cited on pages 16, 23, 62, 84, 86, 87).
- Hibler, W. D. (1979). “A Dynamic Thermodynamic Sea Ice Model”. In: *Journal of Physical Oceanography* 9.4, pages 815–846. DOI: 10.1175/1520-0485(1979)009<0815:ADTSIM>2.0.CO;2 (cited on pages 16, 20, 24, 29, 41, 58, 59, 61, 62, 66, 82, 84, 85, 87, 94, 98, 114).
- Hibler, W. D., J. K. Hutchings, and C. F. Ip (2006). “sea-ice arching and multiple flow States of Arctic pack ice”. en. In: *Annals of Glaciology* 44, pages 339–344. DOI: 10.3189/172756406781811448 (cited on page 60).
- Hibler, W. D. and Erland M. Schulson (1997). “On modeling sea-ice fracture and flow in numerical investigations of climate”. In: *Annals of Glaciology* 25, pages 26–32. DOI: 10.1017/S0260305500190019 (cited on page 52).
- Hibler, W. D. and Erland M. Schulson (2000). “On modeling the anisotropic failure and flow of flawed sea ice”. en. In: *Journal of Geophysical Research: Oceans* 105.C7, pages 17105–17120. DOI: 10.1029/2000JC900045 (cited on pages 24, 34, 41, 54, 59, 60, 62, 63, 70, 73, 77, 84, 96, 100).
- Hibler, WD and Chi F Ip (1995). “The effect of sea ice rheology on Arctic buoy drift”. In: *ASME APPLIED MECHANICS DIVISION-PUBLICATIONS-AMD* 207, pages 255–255 (cited on page 29).
- Hopkins, Mark A. (1994). “On the ridging of intact lead ice”. en. In: *Journal of Geophysical Research: Oceans* 99.C8, pages 16351–16360. DOI: 10.1029/94JC00996 (cited on pages 15, 97).
- Hopkins, Mark A. (2002). “Using DEM to Model Arctic Sea Ice”. en. In: *American Society of Civil Engineers*, pages 374–379. DOI: 10.1061/40647(259)65 (cited on page 17).
- Horvat, C. and E. Tziperman (2015). “A prognostic model of the sea-ice floe size and thickness distribution”. In: *The Cryosphere* 9.6, pages 2119–2134. DOI: 10.5194/tc-9-2119-2015 (cited on pages 14, 122).
- Horvat, Christopher and Eli Tziperman (2017). “The evolution of scaling laws in the sea ice floe size distribution”. en. In: *Journal of Geophysical Research: Oceans*, n/a–n/a. DOI: 10.1002/2016JC012573 (cited on pages 14, 97, 98).
- Hundsdoerfer, W. et al. (1995). “A Positive Finite-Difference Advection Scheme”. In: *Journal of Computational Physics* 117.1, pages 35–46. DOI: 10.1006/jcph.1995.1042 (cited on page 61).
- Hunke, E. C. and J. K. Dukowicz (1997). “An Elastic–Viscous–Plastic Model for Sea Ice Dynamics”. In: *Journal of Physical Oceanography* 27.9, pages 1849–1867. DOI: 10.1175/1520-0485(1997)027<1849:AEVPMF>2.0.CO;2 (cited on pages 58, 75).
- Hunke, Elizabeth C. (2001a). “The Elastic-Viscous-Plastic Sea Ice Dynamics Model”. en. In: *IUTAM Symposium on Scaling Laws in Ice Mechanics and Ice Dynamics*.

- Edited by J. P. Dempsey and H. H. Shen. *Solid Mechanics and Its Applications*. Springer Netherlands, pages 289–297 (cited on pages 16, 39).
- Hunke, Elizabeth C. (2001b). “Viscous–Plastic Sea Ice Dynamics with the EVP Model: Linearization Issues”. In: *Journal of Computational Physics* 170.1, pages 18–38. DOI: 10.1006/jcph.2001.6710 (cited on page 58).
- Hunkins, Kenneth (1960). “Seismic studies of sea ice”. en. In: *Journal of Geophysical Research (1896-1977)* 65.10, pages 3459–3472. DOI: 10.1029/JZ065i010p03459 (cited on page 14).
- Hutchings, Jennifer K., Petra Heil, and William D. Hibler (2005). “Modeling Linear Kinematic Features in Sea Ice”. In: *Monthly Weather Review* 133.12, pages 3481–3497. DOI: 10.1175/MWR3045.1 (cited on pages 16, 17, 23, 41, 59, 60, 75, 82).
- Hutchings, Jennifer K., Hrvoje Jasak, and Seymour W. Laxon (2004). “A strength implicit correction scheme for the viscous-plastic sea ice model”. In: *Ocean Modelling* 7.1, pages 111–133. DOI: 10.1016/S1463-5003(03)00040-4 (cited on page 58).
- Hutter, K. and K. R. Rajagopal (1994). “On flows of granular materials”. en. In: *Continuum Mechanics and Thermodynamics* 6.2, pages 81–139. DOI: 10.1007/BF01140894 (cited on pages 13, 76).
- Hutter, Nils and Martin Losch (2020). “Feature-based comparison of sea ice deformation in lead-permitting sea ice simulations”. English. In: *The Cryosphere* 14.1, pages 93–113. DOI: <https://doi.org/10.5194/tc-14-93-2020> (cited on pages 16, 41, 52, 83, 123).
- Hutter, Nils, Losch Martin, and Menemenlis Dimitris (2018). “Scaling Properties of Arctic Sea Ice Deformation in a High-Resolution Viscous-Plastic Sea Ice Model and in Satellite Observations”. In: *Journal of Geophysical Research: Oceans* 123.1, pages 672–687. DOI: 10.1002/2017JC013119 (cited on pages 17, 58, 59, 82, 97, 111, 123).
- Hutter, Nils, Lorenzo Zampieri, and Martin Losch (2019). “Leads and ridges in Arctic sea ice from RGPS data and a new tracking algorithm”. English. In: *The Cryosphere* 13.2, pages 627–645. DOI: <https://doi.org/10.5194/tc-13-627-2019> (cited on pages 13, 40, 60, 65, 77, 82, 97).
- Ip, Chi F., William D. Hibler, and Gregory M. Flato (1991). “On the effect of rheology on seasonal sea-ice simulations”. en. In: *Annals of Glaciology* 15, pages 17–25 (cited on pages 17, 20, 24, 29, 31, 63, 77, 84, 85, 92, 96).
- Ip, Chi Fung (1993). “Numerical investigation of different rheologies on sea-ice dynamics”. eng. PhD thesis. Thesis PhD–Dartmouth College (cited on pages 33, 92).
- IPCC (2013). *Climate Change 2013: The Physical Science Basis. Contribution of Working Group I to the Fifth Assessment Report of the Intergovernmental Panel on Climate Change*. Technical report. Cambridge, United Kingdom and New York, NY, USA: Cambridge University Press. DOI: 10.1017/CB09781107415324 (cited on page 11).
- IPCC (2018). *Global Warming of 1.5°C. An IPCC Special Report on the impacts of global warming of 1.5°C above pre-industrial levels and related global greenhouse gas emission pathways, in the context of strengthening the global response to the threat of climate change, sustainable development, and efforts to eradicate poverty* [Masson-Delmotte, V., P. Zhai, H.-O. Pörtner, D. Roberts, J. Skea, P.R. Shukla, A. Pirani, W. Moufouma-Okia, C. Péan, R. Pidcock, S. Connors, J.B.R.

- Matthews, Y. Chen, X. Zhou, M.I. Gomis, E. Lonnoy, T. Maycock, M. Tignor, and T. Waterfield (eds.)). Technical report. In press (cited on page 12).
- Itkin, Polona, Martin Losch, and Rüdiger Gerdes (2015). “Landfast ice affects the stability of the Arctic halocline: Evidence from a numerical model”. en. In: *Journal of Geophysical Research: Oceans* 120.4, pages 2622–2635. DOI: 10.1002/2014JC010353 (cited on pages 13, 82).
- Johnson, Jerome and Ronald Metzner (1990). “Thermal Expansion Coefficients For Sea Ice”. en. In: *Journal of Glaciology* 36.124, pages 343–349. DOI: 10.3189/002214390793701327 (cited on page 111).
- Jop, Pierre, Yoël Forterre, and Olivier Pouliquen (2006). “A constitutive law for dense granular flows”. En. In: *Nature* 441.7094, page 727. DOI: 10.1038/nature04801 (cited on page 123).
- Kaus, Boris J. P. (2010). “Factors that control the angle of shear bands in geodynamic numerical models of brittle deformation”. en. In: *Tectonophysics. Quantitative modelling of geological processes* 484.1, pages 36–47. DOI: 10.1016/j.tecto.2009.08.042 (cited on page 96).
- Keeling, Charles D. et al. (1976). “Atmospheric carbon dioxide variations at Mauna Loa Observatory, Hawaii”. en. In: *Tellus* 28.6, pages 538–551. DOI: 10.1111/j.2153-3490.1976.tb00701.x (cited on page 11).
- Kelly PA, Kelly (2020). *Mechanics Lecture Notes: Engineering Solid Mechanics* (cited on pages 23, 25, 46, 108).
- Kimmritz, Madlen, Sergey Danilov, and Martin Losch (2016). “The adaptive EVP method for solving the sea ice momentum equation”. en. In: *Ocean Modelling* 101, pages 59–67. DOI: 10.1016/j.ocemod.2016.03.004 (cited on page 39).
- Koldunov, Nikolay V. et al. (2019). “Fast EVP Solutions in a High-Resolution Sea Ice Model”. en. In: *Journal of Advances in Modeling Earth Systems* 11.5, pages 1269–1284. DOI: 10.1029/2018MS001485 (cited on page 39).
- König Beatty, Christof and David M. Holland (2010). “Modeling Landfast Sea Ice by Adding Tensile Strength”. In: *Journal of Physical Oceanography* 40.1, pages 185–198. DOI: 10.1175/2009JP04105.1 (cited on pages 16, 24, 26, 35, 54, 85, 87).
- Kreyscher, Martin, Markus Harder, and Peter Lemke (1997). “First results of the Sea-Ice Model Intercomparison Project (SIMIP)”. en. In: *Annals of Glaciology* 25, pages 8–11. DOI: 10.3189/S0260305500013719 (cited on page 12).
- Krupnik, Igor et al., editors (2010). *SIKU: Knowing Our Ice: Documenting Inuit Sea Ice Knowledge and Use*. en. Springer Netherlands. DOI: 10.1007/978-90-481-8587-0 (cited on page 99).
- Kwok, R. (2010). “Satellite remote sensing of sea-ice thickness and kinematics: a review”. en. In: *Journal of Glaciology* 56.200, pages 1129–1140. DOI: 10.3189/002214311796406167 (cited on page 15).
- Kwok, Ronald (2001). “Deformation of the Arctic Ocean Sea Ice Cover between November 1996 and April 1997: A Qualitative Survey”. en. In: *IUTAM Symposium on Scaling Laws in Ice Mechanics and Ice Dynamics*. Edited by J. P. Dempsey and H. H. Shen. Solid Mechanics and Its Applications. Dordrecht: Springer Netherlands, pages 315–322. DOI: 10.1007/978-94-015-9735-7 (cited on pages 41, 58, 75, 82).
- Lemieux, Jean-François and Bruno Tremblay (2009). “Numerical convergence of viscous-plastic sea ice models”. en. In: *Journal of Geophysical Research: Oceans* 114.C5. DOI: 10.1029/2008JC005017 (cited on pages 16, 20, 65, 91).

- Lemieux, Jean-Francois, Bruno Tremblay, and Mathieu Plante (2020). “Toward a method for downscaling sea ice pressure”. English. In: *The Cryosphere Discussions*, pages 1–26. DOI: <https://doi.org/10.5194/tc-2020-134> (cited on page 119).
- Lemieux, Jean-François et al. (2008). “Using the preconditioned Generalized Minimum RESidual (GMRES) method to solve the sea-ice momentum equation”. en. In: *Journal of Geophysical Research: Oceans* 113.C10, page C10004. DOI: 10.1029/2007JC004680 (cited on page 16).
- Lemieux, Jean-François et al. (2010). “Improving the numerical convergence of viscous-plastic sea ice models with the Jacobian-free Newton–Krylov method”. In: *Journal of Computational Physics* 229.8, pages 2840–2852. DOI: 10.1016/j.jcp.2009.12.011 (cited on page 58).
- Lemieux, Jean-François et al. (2016). “Improving the simulation of landfast ice by combining tensile strength and a parameterization for grounded ridges”. en. In: *Journal of Geophysical Research: Oceans* 121.10, pages 7354–7368. DOI: 10.1002/2016JC012006 (cited on pages 16, 123).
- Lindsay, R. W. and D. A. Rothrock (1995). “Arctic sea ice leads from advanced very high resolution radiometer images”. en. In: *Journal of Geophysical Research: Oceans* 100.C3, pages 4533–4544. DOI: 10.1029/94JC02393 (cited on page 60).
- Linow, Stefanie and Wolfgang Dierking (2017). “Object-Based Detection of Linear Kinematic Features in Sea Ice”. In: *Remote Sensing* 9.5. DOI: 10.3390/rs9050493 (cited on page 65).
- Lipscomb, William H. et al. (2007). “Ridging, strength, and stability in high-resolution sea ice models”. en. In: *Journal of Geophysical Research: Oceans* 112.C3, C03S91. DOI: 10.1029/2005JC003355 (cited on page 16).
- Losch, Martin and Sergey Danilov (2012). “On solving the momentum equations of dynamic sea ice models with implicit solvers and the elastic–viscous–plastic technique”. In: *Ocean Modelling* 41, pages 42–52 (cited on page 16).
- Losch, Martin et al. (2010). “On the formulation of sea-ice models. Part 1: Effects of different solver implementations and parameterizations”. In: *Ocean Modelling* 33.1–2, pages 129–144. DOI: 10.1016/j.ocemod.2009.12.008 (cited on pages 58, 61, 91, 99).
- Losch, Martin et al. (2014). “A parallel Jacobian-free Newton–Krylov solver for a coupled sea ice-ocean model”. en. In: *Journal of Computational Physics* 257, pages 901–911. DOI: 10.1016/j.jcp.2013.09.026 (cited on pages 16, 41, 93).
- Lund, B. et al. (2018). “Arctic Sea Ice Drift Measured by Shipboard Marine Radar”. en. In: *Journal of Geophysical Research: Oceans* 123.6, pages 4298–4321. DOI: 10.1029/2018JC013769 (cited on page 15).
- Manabe, Syukuro and Ronald J. Stouffer (1980). “Sensitivity of a global climate model to an increase of CO₂ concentration in the atmosphere”. en. In: *Journal of Geophysical Research: Oceans* 85.C10, pages 5529–5554. DOI: 10.1029/JC085iC10p05529 (cited on page 12).
- Manabe, Syukuro and Richard T. Wetherald (1967). “Thermal equilibrium of the atmosphere with a given distribution of relative humidity”. In: *Journal of the Atmospheric Sciences* 24.3, pages 241–259 (cited on page 11).
- Mancktelow, Neil S. (2006). “How ductile are ductile shear zones?” en. In: *Geology* 34.5, pages 345–348. DOI: 10.1130/G22260.1 (cited on page 96).
- Marko, John R. and Richard E. Thomson (1977). “Rectilinear leads and internal motions in the ice pack of the western Arctic Ocean”. In: *Journal of Geophys-*

- ical Research* 82.6, pages 979–987. DOI: 10.1029/JC082i006p00979 (cited on pages 16, 59, 83, 97).
- Marsan, David et al. (2012). “Sea-ice thickness measurement based on the dispersion of ice swell”. In: *The Journal of the Acoustical Society of America* 131.1, pages 80–91. DOI: 10.1121/1.3662051 (cited on page 76).
- Marshall, John et al. (1997). “A finite-volume, incompressible Navier Stokes model for studies of the ocean on parallel computers”. en. In: *Journal of Geophysical Research: Oceans* 102.C3, pages 5753–5766. DOI: 10.1029/96JC02775 (cited on pages 61, 99).
- Maykut, Gary A. (1978). “Energy exchange over young sea ice in the central Arctic”. en. In: *Journal of Geophysical Research: Oceans* 83.C7, pages 3646–3658. DOI: 10.1029/JC083iC07p03646 (cited on page 15).
- Menge, J. A. Richter and K. F. Jones (1993). “The tensile strength of first-year sea ice”. en. In: *Journal of Glaciology* 39.133, pages 609–618. DOI: 10.3189/S0022143000016506 (cited on page 50).
- Miller, Paul A., Seymour W. Laxon, and Daniel L. Feltham (2005). “Improving the spatial distribution of modeled Arctic sea ice thickness”. en. In: *Geophysical Research Letters* 32.18. DOI: 10.1029/2005GL023622 (cited on page 77).
- Mohr, O. (1882). “Ueber die Darstellung des Spannungszustandes eines Korperelements: Civilingenieure, v. 28”. In: (cited on pages 42, 43, 45).
- Mohr, Otto (1900). “Welche Umstände bedingen die Elastizitätsgrenze und den Bruch eines Materials”. In: *Zeitschrift des Vereins Deutscher Ingenieure* 46.1524-1530, pages 1572–1577 (cited on pages 43, 45, 83).
- Nguyen, An T., Ronald Kwok, and Dimitris Menemenlis (2012). “Source and Pathway of the Western Arctic Upper Halocline in a Data-Constrained Coupled Ocean and Sea Ice Model”. In: *Journal of Physical Oceanography* 42.5, pages 802–823. DOI: 10.1175/JPO-D-11-040.1 (cited on pages 13, 82).
- Nguyen, An T., Dimitris Menemenlis, and Ronald Kwok (2011). “Arctic ice-ocean simulation with optimized model parameters: Approach and assessment”. en. In: *Journal of Geophysical Research: Oceans* 116.C4, page C04025. DOI: 10.1029/2010JC006573 (cited on page 82).
- Notz, Dirk and Julienne Stroeve (2018). “The Trajectory Towards a Seasonally Ice-Free Arctic Ocean”. en. In: *Current Climate Change Reports* 4.4, pages 407–416. DOI: 10.1007/s40641-018-0113-2 (cited on page 12).
- Notz, Dirk et al. (2016). “The CMIP6 Sea-Ice Model Intercomparison Project (SIMIP): understanding sea ice through climate-model simulations”. English. In: *Geoscientific Model Development* 9.9, pages 3427–3446. DOI: <https://doi.org/10.5194/gmd-9-3427-2016> (cited on page 12).
- Oikkonen, Annu et al. (2016). “Sea ice drift and deformation in the coastal boundary zone”. en. In: *Geophysical Research Letters* 43.19, pages 10, 303–10, 310. DOI: 10.1002/2016GL069632 (cited on page 15).
- Olason, Einar Örn (2012). “Dynamical modelling of Kara Sea land-fast ice”. de. In: (cited on page 123).
- Overland, James E. et al. (1998). “Arctic sea ice as a granular plastic”. In: *Journal of geophysical research* 103.C10, pages 21845–21868 (cited on pages 13, 41, 58, 59, 82, 97).
- Petrich, Chris, Pat J. Langhorne, and Tim G. Haskell (2007). “Formation and structure of refrozen cracks in land-fast first-year sea ice”. en. In: *Journal of Geophys-*

- ical Research: Oceans* 112.C4. DOI: 10.1029/2006JC003466 (cited on pages 14, 111).
- Pithan, Felix and Thorsten Mauritsen (2014). “Arctic amplification dominated by temperature feedbacks in contemporary climate models”. en. In: *Nature Geoscience* 7.3, pages 181–184. DOI: 10.1038/ngeo2071 (cited on page 12).
- Popov, Egor P. (1976). *Mechanics of Materials*. English. 2 edition. Englewood Cliffs, N.J: Prentice Hall (cited on pages 43, 72).
- Pritchard, R. S. (1975). “An Elastic-Plastic Constitutive Law for Sea Ice”. In: *Journal of Applied Mechanics* 42.2, pages 379–384. DOI: 10.1115/1.3423585 (cited on page 59).
- Pritchard, Robert S. (1988). “Mathematical characteristics of sea ice dynamics models”. en. In: *Journal of Geophysical Research: Oceans* 93.C12, pages 15609–15618. DOI: 10.1029/JC093iC12p15609 (cited on pages 45, 49, 60, 63, 75, 77).
- Pritchard, Robert S. (2001). “Sea Ice Dynamics Models”. en. In: *IUTAM Symposium on Scaling Laws in Ice Mechanics and Ice Dynamics*. Edited by J. P. Dempsey and H. H. Shen. Solid Mechanics and Its Applications. Springer Netherlands, pages 265–288 (cited on page 39).
- Rampal, P. et al. (2016). “neXtSIM: a new Lagrangian sea ice model”. In: *The Cryosphere* 10.3, pages 1055–1073. DOI: 10.5194/tc-10-1055-2016 (cited on pages 58, 59, 82).
- Ringeisen, Damien, L. Bruno Tremblay, and Martin Losch (2020). “Non-normal flow rules affect fracture angles in sea ice viscous-plastic rheologies”. English. In: *The Cryosphere Discussions*, pages 1–24. DOI: <https://doi.org/10.5194/tc-2020-153> (cited on page 81).
- Ringeisen, Damien et al. (2019). “Simulating intersection angles between conjugate faults in sea ice with different viscous–plastic rheologies”. English. In: *The Cryosphere* 13.4, pages 1167–1186. DOI: <https://doi.org/10.5194/tc-13-1167-2019> (cited on pages 18, 30, 41, 57, 83, 87, 88, 90, 91, 95–98).
- Roach, Lettie A. et al. (2018). “An Emergent Sea Ice Floe Size Distribution in a Global Coupled Ocean-Sea Ice Model”. en. In: *Journal of Geophysical Research: Oceans* 123.6, pages 4322–4337. DOI: 10.1029/2017JC013692 (cited on pages 97, 123).
- Roscoe, K. H. (1970). “The Influence of Strains in Soil Mechanics”. In: *Géotechnique* 20.2, pages 129–170. DOI: 10.1680/geot.1970.20.2.129 (cited on pages 42, 43, 46, 50, 56, 83, 87, 88, 95, 98, 108).
- Roscoe, K. H., A. N. Schofield, and C. P. Wroth (1958). “On The Yielding of Soils”. In: *Géotechnique* 8.1, pages 22–53. DOI: 10.1680/geot.1958.8.1.22 (cited on page 15).
- Rothrock, D. A. (1975a). “The energetics of the plastic deformation of pack ice by ridging”. en. In: *Journal of Geophysical Research* 80.33, pages 4514–4519. DOI: 10.1029/JC080i033p04514 (cited on page 97).
- Rothrock, D. A. (1975b). “The Mechanical Behavior of Pack ICE”. In: *Annual Review of Earth and Planetary Sciences* 3.1, pages 317–342. DOI: 10.1146/annurev.earth.03.050175.001533 (cited on page 24).
- Rothrock, D. A. (1975c). “The steady drift of an incompressible Arctic ice cover”. en. In: *Journal of Geophysical Research* 80.3, pages 387–397. DOI: 10.1029/JC080i003p00387 (cited on pages 16, 58).

- Rothrock, D. A. and A. S. Thorndike (1984). “Measuring the sea ice floe size distribution”. en. In: *Journal of Geophysical Research: Oceans* 89.C4, pages 6477–6486. DOI: 10.1029/JC089iC04p06477 (cited on pages 13, 58, 98).
- Schmidt, Gavin A. et al. (2014). “Configuration and assessment of the GISS ModelE2 contributions to the CMIP5 archive”. en. In: *Journal of Advances in Modeling Earth Systems* 6.1, pages 141–184. DOI: 10.1002/2013MS000265 (cited on page 77).
- Schreyer, H. L. et al. (2006). “Elastic-decohesive constitutive model for sea ice”. en. In: *Journal of Geophysical Research: Oceans* 111.C11, C11S26. DOI: 10.1029/2005JC003334 (cited on pages 17, 58).
- Schulson, E. M. et al. (2006). “On the role of frictional sliding in the compressive fracture of ice and granite: Terminal vs. post-terminal failure”. en. In: *Acta Materialia* 54.15, pages 3923–3932. DOI: 10.1016/j.actamat.2006.04.024 (cited on page 98).
- Schulson, Erland M. (2004). “Compressive shear faults within arctic sea ice: Fracture on scales large and small”. en. In: *Journal of Geophysical Research: Oceans* 109.C7, page C07016. DOI: 10.1029/2003JC002108 (cited on pages 52, 59, 64, 68, 75, 108).
- Schulson, Erland M. and William D. Hibler (2004). “Fracture of the winter sea ice cover on the Arctic ocean”. en. In: *Comptes Rendus Physique. Ice: from dislocations to icy satellites* 5.7, pages 753–767. DOI: 10.1016/j.crhy.2004.06.001 (cited on page 82).
- Schweiger, Axel et al. (2011). “Uncertainty in modeled Arctic sea ice volume”. en. In: *Journal of Geophysical Research: Oceans* 116.C8. DOI: 10.1029/2011JC007084 (cited on page 14).
- Screen, James A. and Ian Simmonds (2010). “The central role of diminishing sea ice in recent Arctic temperature amplification”. en. In: *Nature* 464.7293, pages 1334–1337. DOI: 10.1038/nature09051 (cited on page 12).
- Serreze, M. C. et al. (2009). “The emergence of surface-based Arctic amplification”. English. In: *The Cryosphere* 3.1, pages 11–19. DOI: <https://doi.org/10.5194/tc-3-11-2009> (cited on page 12).
- Shukla, J., C. Nobre, and P. Sellers (1990). “Amazon Deforestation and Climate Change”. en. In: *Science* 247.4948, pages 1322–1325. DOI: 10.1126/science.247.4948.1322 (cited on page 12).
- SIMIP Community (2020). “Arctic Sea Ice in CMIP6”. en. In: *Geophysical Research Letters* 47.10, e2019GL086749. DOI: 10.1029/2019GL086749 (cited on pages 12, 15).
- Sirven, Jérôme and Bruno Tremblay (2014). “Analytical Study of an Isotropic Viscoplastic Sea Ice Model in Idealized Configurations”. In: *Journal of Physical Oceanography* 45.2, pages 331–354. DOI: 10.1175/JPO-D-13-0109.1 (cited on page 76).
- Spren, G. et al. (2017). “Sea-ice deformation in a coupled ocean–sea-ice model and in satellite remote sensing data”. In: *The Cryosphere* 11.4, pages 1553–1573. DOI: 10.5194/tc-11-1553-2017 (cited on pages 59, 82).
- Stern, H. L., D. A. Rothrock, and R. Kwok (1995). “Open water production in Arctic sea ice: Satellite measurements and model parameterizations”. In: *Journal of Geophysical Research: Oceans* 100.C10, pages 20601–20612. DOI: 10.1029/95JC02306 (cited on pages 29, 77, 82, 84, 97, 108, 123).

- Stroeve, J. et al. (2014). “Using records from submarine, aircraft and satellites to evaluate climate model simulations of Arctic sea ice thickness”. In: *The Cryosphere* 8.5, pages 1839–1854. DOI: 10.5194/tc-8-1839-2014 (cited on pages 16, 58, 78, 82).
- Sulsky, Deborah et al. (2007). “Using the material-point method to model sea ice dynamics”. en. In: *Journal of Geophysical Research: Oceans* 112.C2, C02S90. DOI: 10.1029/2005JC003329 (cited on pages 17, 60).
- Thorndike, A. S. et al. (1975). “The thickness distribution of sea ice”. en. In: *Journal of Geophysical Research* 80.33, pages 4501–4513. DOI: 10.1029/JC080i033p04501 (cited on pages 16, 118).
- Tremblay, L-B. and L. A. Mysak (1997). “Modeling Sea Ice as a Granular Material, Including the Dilatancy Effect”. In: *Journal of Physical Oceanography* 27.11, pages 2342–2360. DOI: 10.1175/1520-0485(1997)027<2342:MSIAAG>2.0.CO;2 (cited on pages 17, 20, 22, 24, 39, 42, 58, 59, 62, 77, 83, 84, 96, 98, 108, 123).
- Trisos, Christopher H., Cory Merow, and Alex L. Pigot (2020). “The projected timing of abrupt ecological disruption from climate change”. en. In: *Nature* 580.7804, pages 496–501. DOI: 10.1038/s41586-020-2189-9 (cited on page 12).
- Tsamados, M., D. L. Feltham, and A. V. Wilchinsky (2013). “Impact of a new anisotropic rheology on simulations of Arctic sea ice”. en. In: *Journal of Geophysical Research: Oceans* 118.1, pages 91–107. DOI: 10.1029/2012JC007990 (cited on page 59).
- Ukita, Jinro and Richard E. Moritz (1995). “Yield curves and flow rules of pack ice”. en. In: *Journal of Geophysical Research: Oceans* 100.C3, pages 4545–4557. DOI: 10.1029/94JC02202 (cited on page 25).
- Ungermann, Mischa et al. (2017). “Impact of the Ice Strength Formulation on the Performance of a Sea Ice Thickness Distribution Model in the Arctic”. en. In: *Journal of Geophysical Research: Oceans*, n/a–n/a. DOI: 10.1002/2016JC012128 (cited on pages 16, 24, 77).
- Untersteiner, N. (1961). “On the mass and heat budget of arctic sea ice”. en. In: *Archiv für Meteorologie, Geophysik und Bioklimatologie, Serie A* 12.2, pages 151–182. DOI: 10.1007/BF02247491 (cited on page 15).
- Urban, Mark C. (2015). “Accelerating extinction risk from climate change”. en. In: *Science* 348.6234, pages 571–573. DOI: 10.1126/science.aaa4984 (cited on page 12).
- Vardoulakis, I. (1980). “Shear band inclination and shear modulus of sand in biaxial tests”. en. In: *International Journal for Numerical and Analytical Methods in Geomechanics* 4.2, pages 103–119. DOI: 10.1002/nag.1610040202 (cited on pages 42, 83).
- Vardoulakis, I. and B. Graf (1985). “Calibration of constitutive models for granular materials using data from biaxial experiments”. In: *Géotechnique* 35.3, pages 299–317. DOI: 10.1680/geot.1985.35.3.299 (cited on pages 83, 107).
- Vermeer, P. A. (1990). “The orientation of shear bands in biaxial tests”. en. In: *Géotechnique*. DOI: 10.1680/geot.1990.40.2.223 (cited on pages 42, 83, 108).
- Vermeer, Pieter A. and R. De Borst (1984). “Non-associated plasticity for soils, concrete and rock”. In: *HERON*, 29 (3), 1984 (cited on page 91).
- Verruijt, Arnold (2018). *An Introduction to Soil Mechanics*. en. Theory and Applications of Transport in Porous Media. Springer International Publishing (cited on pages 31, 44).

- Vihma, Timo (2014). “Effects of Arctic Sea Ice Decline on Weather and Climate: A Review”. en. In: *Surveys in Geophysics* 35.5, pages 1175–1214. DOI: 10.1007/s10712-014-9284-0 (cited on page 13).
- Walter, Bernard A. and James E. Overland (1993). “The response of lead patterns in the Beaufort Sea to storm-scale wind forcing”. en. In: *Annals of Glaciology* 17, pages 219–226. DOI: 10.3189/S0260305500012878 (cited on pages 60, 75).
- Wang, Keguang (2007). “Observing the yield curve of compacted pack ice”. en. In: *Journal of Geophysical Research: Oceans* 112.C5, page C05015. DOI: 10.1029/2006JC003610 (cited on pages 39, 59, 60, 77, 84).
- Wang, Keguang, Matti Leppäranta, and Tarmo Kõuts (2006). “A study of sea ice dynamic events in a small bay”. In: *Cold Regions Science and Technology* 45.2, pages 83–94. DOI: 10.1016/j.coldregions.2006.02.002 (cited on pages 45, 59).
- Wang, Keguang and Caixin Wang (2009). “Modeling linear kinematic features in pack ice”. en. In: *Journal of Geophysical Research: Oceans* 114.C12. DOI: 10.1029/2008JC005217 (cited on page 39).
- Wang, Q. et al. (2016). “Sea ice leads in the Arctic Ocean: Model assessment, interannual variability and trends”. en. In: *Geophysical Research Letters* 43.13, pages 7019–7027. DOI: 10.1002/2016GL068696 (cited on page 60).
- Weiss, Jérôme and Véronique Dansereau (2017). “Linking scales in sea ice mechanics”. en. In: *Phil. Trans. R. Soc. A* 375.2086, page 20150352. DOI: 10.1098/rsta.2015.0352 (cited on page 13).
- Weiss, Jérôme and Erland M. Schulson (2009). “Coulombic faulting from the grain scale to the geophysical scale: lessons from ice”. en. In: *Journal of Physics D: Applied Physics* 42.21, page 214017. DOI: 10.1088/0022-3727/42/21/214017 (cited on pages 16, 48, 83, 97, 98, 108, 122).
- Weiss, Jérôme, Erland M. Schulson, and Harry L. Stern (2007). “Sea ice rheology from in-situ, satellite and laboratory observations: Fracture and friction”. In: *Earth and Planetary Science Letters* 255.1–2, pages 1–8. DOI: 10.1016/j.epsl.2006.11.033 (cited on pages 52, 59, 64, 77, 82, 84, 98).
- Wilchinsky, Alexander V. and Daniel L. Feltham (2006a). “Anisotropic model for granulated sea ice dynamics”. In: *Journal of the Mechanics and Physics of Solids* 54.6, pages 1147–1185. DOI: 10.1016/j.jmps.2005.12.006 (cited on pages 17, 58, 75).
- Wilchinsky, Alexander V. and Daniel L. Feltham (2006b). “Modelling the rheology of sea ice as a collection of diamond-shaped floes”. In: *Journal of Non-Newtonian Fluid Mechanics* 138.1, pages 22–32. DOI: 10.1016/j.jnnfm.2006.05.001 (cited on page 82).
- Wilchinsky, Alexander V. and Daniel L. Feltham (2011). “Modeling Coulombic failure of sea ice with leads”. In: *Journal of Geophysical Research: Oceans* 116.C8. DOI: 10.1029/2011JC007071 (cited on page 70).
- Wilchinsky, Alexander V. and Daniel L. Feltham (2012). “Rheology of Discrete Failure Regimes of Anisotropic Sea Ice”. In: *Journal of Physical Oceanography* 42.7, pages 1065–1082. DOI: 10.1175/JP0-D-11-0178.1 (cited on page 70).
- Wilchinsky, Alexander V., Daniel L. Feltham, and Mark A. Hopkins (2010). “Effect of shear rupture on aggregate scale formation in sea ice”. en. In: *Journal of Geophysical Research: Oceans* 115.C10, page C10002. DOI: 10.1029/2009JC006043 (cited on pages 17, 60, 75, 92).

- Wilchinsky, Alexander V., Daniel L. Feltham, and Mark A. Hopkins (2011). “Modelling the reorientation of sea-ice faults as the wind changes direction”. en. In: *Annals of Glaciology* 52.57, pages 83–90. DOI: 10.3189/172756411795931831 (cited on page 70).
- Williams, James, L. Bruno Tremblay, and Jean-François Lemieux (2017). “The effects of plastic waves on the numerical convergence of the viscous–plastic and elastic–viscous–plastic sea-ice models”. In: *Journal of Computational Physics* 340, pages 519–533. DOI: 10.1016/j.jcp.2017.03.048 (cited on page 93).
- Zhang, Jinlun and W. D. Hibler (1997). “On an efficient numerical method for modeling sea ice dynamics”. en. In: *Journal of Geophysical Research: Oceans* 102.C4, pages 8691–8702. DOI: 10.1029/96JC03744 (cited on pages 58, 65, 91).
- Zhang, Jinlun and D. A. Rothrock (2003). “Modeling Global Sea Ice with a Thickness and Enthalpy Distribution Model in Generalized Curvilinear Coordinates”. In: *Monthly Weather Review* 131.5, pages 845–861. DOI: 10.1175/1520-0493(2003)131<0845:MGSIWA>2.0.CO;2 (cited on page 14).
- Zhang, Jinlun and D. A. Rothrock (2005). “Effect of sea ice rheology in numerical investigations of climate”. en. In: *Journal of Geophysical Research: Oceans* 110.C8, page C08014. DOI: 10.1029/2004JC002599 (cited on pages 20, 35, 36, 38, 54, 59, 84, 97, 105, 109).